ON THE DYNAMICS OF THE FORMATION OF MULTIPLE TROPICAL DISTURBANCES

by

Rosana Nieto Ferreira

Colorado State University

DEPARTMENT OF ATMOSPHERIC SCIENCE

PAPER NO. 559

ON THE DYNAMICS OF THE FORMATION OF MULTIPLE TROPICAL DISTURBANCES

by

Rosana Nieto Ferreira

Department of Atmospheric Science
Colorado State University
Fort Collins, CO 80523

Summer 1994

Atmospheric Science Paper No. 559

ABSTRACT

ON THE DYNAMICS OF THE FORMATION OF MULTIPLE TROPICAL DISTURBANCES

A nonlinear shallow water model on the sphere is used to study the early stages of tropical cyclone genesis, namely, the formation of tropical disturbances. Two particular cases in which one or more tropical disturbances are produced are studied: the ITCZ breakdown and the formation of disturbances that lead to twin tropical cyclones.

The ITCZ breakdown is seen to be a plausible mechanism for the formation of tropical disturbances. This mechanism also offers an explanation for the observations of easterly waves outside the Atlantic basin. In the Eastern Pacific, in particular, the time and space clustering of tropical cyclone genesis lend support to the hypothesis that the ITCZ breakdown plays a role in their formation.

Tropical cyclone twins are observed exclusively in the Indian Ocean and in the West Pacific near the dateline. They are believed to form in association with super cloud clusters that straddle the equator in those regions. Shallow water model results presented herein corroborate this hypothesis. The existence of preferred regions for their formation is proposed to be associated with the life cycle and movement of their parent super cloud clusters.

The shallow water model proved to be a useful simple tool for investigating barotropic dynamical aspects of the formation of tropical cyclone disturbances.

ACKNOWLEDGEMENTS

I wish to thank my advisor, Dr. Wayne H. Schubert, for his dedicated guidance, encouragement and teachings throughout the completion of this degree. I am also grateful to Drs. Richard H. Johnson, David A. Randall and Gerald D. Taylor for serving in my committee. I also thank Dr. Michael T. Montgomery for his review of this work and for participating in my committee.

Thanks also go to Paul Ciesielski and Rick Taft for their patience and willingness in guiding me through the mysterious world of computers. I am grateful to Tom Rickenbach for his support throughout this work and his reading and commenting on the initial manuscript. I am grateful to Dr. Raymond Zehr who contributed to this work with numerous discussions about tropical cyclones and also for reviewing the initial manuscript. I have also benefited from discussions with my colleagues, members of the research groups of Drs. Wayne Schubert and William Gray. I also thank Lígia R. Bernardet and James Edwards for their review of the manuscript. Many other friends and colleagues contributed to this work in different ways.

I express here my gratitude to my parents and brother whose encouragement has always been essential to my work. (*Agradeço aos meus pais e irmão, cujo estímulo sempre foi essencial para o meu trabalho*).

This work was supported by *CNPq*, the Brazilian Council for the Development of Science and Technology and by the National Science Foundation, under grant ATM-9115485. Additional computing support was provided by NCAR (National Center for Atmospheric Research).

CONTENTS

1 Introduction **1**
1.1 Tropical Cyclogenesis 1
1.1.1 Internal Mechanisms 3
1.1.2 External Mechanisms 4
1.1.3 A Conceptual Model for Tropical Cyclogenesis 8
1.2 The Intertropical Convergence Zone 12
1.2.1 A Climatology of the ITCZ 12
1.2.2 Transience and Cyclogenesis within the ITCZ 14

2 The Shallow Water Model **19**
2.1 The Governing Equations 19
2.2 Conservation Principles 21
2.3 Use of Shallow Water Models in Tropical Dynamics 23
2.4 Model Initialization 24

3 Stability Studies **27**
3.1 Stability Theory 28
3.1.1 Linear Barotropic Nondivergent Stability Theorem 29
3.1.2 Linear Barotropic Divergent Stability Theorem 30
3.1.3 The Nature of Barotropic Instability 33
3.2 Linear Normal Mode Stability Analysis of Vorticity Strips 35
3.2.1 Stability Results 36
3.3 Wave-activity Diagnostics 38
3.3.1 Disturbance Pseudo-Momemtum 41

4 ITCZ Breakdown **45**
4.1 Zonally Symmetric Vorticity Strips 46
4.2 Interaction Between a Vortex and a Zonally Symmetric PV Strip 50
4.3 Elliptical Mass Sink 58
4.4 Distorted Ellipsoidal Mass Sink 64
4.5 Frequency of Tropical Cyclone Genesis in the Eastern Pacific 68

5 Twin Tropical Cyclones **74**
5.1 Observations 74
5.1.1 A 'Canonical' Tropical Cyclone Pair 76
5.1.2 A Short Climatology of Tropical Cyclone Twins 83
5.2 Twin Tropical Cyclone Formation 85
5.3 Preferred Regions for Twin Tropical Cyclone Formation 94
5.4 Movement of Twin Tropical Cyclones 103

6 Summary and Conclusions **105**

REFERENCES **112**

A Numerical Aspects of the Global Shallow Water Model **124**
A.1 The spectral transform method 124
A.2 The semi-implicit time differencing scheme 127

B Linear stability analysis **129**

LIST OF FIGURES

1.1 Schematic diagram of a conceptual model of tropical cyclone genesis proposed by Zehr (1992) 11
1.2 Mean monthly 'ITCZ' structure for *a)* January, *b)* April, *c)* July and *d)* October. 13
1.3 ITCZ breakdown in the Eastern Pacific 16

2.1 Rate of dissipation as a function of wavenumber, n. 25

3.1 Interpretation of the physical mechanism for barotropic instability through the interactions between two counter propagating Rossby waves. 34
3.2 Characteristics of the most unstable modes obtained in the linear normal mode stability calculations 37
3.3 E-folding time and wavenumber of the most unstable mode as a function of the intensity of the vorticity strip. 38
3.4 Growth rate spectra for vorticity strips of different widths centered at $10°N$ with $\zeta_s = 3.0 \times 10^{-5} s^{-1}$. Strip widths are 5, 7, 9 and 11°. 39
3.5 Streamfunctions showing the time evolution of the most unstable mode for $\phi_c = 10°$ and $\alpha = 7°$. Fields are at 0, 8 and 16 e-folding times. 40
3.6 Meridional profiles of zonal wind and absolute vorticity for a vorticity strip centered at $\phi_c = 10°$ and with width $\alpha = 7°$ 41

4.1 Meridional profiles of the initial zonal wind and absolute vorticity across a 7° wide zonally symmetric vorticity strip centered at $15°N$ with maximum intensity $\zeta_s = 3.0 \times 10^{-5}\, s^{-1}$. 47
4.2 Breakdown of a 7° wide zonally symmetric vorticity strip centered at $15°N$ with maximum intensity $\zeta_s = 3.0 \times 10^{-5}\, s^{-1}$; *a)* initial height (in m), PV (in $s\,m^{-2}$, with contours from 0. to 1.6×10^{-8} by 0.2×10^{-8}) and wind fields (in m/s), b) same fields at 5 days, c) idem at 11 days. In the PV plot, values greater than $1.4 \times 10^{-8} s\,m^{-2}$ are dotted. Maximum wind vectors are $20 m/s$ and span the distance between two plotted grid points. 48
4.3 GOES infrared satellite images for the E. Pacific during the period between 13 and 21 July 1978 (time is UTC). The sequence illustrates the interaction of Hurricane Fico with the ITCZ. 51
4.4 Radial relative vorticity and wind distributions of the vortex used in the simulation of the interactions between a zonally symmetric PV strip and a nearby vortex. 53

4.5 Interaction of a vortex centered at $15°N$ with $\zeta_v = 2 \times 10^{-4}\, s^{-1}$ and 2° in radius with a 7° wide zonally symmetric PV strip centered at $10°N$ with $\zeta_s = 3 \times 10^{-5}\, s^{-1}$. Height (m), wind (m/s) and PV ($s\,m^{-2}$) fields at *a)* initial fields, *b)* 2 days, *c)* 6 days and *d)* 9 days. PV contours are from 0. to 5.6×10^{-9} by 0.2×10^{-9} and maximum wind vector is $20\,m/s$ in modulus and spans the distance between two plotted grid points. 54
4.6 Trajectories followed by vortices initially centered at 15° (NPV), 10° (CPV) and 5° (SPV), under the influence of a zonally symmetric PV strip centered at 10°. The trajectory of a vortex centered at 10° in a quiescent environment (VOR) is included for comparison. Symbols denote vortex positions at 24h intervals. 56
4.7 Height (m) and PV ($s\,m^{-2}$) fields for a 2° radius vortex with $\zeta_v = 2 \times 10^{-4}\, s^{-1}$ and $\phi_c = 15°N$ in a quiescent environment. *a)* at 9 days; *b)* at 15 days. . . 57
4.8 Radial and temporal variations of the mass sink. 59
4.9 Evolution of height (m), PV ($s\,m^{-2}$) and wind (m/s) fields for the case in which a zonally oriented elliptical mass sink centered at $\phi_c = 10°N$, with $c = 60$, $d = 4$ and $\tau = 4$ is imposed. 61
4.10 Meridional profiles of zonal winds across the center of the PV strip after 1, 5 and 15 days. 63
4.11 GOES IR satellite images for 28, 29 and 31 of May, 1978, showing the formation of Hurricane Aletta (time is UTC). 66
4.12 Evolution of a zonally oriented distorted ellipsoidal mass sink centered at $\phi_c = 10°N$,, with $c = 40$, $d = 4$, $\tau = 4$, $\alpha_i = 3$ and $\alpha_r = 3$. 67
4.13 Evolution of a zonally oriented elliptical mass sink centered at $\phi_c = 10°N$, with $c = 40°$, $d = 4°$ and $\tau = 4$. 69
4.14 Tropical storms in the E. Pacific between 1980 and 1993. 70
4.15 Frequencies of occurrence of intergenesis intervals (in days) between all storms during 1980 through 1993. 71
4.16 Longitudes and dates of formation of storms found in time clusters from 1980 to 1993. Dates on the right column indicate date of formation of storm '0'. Storm '1' formed a day later, and so forth. The '*' indicate time clusters in which the storms formed successively from west to east. 72
4.17 Frequencies of occurrence of longitudinal distances between storms that formed within the same time cluster. 73

5.1 GMS IR satellite images showing the life cycles of twin tropical cyclones in the W. Pacific. 77
5.2 ECMWF 850 mb wind analyses for the Western Pacific during a tropical cyclone twins event. 80
5.3 Radial and temporal variations of the mass sink. 86
5.4 Evolution produced by a mass sink centered at the equator with $c = 10°$, $d = 15°$, $\tau = 5$, $\overline{\Phi} = 2177.15$ and $\mid \partial\Phi/\partial t \mid = 864\ m^2 s^{-2} day^{-1}$. 87
5.5 Evolution produced by a mass sink centered at $2.5°N$ with $c = 10°$, $d = 15°$, $\tau = 5$, $\overline{\Phi} = 2177.15\ m^2 s^{-2} day^{-1}$ and $\mid \partial\Phi/\partial t \mid = 864\ m^2 s^{-2} day^{-1}$. 92
5.6 Height (m), wind (m/s) and PV($s\,m^{-2}$) fields for a meridionally elongated mass sink centered at the equator and moving due east at 5 m/s. 96
5.7 Height (m), wind (m/s) and PV ($s\,m^{-2}$) fields for a meridionally elongated mass sink centered at the equator and moving due east at 10 m/s. 97

5.8 Height, wind and PV fields for a meridionally elongated mass sink centered at the equator and moving due east at variable speed. 98
5.9 Time variation of the speed of the mass sink. 102
5.10 Trajectories followed by twin vortices. 104

B.1 Stairstep distribution of vorticity. 130

LIST OF TABLES

2.1 Time steps and K_4 used with $T126$ and $T213$ spectral truncations. 25

5.1 Dates and approximate longitudes of formation of twin tropical cyclones from January 1983 through December 1993, in the tropical belt between $70°E$ and $150°W$. 84

Chapter 1

INTRODUCTION

Tropical cyclones are intense cyclonic storms that form over the warmest waters of the tropical oceans. Along with earthquakes, intense tropical cyclones are the most destructive natural phenomena on Earth, claiming many lives and high costs in property damage every year. Although addressed in numerous studies, tropical cyclogenesis still awaits a widely accepted elucidation. This is in part due to the historical scarcity of observations over the oceanic regions where tropical cyclogenesis takes place.

1.1 Tropical Cyclogenesis

Before addressing the topic of tropical cyclogenesis, it is useful to review some relevant definitions. Tropical cyclones are classified in three different categories according to their intensity. At the bottom of the tropical cyclone hierarchy are *tropical depressions* which have a well defined low level cyclonic circulation with maximum rotating winds of less than 17 m/s; next come *tropical storms* with maximum winds between 17 and 33 m/s; and finally, *hurricanes* (or *typhoons*, as they are called in the West Pacific) are strong storms with sustained maximum winds that exceed 33 m/s. *Tropical disturbances* such as easterly waves or cloud clusters precede tropical cyclones in the aforementioned hierarchy and are characterized by broad regions ($\sim 200 - 600$ km in diameter) of organized convection that do not contain a persistent and well defined mesoscale cyclonic circulation (Frank, 1987). Tropical disturbances are composed of a number of mesoscale convective systems.

In the literature, some confusion often occurs when different definitions are given to the term tropical cyclogenesis. Throughout this work, *tropical cyclogenesis* (or *formation*) will be understood to begin with the formation of a tropical disturbance and end when the tropical storm stage is reached, including the formation of the mesoscale cyclonic vortex.

The development of the storm beyond the tropical storm stage is called *intensification* (Frank, 1987; Zehr, 1992).

Approximately 80 tropical storms form each year in the tropics and about 60% of these become hurricanes. Climatologically, tropical cyclogenesis is favored in regions where certain empirical thermodynamic and dynamic parameters are propitious (Gray, 1975). The thermodynamic parameter is composed of three factors, namely, *1)* a conditionally unstable atmosphere below 500 mb, *2)* a warm and deep oceanic mixed layer, and *3)* above average middle level moisture. The dynamic parameter combines a *1)* significant value of planetary vorticity (typically farther than 5° away from the equator), *2)* weak vertical wind shear of the horizontal wind and *3)* high low level relative vorticity. Gray (1975) combines the thermodynamic and dynamic parameters into a seasonal genesis parameter that successfully diagnoses the observed geographical distribution of tropical cyclone genesis. The thermodynamic and Coriolis parameters, however, are favorable over large portions of the tropical oceans during much of the year while tropical cyclones are relatively rare events compared to the large number of tropical disturbances that are potential candidates to undergo genesis. Gray and collaborators suggested that the low level vorticity and the vertical wind shear are the critical parameters to distinguish between developing and non-developing disturbances, given that the other conditions are favorable. These dynamic variables were combined to calculate a genesis parameter that may be used to differentiate individual developing from non-developing disturbances (McBride and Zehr, 1981; Zehr, 1992).

Large scale processes such as the El Niño-Southern Oscillation (Gray, 1989; Lander, 1994; ENSO), Quasi-Biennial Oscillation (Gray, 1989; QBO) and the Madden Julian Oscillation (Liebmann *et al.*, 1993; MJO; see Madden and Julian, 1994, for an overview of observational work on the MJO) have been shown to influence tropical cyclogenesis through the changes they provoke in the environmental parameters discussed above.

Over the past few decades, several theories for tropical cyclogenesis have been put forth. While all propose pieces of the tropical cyclogenesis puzzle, a complete understanding of the role of environmental and internal processes in the genesis problem still awaits

elucidation. In this work, the initial stages of tropical cyclone genesis, namely, the formation of tropical disturbances, is studied. Before presenting the approach taken in this study, a review of relevant work is given below. Some of these theories concentrate on processes internal to the storm, others evoke external processes.

1.1.1 Internal Mechanisms

In the early years, studies of tropical cyclone genesis concentrated on searching for linear instabilities of the mean tropical atmosphere that would amplify resulting in a tropical cyclone. The main theory that emerged during this quest was that of Conditional Instability of the Second Kind (CISK), proposed by Charney and Eliassen (1964) and Ooyama (1964).

In CISK, the intensification of a tropical depression occurs through a cooperative feedback between its embedded cumulus convection and mesoscale circulations, the former supplying the energy (in the form of latent heating) to intensify the vortex and the latter providing the boundary layer convergence that is vital for maintaining deep convection. An important effect ignored in linear CISK theory is the role of time varying inertial stability on the intensification of the storm. As the storm intensifies, its inertial stability increases gradually improving the efficiency of latent heating in further strengthening the storm (Schubert and Hack, 1982). CISK, however, was intended as a theory for tropical cyclone intensification rather than genesis (Ooyama, 1982).

In CISK, the energy for the growth of the disturbance is supplied by CAPE (Convective Available Potential Energy) stored in the atmosphere. Emanuel (1986) and Rotunno and Emanuel (1987) argue that there is little CAPE in the tropical atmosphere and the source of energy for storm intensification is provided by sensible and latent heat fluxes from the ocean. A finite amplitude instability is then proposed, the so called Wind Induced Surface Heat Exchange (WISHE), which arises through a positive feedback between latent and sensible heat fluxes from the ocean and the surface tangential wind in an environment with no initial CAPE.

In both of the theories above, intensification is conditioned on the existence of a finite amplitude initial vortex.

1.1.2 External Mechanisms

Several different types of external forcing of tropical cyclone genesis have been proposed, among these are the theories of upper level forcing, low level forcing and topography influences which are reviewed below.

Riehl (1945) was among the first to recognize the existence of westward moving waves (the so called easterly waves) in the lower levels of the tropical atmosphere, and their importance in tropical cyclone genesis. Riehl observed that tropical easterly waves formed somewhere in Africa (with a frequency of about one every 2-4 days) and propagated westward (at 5-7 m/s), losing some intensity as they crossed the stable air over the Eastern Atlantic, but strengthening over the Western Atlantic and, in some cases, crossing Central America moving into the Eastern Pacific Ocean.

Easterly waves have been observed in the eastern Atlantic and West Africa (Carlson, 1969; Burpee, 1972, 1975; Reed *et al.*,1977; Chen and Ogura, 1982), Western and Central Pacific (Reed and Recker, 1971; Yanai, 1961), South China Sea and India (Saha *et al.*, 1981) and Eastern Pacific Ocean (Chang, 1970; Tai and Ogura, 1987). Among these, the most extensively documented and studied are the Atlantic and West African easterly waves.

In the Atlantic basin, it is well established that approximately half of the tropical cyclones originate from African easterly waves (Frank, 1987). About 60 of these waves form every year in eastern central Africa between May and November (Carlson, 1969a; Avila and Clark, 1989). They propagate westward into the Atlantic ocean (Carlson, 1969b) often being tracked as far west as the Caribbean and Eastern Pacific (Riehl, 1945; Simpson *et al.*, 1969; Frank, 1969a; Frank, 1976; Frank,1987; Avila and Clark, 1989; and many others). Once over the ocean, some of these easterly waves participate in tropical cyclogenesis. Consistent with the early observations of Riehl (1945), the average wavelength of these easterly waves is observed to be approximately 2500 km with westward propagation speed of about 8 m/s and maximum disturbance amplitude near the 700 mb level (Reed *et al.*, 1977; Burpee, 1972).

Through both observational (Burpee, 1972; Norquist *et al.*, 1977) and numerical (Rennick, 1976; Simmons, 1977; Mass, 1979; Kuo, 1978, Kwon, 1989) studies, a consensus seems to have been achieved that African easterly waves result from combined barotropic and baroclinic instability of the African easterly jet. The relative importance of these two instability mechanisms has not yet been satisfactorily established. Although the tropical easterly jet is present over the southern part of the African bulge all year round, it is a well organized feature of the circulation only from April to November. This jet has a maximum of about 13 m/s at around 650 mb and 16°N (Norquist *et al.*, 1977) and its existence is usually explained in the literature through thermal wind balance over the southern part of the African bulge. In that region, a strong meridional temperature gradient between the warm Saharan air and the colder air over the Guinea Gulf, requires the existence of the easterly jet. Since this mechanism depends on surface boundary conditions that are particular to the African region, it does not appear to explain the aforementioned observations of easterly waves in the other oceanic basins, unless they can be shown to have originated in Africa.

In the Eastern Pacific, for example, there is some controversy regarding the frequency with which African easterly waves cross Central America and trigger tropical cyclones (Simpson *et al.*, 1969; Frank, 1969a; Frank, 1976; Frank, 1987; Avila and Clark, 1989; and many others). An observational study by Tai and Ogura (1987) suggests that easterly waves in the Pacific Ocean are not typically related to African Waves but rather have a local origin. They also show that easterly wave activity is a maximum in July and August in the Pacific basin. Easterly wave activity is stronger in the Western Pacific, followed by the Eastern Pacific and finally the Central Pacific. No attempt has been made to connect African waves to disturbances in the Central or Western Pacific. Nitta and Yanai (1969), show that the mean zonal flow in the Western Pacific is barotropically unstable during some of the summer months. Given the lack of strong underlying meridional temperature gradients in the Pacific Ocean, a different mechanism for producing the unstable mean flow must be present. This will be further discussed in section 1.2.2.

Based on observations in the West Atlantic, Riehl (1948) was among the first to suggest that tropical cyclone genesis is favored in regions where there occurs superposition

of a westerly moving upper-level trough and an easterly moving tropical disturbance (such as the previously mentioned easterly waves).

Further observational evidence attesting for the importance of upper tropospheric disturbances in tropical cyclone genesis and intensification is presented by Sadler (1976, 1978). He observes that in the Western Pacific tropical cyclone genesis often occurs in the monsoon trough in association with a tropical upper tropospheric trough (TUTT). Sadler argues that the presence of a TUTT to the N-NW of a tropical disturbance provides a westerly outlfow channel aloft that acts to efficiently remove both mass and heat from the tropical disturbance, favoring its development into a tropical storm.

Modeling studies of the role of upper level disturbances in the formation of Atlantic hurricanes were performed by Challa and Pfeffer (1990, and references therein). Using initial conditions from developing and non-developing cloud cluster composites calculated by McBride (1981 a and b) and McBride and Zehr (1981), Challa and Pfeffer conclude that upper tropospheric eddy flux convergence of angular momentum associated with wavelike disturbances in the upper troposphere may act as a trigger for tropical cyclone genesis and intensification in the developing cases.

Montgomery and Farrel (1993) also pursued the hypothesis of cyclogenesis induced by upper tropospheric forcing, but used a potential vorticity (PV) dynamics approach in an attempt to unify the theories of tropical and extratropical cyclogenesis. They proposed a model of tropical cyclone genesis initiated by translating upper level PV anomalies in areas of deep moist neutrality which is similar, in concept, to models of extratropical cyclogenesis. They used both two-dimensional and three-dimensional Boussinesq semi-geostrophic balanced models that incorporated moist processes to simulate tropical cyclone genesis in near moist-neutral environments. The three-dimensional dynamics was illustrated for model parameters that simulated the formation of Hurricane Diana. This hurricane formed off the Florida coast (near $30°N$) in September of 1984 associated with a westerly moving upper tropospheric positive PV anomaly upwind of a surface front (Bosart and Bartlo, 1991). A surface front off the Florida coast provided the initial low level vorticity required for cyclogenesis. Assuming deep saturated ascent in a moist neutral environment, a small

scale cyclone of tropical storm intensity forms in their simulation after approximately 61 hours. They propose that similar mechanisms may also operate in the deep tropics.

Gray (1968, 1975) found that upper level forcing causes approximately 15% of the global total of tropical cyclones, with an additional 3-5% of the total storms forming in subtropical latitudes in association with stagnant frontal zones and upper level forcing.

Reilly (1992) offers observational support to the upper level forcing hypothesis. He calculates a forcing parameter that measures an average differential PV advection near the tropopause using NMC (National Meteorological Center) global analyses for 11 tropical storms that occured in 1991 in the Northern West Pacific. He concludes that five of the storms studied may have been connected to the presence of a TUTT. The inclusion of non-developing storms in this kind of study may help in establishing the importance of TUTTS in tropical cyclogenesis. The JTWC (Joint Typhoon Warning Center), however, reported that none of the Western North Pacific tropical cyclones in 1991 were TUTT induced, even though the TUTT was often present during the summer (JTWC, 1991). Moreover, in a study of two years of tropical cyclone genesis in the Northern West Pacific, Zehr (1992) finds that the TUTT is just as common near non-developing cloud clusters as it is near developing ones.

From the above discussion, it becomes clear that although is has long been recognized that upper level anomalies participate in tropical cyclone genesis, the modes of interactions and the frequency with which they occur are still the subject of debate. A better observational network is required to shed light on this problem.

In Zehnder and Gall (1991a, b), Zehnder (1991) and Zhong *et al.* (1993), another mechanism for tropical cyclogenesis that is probably unique to the Eastern North Pacific is discussed. This basin is a peculiar region because it is located downwind of the Sierra Madre Mountains in Central America and has the highest frequency of tropical cyclone genesis per unit area in the world (Renard and Bowman, 1976). Zehnder and his collaborators investigate the possibility that this enhanced tropical cyclogenesis region exists due to lee cyclogenesis caused by the interactions of certain southeasterly flows with the Central American Sierra Madre mountains. Evidence supporting this hypothesis was gathered using both observations (Zehnder and Gall, 1991a; Mozer and Zehnder, 1994) and numerical

models. Numerical results (Zehnder and Gall, 1991b; Zehnder, 1991) show that for the actual orientation, shape and dimensions of the Sierra Madre mountains, a southeasterly flow impinging on the mountains will produce a train of waves to the west of the mountains. This wave train has a cyclonic vorticity maximum just west of the mountains and a secondary maximum located $1000 - 2000\ km$ downstream. The dimensions of the first of these cyclonic maxima are comparable to those of mesoscale vortices that are observed to precede cyclone genesis, but its intensity is at least one order of magnitude smaller than that of the observed initial mesoscale vortex (Zehnder, 1991). They also suggested that the formation of a wave train to the west of the mountain may explain episodes of almost simultaneous formation of more than one tropical cyclone in the Eastern Pacific (see figure 1.3 for an example). The persistent southeasterly wind required to produce lee cyclogenesis is hypothesized to be associated with planetary scale Rossby waves in the troposphere (Zehnder, 1991). Zhong *et al.* (1993) use several years of NMC analyses to show that there is good correlation between years with enhanced Rossby wave activity in the tropics and years with above average tropical cyclone genesis in the East Pacific. Nevertheless, it seems that perhaps rather than explaining the existence of the initial mesoscale vortex, lee cyclogenesis explains the increased frequency of more mesoscale convective systems (MCS) on the west side of the Sierra Madres as initially proposed in Velasco and Fritsch (1987). This increased frequency of occurrence of MCSs would then improve the probability of tropical cyclone genesis perhaps through the mechanism described below.

1.1.3 A Conceptual Model for Tropical Cyclogenesis

A common problem among the tropical cyclogenesis theories discussed above is the need for a weak pre-existing cyclonic vortex for the proposed mechanisms to act. Since tropical cyclogenesis is the evolution from a tropical disturbance (wherein no persistent and well defined mesoscale cyclonic vortex exists) to a tropical storm (which contains a mesoscale cyclonic vortex), these theories only describe the later stages of cyclogenesis.

Thus far, a single linear or nonlinear instability of the mean flow has not been able to thoroughly explain the transition from a tropical disturbance to a tropical storm. A different approach to this problem is proposed in Ooyama (1982). He envisioned the

genesis process as a series of events, with the probability of further evolution increasing as it proceeds. Zehr (1992) and Emanuel (1993) propose similar conceptual models of tropical cyclone genesis that contain this probabilistic nature proposed by Ooyama (1982).

It is useful at this point to review a key concept in understanding the dynamics of tropical cyclonegenesis, the Rossby radius of deformation (R_D). In an axisymmetric system, R_D is defined as

$$R_D = \frac{NH}{(f+\zeta)^{1/2}(f+2V/r)^{1/2}} \tag{1.1}$$

where N is the Brunt-Väisälä frequency, H is the equivalent depth, f is the planetary vorticity, ζ is the relative vorticity of the disturbance and V is the tangential velocity at radius r. Inertial stability is included in the definition of R_D because it is directly proportional to the efficiency of a given forcing in producing a balanced circulation (Schubert and Hack, 1982; Hack and Schubert, 1986). The Rossby radius of deformation separates scales of motion in which balanced dynamics prevails from those dominated by non-balanced dynamics. For instance, given a certain forcing of radius r, if $r \ll R_D$, the disturbance is dynamically small (Cotton *et al.*; 1989), and geostrophic adjustment dictates that most of the energy will be dispersed away with transient gravity waves. In a dynamically large disturbance ($r \geq R_D$), on the other hand, little energy propagates away with gravity waves, most of it being used to produce a balanced rotating circulation (Schubert *et al.*, 1980). Thus, the above discussion implies that it is difficult to force a balanced vortex in a dynamically small disturbance, because in such a system the forcing will mostly excite transient gravity waves.

Due to their small ζ and N and the low latitudes they form at, tropical disturbances are an example of dynamically small systems. Consequently, tropical cyclone genesis, *i.e.* the formation of a dynamically large tropical storm within a dynamically small tropical disturbance, requires a local decrease in the Rossby radius of deformation. From equation (1.1) it is clear that at any fixed latitude, R_D can only be decreased by either increasing the relative vorticity or decreasing the local static stability. Both of these processes are believed to be involved in tropical cyclone genesis, as explained below.

Zehr (1992), proposes a conceptual model of tropical cyclone genesis that possesses the probabilistic nature described in Ooyama (1982). Based on observations of 52 Northern West Pacific tropical storms during 1983-1984, he proposes the two stage conceptual model for tropical cyclogenesis illustrated in Fig. 1.1. The environmental thermodynamic and dynamic parameters previously mentioned (Gray, 1975) must be favorable at all times during the proposed tropical cyclone genesis process. In stage 1 of genesis, a low level wind surge enhances convergence in a tropical disturbance initiating an MCS. embedded within the favorable environment of a tropical disturbance. In the stratiform region of this MCS, an inertially stable warm core mesoscale vortex is produced by mechanisms to be discussed later. This mesoscale convectively generated vortex (MCV) is typically $150 - 300$ km in diameter and may persist for a few days after the parent MCS has dissipated, providing the tropical atmosphere with a region of decreased R_D. A second low level wind surge may then fortuitously initiate a new episode of active convection in the vicinity of the existing MCV, marking the beginning of stage 2 of genesis. If the spatial scale of this new convective region is comparable to the local reduced R_D, the efficiency of the latent heating in intensifying the existing balanced cyclonic circulation is high. At this point, a minimal tropical storm exists that will intensify provided that the environmental conditions continue being propitious.

Although initially proposed for the Western Pacific, the sequence of events that compose this conceptual model of tropical cyclone genesis is also observed in the Atlantic and E. Pacific basins (Zehr, 1993) and it is believed to be possible in all regions where genesis takes place.

However, several steps of this observationally devised conceptual model for cyclogenesis need to be physically understood through further theoretical, modeling and observational studies before a complete picture of tropical cyclone genesis emerges.

For instance, mesoscale convective systems are observed to produce MCVs both in midlatitudes (Brandes, 1990, Bartels and Maddox, 1991; Johnson and Bartels, 1992) and in the tropics (Velasco and Fritsch, 1987; Zehr, 1992; Emanuel *et al.*, 1993). However, the processes that lead to the formation of these vortices are still subject to investigation.

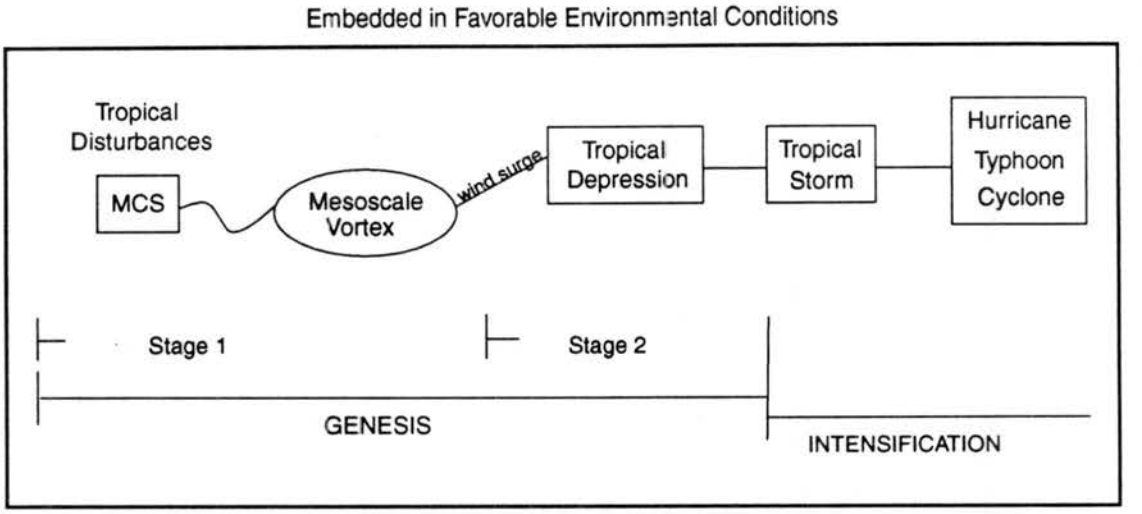

Figure 1.1: Schematical diagram of a conceptual model of tropical cyclone genesis proposed by Zehr (1992). See text for explanation

The formation of an MCV within the trailing stratiform region of an MCS is believed to occur mainly through vortex stretching (Hertenstein and Schubert, 1991; Weisman *et al.*, 1993; Chen and Frank, 1993). More specifically, midlevel convergence associated with the mesoscale circulations of the stratiform region and latent heating (Houze, 1989) act to locally amplify the vertical vorticity. This mechanism, however, is more efficient in the midlatitudes, where f is larger, than in the tropics. Tilting of horizontal vorticity also seems to play an important role in the initial production of the vortex (Brandes, 1990; Verlinde and Cotton, 1990). Observational studies in the midlatitudes corroborate these findings about the origin of the MCV (see Brandes, 1990; Verlinde and Cotton, 1990; Bartels and Maddox, 1991; Johnson and Bartels, 1992).

A better understanding of the origin of low level wind surges, as well as of their interaction with tropical disturbances is required. In the W. Pacific these low level wind surges were observed from all directions, with most of the cases having a westerly and/or southerly component (Zehr, 1992; Briegel, 1993). The origin of these wind surges is still not clear, among possible suggested mechanisms are tropical easterly waves, cross equatorial cold surges (Love, 1985) and equatorial waves.

Also, the mechanisms for formation of tropical disturbances and their embedded MCS need to be further understood. In this work a further step towards understanding some cases of tropical disturbance formation is taken.

Finally, it is important to remark that the mechanisms for tropical cyclogenesis reviewed above need not be exclusive, in the sense that in some cases, more than one of them may be acting cooperatively in the genesis of a tropical storm.

1.2 The Intertropical Convergence Zone

Given that approximately 80% of all the tropical cyclones on the globe form near or within the Intertropical Convergence Zone (Gray, 1968; ITCZ), it seems reasonable to search for mechanisms that favor tropical cyclogenesis within the dynamics of the ITCZ.

The ITCZ is a more or less continuous, narrow zonal belt of convection that circumscribes the earth within tropical latitudes. It is composed of hundreds of distinct tropical disturbances with horizontal scales on the order of a few hundred kilometers, separated by regions of relatively clear skies. In terms of circulation patterns, the ITCZ lies in the equatorial trough, which is the region where the trade winds from both hemispheres meet, and constitutes the ascending branch of the Hadley cell.

Two basic types of circulation patterns occur associated with the ITCZ, namely, the monsoon trough and the trade wind trough. The monsoon trough pattern typically occurs when the ITCZ is located farther than 10° away from the equator and is characterized by northeasterly (southeasterly) winds to the north (south) of the trough and southwesterly (northwesterly) winds between the trough and the equator in the Northern (Southern) Hemisphere. The trade wind trough is defined when the ITCZ is located within 10° of the equator and is characterized by northeasterly trades to the north and southeasterly trades to the south in either hemisphere.

1.2.1 A Climatology of the ITCZ

A climatology of the ITCZ calculated using a 17 year long Highly Reflective Cloud data set (Waliser and Gautier, 1993) is shown in Fig.1.2. Some of the evident characteristics of the ITCZ are pointed out below.

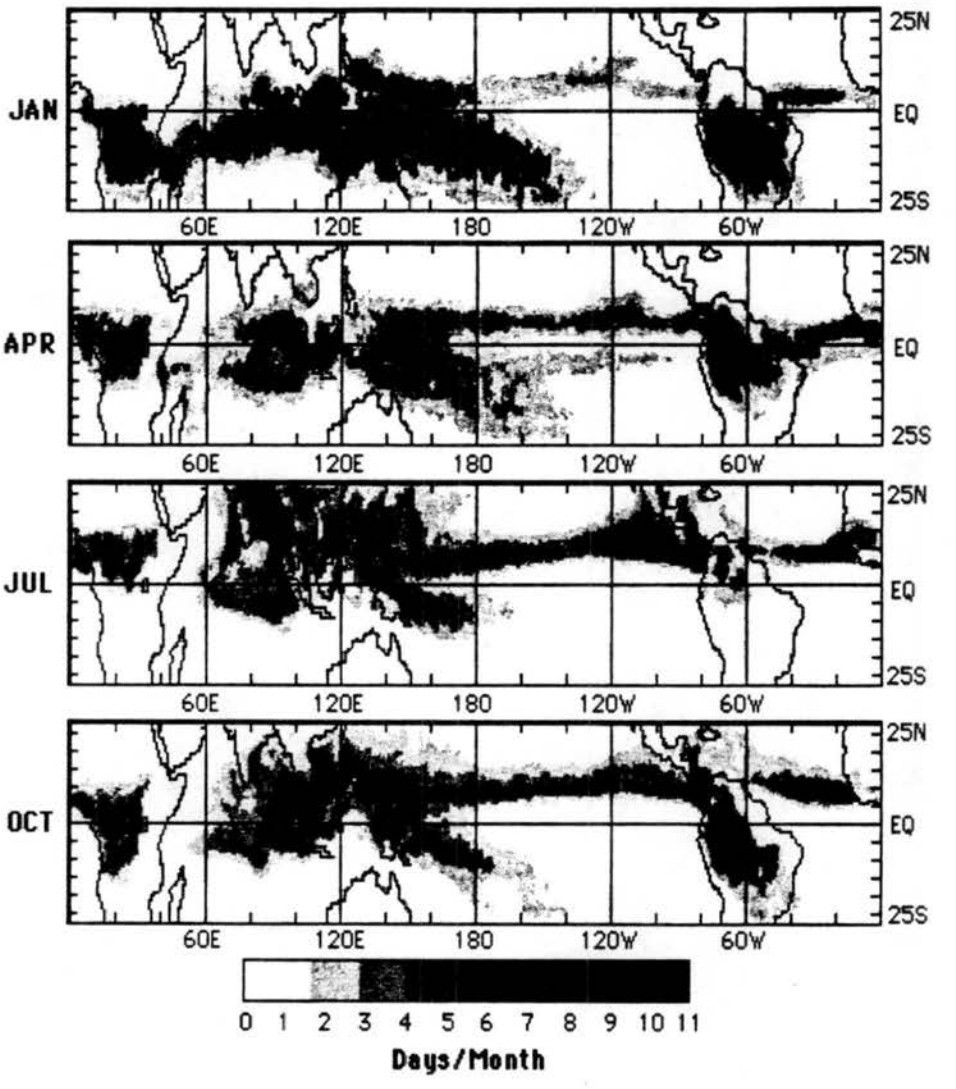

Figure 1.2: Mean monthly 'ITCZ' structure for *a)* January, *b)* April, *c)* July and *d)* October. These mean monthly images are based on 17 years of monthly HRC (Highly Reflective Cloud) data. Values represent the number of days per month that a given grid point was covered by a large-scale convective system.(From Waliser and Gautier, 1993).

In the Western Hemisphere, the ITCZ is remarkably zonally symmetric and remains in the Northern Hemisphere all year round, with the exception of the portion that lies over the American continent. In the Eastern Pacific, the ITCZ becomes wider in its easternmost part during the Northern summer, reflecting the migration of the ITCZ from the Amazon region to Central America.

The Eastern Hemisphere portion of the ITCZ shows less zonal symmetry than its Western Hemisphere counterpart and migrates between the Northern and Southern Hemispheres at all longitudes. In the Western Pacific warm pool, complicated ITCZ patterns emerge with the prevalent circulation being of the monsoon type. Two basic types of circulation are identified in the NW Pacific, namely, the linear monsoon trough and the less common monsoon gyres (Lander, 1993).

Although possessing mixed characteristics of both midlatitude frontal zones and the ITCZ, the subtropical frontal zones (Kodama, 1992), namely the South Pacific Convergence Zone (SPCZ), the South Atlantic convergence zone and the Baiu front are also evident in the ITCZ climatology presented in figure 1.2. In the South Western Pacific, it is interesting to note that the SPCZ is present all year round, with peak activity during the Southern summer.

The migration of the ITCZ across the equator in oceanic latitudes in the E. Hemisphere, allows the somewhat rare occurrence of twin tropical cyclones which will be further discussed in chapter 5.

1.2.2 Transience and Cyclogenesis within the ITCZ

Depending on the context in which it is studied, the ITCZ may be regarded as either a stationary or a transient feature of the tropical atmosphere. The stationary approach is usually adopted in general circulation or climatology studies. The transient approach must be followed when daily and zonal variations of the ITCZ are considered.

The ITCZ breakdown is a transient phenomenon which is hypothesized to aid in setting the stage for certain cases of tropical cyclogenesis. In satellite images, the ITCZ is sometimes observed to undulate, forming cloud patterns that resemble *inverted V's* (Frank, 1969b). At times, this undulating ITCZ breaks down (Agee, 1972) into several

tropical cyclones. This process is referred to as ITCZ breakdown. These tropical cyclones then move into higher latitudes allowing the ITCZ to reform and perhaps start the cycle over again.

A classical example of ITCZ breakdown that occurred in the E. Pacific in July of 1988 is shown in figure 1.3. From July 27 through July 30, five tropical depressions formed in the E. Pacific within about 9° longitude of each other. Four of these depressions became named storms (Gerrish and Mayfield, 1989). On July 26, the ITCZ was an elongated zonal band of convection centered at about $10°N$. Two days later, on July 28, the ITCZ is undulating, resulting in its breakdown into a series of tropical cyclones by August 3. These tropical cyclones then moved into higher latitudes allowing the ITCZ to reform by August 10. In the 1988 hurricane summary, Avila and Clark (1989) report that all of the E. Pacific tropical storms during 1988 were initiated by African easterly waves.

The aforementioned undulations of the ITCZ may be related to the previously discussed tropical easterly waves. These waves are believed to result from combined barotropic and baroclinic instability of the mean zonal flow. In the African region the origin of this unstable mean flow is believed to be related to the strong underlying meridional temperature gradients (Burpee, 1972; Norquist *et al.*, 1977). However, the inexistence of similar temperature gradients in other regions where easterly waves are observed make it necessary to find alternative mechanisms for the production of unstable mean flows and easterly waves outside the tropical Atlantic. The mechanism studied here and previously in Hack *et al.* (1989), Schubert *et al.* (1991, 1992) and Guinn (1992) is also combined barotropic and baroclinic instability of the zonal flow. The difference is that the meridional PV gradient reversal that is necessary for the occurrence of combined barotropic and baroclinic instability is instead hypothesized to have been produced by latent heat release in deep cumulus convection within the ITCZ. This mechanism is called ITCZ breakdown. The presence of the strong meridional temperature gradient at the surface in the African region may act as an enhancing factor. Evidence for this is that the magnitude of the meridional shear of the zonal wind is much stronger in the Atlantic (and African) region than in the Eastern Pacific.

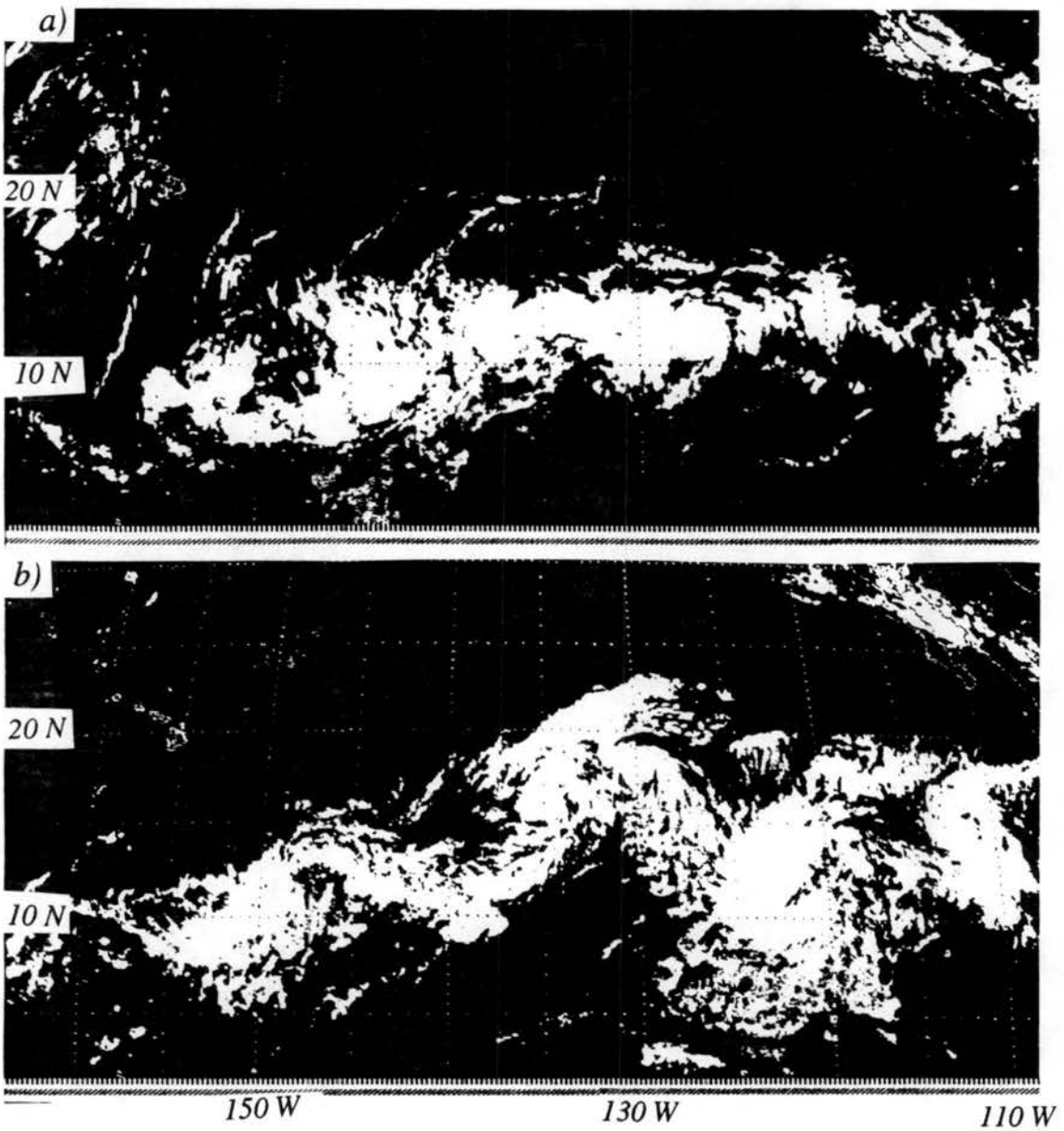

Figure 1.3: GOES IR images illustrating the ITCZ breakdown in the Eastern Pacific; a) 26 July, b) 28 July of 1988 at 16:46.

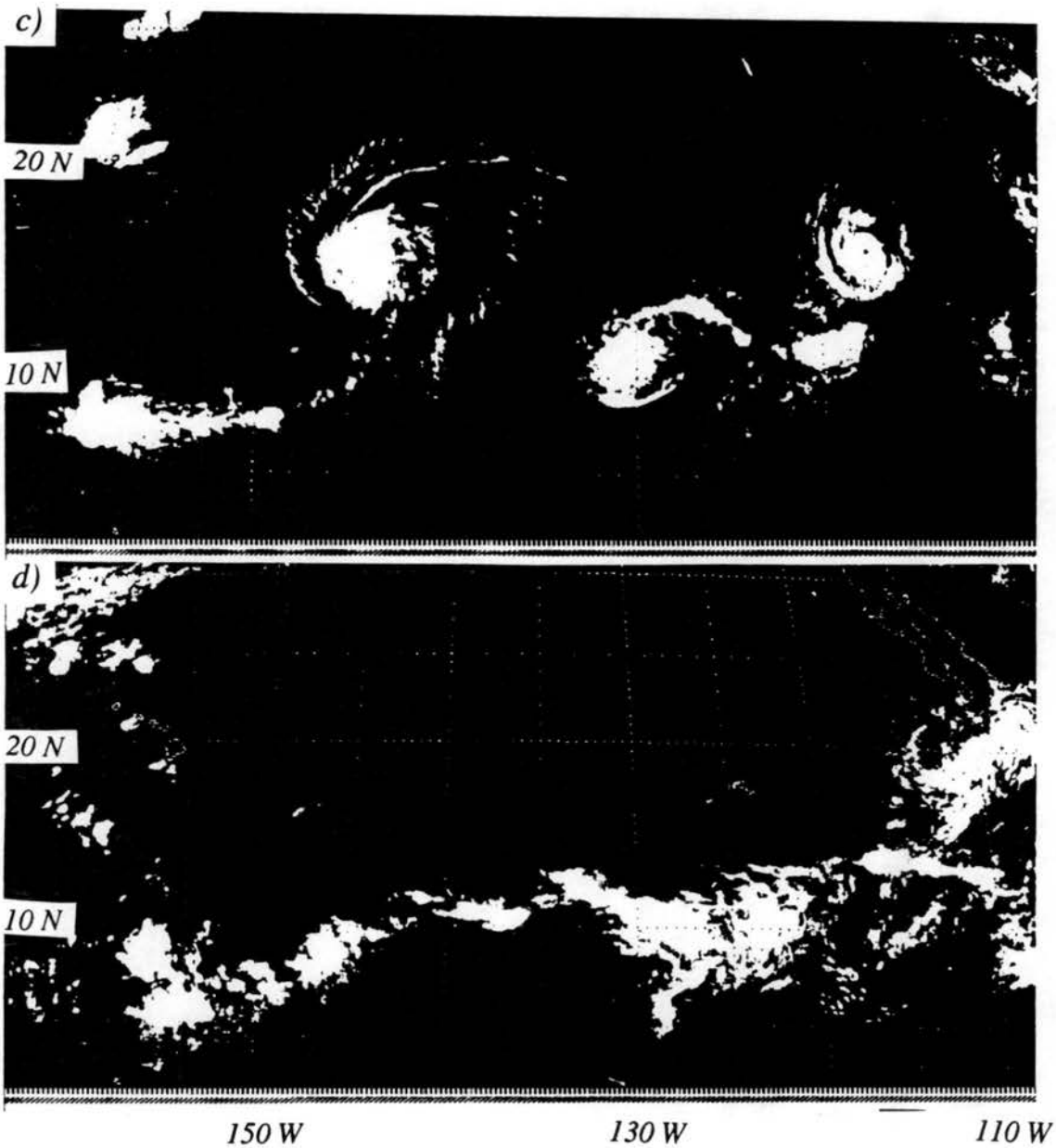

Figure 1.3: Continued; c) 3 August and d) 10 August of 1988.

The ITCZ breakdown is here hypothesized to be a mechanism for the formation of tropical disturbances. These tropical disturbances are large regions of increased vorticity and organized convection, therefore being a prime environment for the genesis of tropical cyclones. The ITCZ breakdown is proposed to explain the early stage of tropical cyclone genesis, namely, the formation of tropical disturbances.

Chapter 2 introduces the shallow water model which is used in this work. The numerical aspects of the model are presented in Appendix A. Given that the ITCZ breakdown results from an instability of the mean flow, the theory for instability of barotropic flows is reviewed in Chapter 3. The method used in the linear normal mode stability analysis of zonally symmetric vorticity strips on the sphere presented in Chapter 3 is outlined in Appendix B. Chapter 4 contains the results of model experiments which were designed to simulate the formation of tropical disturbances through the ITCZ breakdown process. The interactions between an idealized ITCZ and a nearby vortex are also shown in this chapter. A short climatology of Eastern Pacific tropical cyclone genesis was included to provide some observational support to the model results. In Chapter 5, the formation of the tropical disturbances that lead to twin tropical cyclogenesis is simulated. The effects of the movement of super cloud clusters associated with the Madden Julian Oscillation on twin tropical cyclone formation is also addressed. A short climatology of twin tropical cyclone formation is included. Finally, a summary of the results obtained and related conclusions are presented in Chapter 6.

Chapter 2

THE SHALLOW WATER MODEL

In this chapter, a review of the shallow water model used later on is presented. The model was developed by Hack and Jakob (1992) and is based on the shallow water equations solved globally on the sphere using the spectral transform method. A detailed description of this model is given in Hack and Jakob (1992). Nonetheless, a brief description of its governing equations is presented in section 2.1. Section 2.2 reviews the conservation principles pertinent to the shallow water equations, and section 2.3 discusses the usefulness of shallow water models in the study of tropical dynamics. Finally, section 2.4 discusses the model initialization, spatial truncation, time step and dissipation.

2.1 The Governing Equations

The shallow water equations describe the motion of a single layer of homogeneous, incompressible and hydrostatic fluid. On the sphere, these equations are

$$\frac{\partial u}{\partial t} + u\frac{\partial u}{a\cos\varphi\partial\lambda} + v\frac{\partial u}{a\partial\varphi} - \left(2\Omega\sin\varphi + \frac{u\tan\varphi}{a}\right)v = -\frac{\partial\Phi}{a\cos\varphi\partial\lambda} + F_u^{Diff} \tag{2.1}$$

$$\frac{\partial v}{\partial t} + u\frac{\partial v}{a\cos\varphi\partial\lambda} + v\frac{\partial v}{a\partial\varphi} + \left(2\Omega\sin\varphi + \frac{u\tan\varphi}{a}\right)u = -\frac{\partial\Phi}{a\partial\varphi} + F_v^{Diff} \tag{2.2}$$

$$\frac{\partial\Phi}{\partial t} + \frac{\partial(u\Phi)}{a\cos\varphi\partial\lambda} + \frac{\partial(v\Phi\cos\varphi)}{a\cos\varphi\partial\varphi} = Q + F_\Phi^{Diff} \tag{2.3}$$

where

$$F_u^{Diff} = -K_4\left[\frac{\nabla^4 u}{\cos\phi} - \frac{4u}{a^4}\right] \tag{2.4a}$$

$$F_v^{Diff} = -K_4\left[\frac{\nabla^4 v}{\cos\phi} - \frac{4v}{a^4}\right] \tag{2.4b}$$

$$F_\Phi^{Diff} = -K_4\nabla^4\Phi \tag{2.4c}$$

and u and v are the horizontal components of the wind, Φ is the geopotential height, a is the radius of the earth, Q is a mass sink or source, K_4 is a diffusion coefficient and φ and λ are latitude and longitude, respectively. The diffusion operators are added to control spectral blocking (*i.e.*, accumulation of energy in the smallest resolved scales) and the linear operators they contain are needed to prevent damping of solid body rotation (Jakob *et al.*, 1993). Equations (2.1)-(2.3) form a closed system in u, v and Φ. An equivalent closed system in δ, ζ and Φ is obtained by replacing the momentum equations with the divergence and vorticity equations. This is the so called vorticity/divergence form of the equations of motion and it is the form integrated in this model. The horizontal divergence and vertical vorticity equations are

$$\frac{\partial \delta}{\partial t} = \frac{1}{a(1-\mu^2)}\frac{\partial (V\eta)}{\partial \lambda} - \frac{\partial (U\eta)}{a\partial \mu} - \nabla^2\left[\Phi + \frac{U^2+V^2}{2(1-\mu^2)}\right] - K_4(\nabla^4\delta - \frac{4}{a^4}\delta), \tag{2.5}$$

$$\frac{\partial \eta}{\partial t} = -\frac{\partial (\eta V)}{a\partial \mu} - \frac{1}{a(1-\mu^2)}\frac{\partial (\eta U)}{\partial \lambda} - K_4(\nabla^4\eta - \frac{4}{a^4}\eta), \tag{2.6}$$

where

$$\delta = \frac{\partial U}{a(1-\mu^2)\partial \lambda} + \frac{\partial V}{a\partial \mu}, \tag{2.7a}$$

$$\eta = \zeta + f = \frac{\partial V}{a(1-\mu^2)\partial \lambda} - \frac{\partial U}{a\partial \mu} + f, \tag{2.7b}$$

and $U = u\cos\varphi$, $V = v\cos\varphi$, $\mu = \sin\varphi$ and $f = 2\Omega\sin\varphi$ (which is the Coriolis parameter).

The mass conservation equation may be written as

$$\frac{\partial \Phi'}{\partial t} = -\frac{1}{a(1-\mu^2)}\frac{\partial (U\Phi')}{\partial \lambda} - \frac{\partial (V\Phi')}{a\partial \mu} - \overline{\Phi}\delta + Q - K_4\nabla^4(\overline{\Phi} + \Phi') \tag{2.8}$$

if the geopotential is given by $\Phi(\lambda,\varphi,t) = \overline{\Phi} + \Phi'(\lambda,\varphi,t)$.

The Helmholtz theorem states that a horizontal velocity vector ($\mathbf{V} = \mathbf{i}u + \mathbf{j}v$) may be written as the sum of a rotational part plus a divergent part, that is:

$$\mathbf{V} = \mathbf{k} \times \nabla\psi + \nabla\chi \tag{2.9}$$

where ψ and χ are a scalar streamfunction and velocity potential, respectively and $\mathbf{i}$, $\mathbf{j}$, and $\mathbf{k}$ are the zonal, meridional and vertical unit vectors. From (2.9), in spherical coordinates

U and V may be written as:

$$U = \frac{\partial \chi}{a \partial \lambda} - \frac{(1-\mu^2)}{a} \frac{\partial \psi}{\partial \mu} \tag{2.10}$$

$$V = \frac{\partial \psi}{a \partial \lambda} + \frac{(1-\mu^2)}{a} \frac{\partial \chi}{\partial \mu} \tag{2.11}$$

The prognostic variables η and δ may be obtained as functions of ψ and χ by substituting (2.10) and (2.11) into (2.7):

$$\eta = \nabla^2 \psi + f \tag{2.12}$$

$$\delta = \nabla^2 \chi \tag{2.13}$$

The use of (2.12) and (2.13) eases matters because the Laplacian operator has a simple form in a spectral space whose basis functions are spherical harmonics (see Appendix A).

Substitution of (2.10) through (2.13) into (2.5), (2.6) and (2.8) yields a non-linear system of prognostic equations for ϕ, χ and Φ, that will be solved using the spectral transform method in space and semi-implicit time differencing. In order to start the integration in time, initial fields of either η, δ and Φ or U, V and Φ on the transform grid are required. For each time step the model calculates all non-linear terms and diabatic processes in the transform grid. Then it transforms all variables into spectral space where the linear terms, derivatives and time tendencies are evaluated. Finally all variables are transformed back to physical space and one cycle of the integration is completed. For more information on the numerical aspects of the model, see Appendix A.

2.2 Conservation Principles

For the sake of completeness, the conservation principles pertinent to the shallow water model (neglecting the dissipation terms) will be presented in this section. These are conservation of energy, angular momentum and potential vorticity.

The principle of conservation of potential vorticity is obtained by combining equations (2.3) and (2.6)

$$\frac{dq}{dt} = -q \frac{Q}{\Phi} \tag{2.14}$$

where the potential vorticity, q, which is given by

$$q = \frac{\eta}{\Phi}, \tag{2.15}$$

and the total derivative by

$$\frac{d}{dt} = \frac{\partial}{\partial t} + u\frac{\partial}{a\cos\phi\partial\lambda} + v\frac{\partial}{a\partial\phi}. \tag{2.16}$$

It is evident from (2.14) that in the absence of any mass sinks or sources, potential vorticity is conserved following the motion of a particle. If, on the other hand, a mass source (sink) is present, potential vorticity will decrease (increase).

The total energy (kinetic plus potential) conservation principle is obtained by taking (2.1)$\cdot\Phi u$+(2.2)$\cdot\Phi v$ and adding it to (2.3) $\cdot$ $[(u^2+v^2)/2+\Phi]$, which results in

$$\frac{\partial[\Phi(K+\frac{P}{2})]}{\partial t} + \frac{\partial[(K+P)u\Phi]}{a\cos\phi\partial\lambda} + \frac{\partial[(K+P)v\cos\phi\Phi]}{a\cos\phi\partial\phi} = Q(K+P) \tag{2.17}$$

where $K = (u^2+v^2)/2$ and $P = \Phi$ are the kinetic and potential energy per unit mass, respectively. Integrating (2.17) over the whole domain of the sphere results in the conservation relation

$$\frac{d}{dt}\int_0^{2\pi}\int_{-\pi/2}^{\pi/2}\Phi(K+\frac{P}{2})a\cos\phi d\lambda d\phi = \int_0^{2\pi}\int_{-\pi/2}^{\pi/2}Q(K+P)a\cos\phi d\lambda d\phi, \tag{2.18}$$

i.e., in the absence of mass sources or sinks and friction effects, total energy is conserved when integrated over the surface of a sphere.

Finally, the angular momentum conservation principle is given by

$$\frac{dM}{dt} = -\frac{\partial\Phi}{\partial\lambda}, \tag{2.19}$$

where $M = (\Omega a\cos\phi + u)a\cos\phi$ is the angular momentum. Integration of (2.19) over the entire domain of the sphere, gives

$$\frac{d}{dt}\int_0^{2\pi}\int_{-\pi/2}^{\pi/2}M\Phi a\cos\phi d\lambda d\phi = \int_0^{2\pi}\int_{-\pi/2}^{\pi/2}[(Q+F_\Phi^{Diff})M]a\cos\phi d\lambda d\phi, \tag{2.20}$$

i.e., angular momentum integrated over the sphere is conserved, when mass sinks or sources and friction effects are absent.

The conservation principles derived in this section will become useful in the derivation of flow stability theorems to be presented in chapter 3. They will also be referred to in that chapter for the derivation of a conservative quantity of the perturbed flow, the so-called wave activity.

2.3 Use of Shallow Water Models in Tropical Dynamics

The use of simple models in meteorology is advantageous because it allows easier isolation of the processes that are important to explain a given atmospheric phenomenon. The shallow water system presented in section 2.1 is an example of a simple model of the atmosphere which is especially useful in the study of tropical dynamics. The reason for its usefulness is that a scale analysis of the equations of motion shows that, outside regions of convection, synoptic scale tropical motions are approximately barotropic and non-divergent (Charney, 1963; Holton, 1992). Within regions of convection, however, divergent effects become very important and the barotropic non-divergent equations are no longer valid. The barotropic divergent equations (also known as shallow water equations) are more appropriate for studies that include the effects of tropical convection.

Further justification for the use of a shallow water model in tropical dynamics is offered below. In a linear, compressible atmosphere, it is possible to separate the horizontal structure of motion from its vertical structure (Silva Dias *et al.*, 1983; Fulton and Schubert, 1985). Such an atmosphere may then be seen as a linear combination of numerous sets of shallow water equations with different equivalent depths ($\overline{\Phi}/g$) and different corresponding vertical structures. For a disturbance of fixed size, different $\overline{\Phi}$ have different Rossby radii of deformation, which will imply different partitions of energy between geostrophic and gravity modes. Fulton and Schubert (1985) applied a vertical normal mode transform to apparent heat source profiles obtained in the Marshall Islands and GATE (Global Atmosphere Research Program - Atlantic Tropical Experiment) and found that important contributions to the forcing of the mass field come from vertical modes with speed in the $30 - 70\,m/s$ range (or $\overline{\Phi}$ between $900 - 4900\,m^2/s^2$). Since most of the energy produced by convective forcing is projected onto a single vertical mode (typically the first or second internal mode), the use of a single shallow water layer should be a good approximation to the tropical circulation. This approach has been previously used in linear studies by Gill (1980), Silva Dias *et al.* (1983), and others.

In order to simulate the effects of convection in a shallow water model, it is necessary to understand its effect in the real atmosphere. Organized cumulus convection in the

tropics has the net effect of moistening and warming the large scale environment. The warming is associated to adiabatic compression in the large scale compensating subsidence and the moistening is due to the detrainment of water from the clouds (Yanai *et al.*, 1973). This convective heating produces a positive PV anomaly when located in the Northern Hemisphere. According to the PV equation (2.14), in a shallow water model, a mass sink produces a positive (negative) potential vorticity anomaly in the Northern (Southern) Hemisphere. Therefore, in a shallow water model, convective heating is simulated by a mass sink (Q) introduced in the continuity equation (2.3).

2.4 Model Initialization

Time integration of the shallow water model described in chapter 2 requires knowledge of the initial mass and momentum fields. Initialization of the model in cases where the initial wind fields are at rest and the fluid depth is constant is straightforward. If, however, the initial state is not a resting one, the model should be initialized with balanced mass and wind fields in order to keep initial transient gravity waves to a minimum.

In the model simulations to be shown next, given the initial relative vorticity, the wind and geopotential fields are obtained therefrom as follows. Assuming initially nondivergent flow, the streamfunction Ψ is obtained from the vorticity through

$$\zeta = \nabla^2 \Psi, \tag{2.21a}$$

and the corresponding nondivergent wind field is given by

$$U = \frac{(1-\mu^2)}{a}\frac{\partial \Psi}{\partial \mu} \quad \text{and} \quad V = \frac{\partial \Psi}{a \partial \lambda} \tag{2.21b}$$

where (2.21a,b) are obtained from (2.10-2.12). At this point, it is assumed that the mass and wind fields obey a nonlinear balance relation which is obtained by setting the local time variation of divergence to zero in (2.5) (Haltiner and Williams, 1980) resulting in

$$\nabla^2 \Phi = \frac{1}{a(1-\mu^2)}\frac{\partial (V\eta)}{\partial \lambda} - \frac{\partial (U\eta)}{a \partial \mu} - \nabla^2 \left[\frac{U^2+V^2}{2(1-\mu^2)}\right] \tag{2.22}$$

Therefore, given a vorticity field, equations (4.1a,b) and (2.22) are used to initialize the model. The nonlinear terms in these equations are calculated in physical space and the remaining terms are most easily computed in spectral space.

Table 2.1 shows the values of diffusion coefficients (K_4) and time steps used in simulations performed with $T126$ and $T213$ spectral truncations. According to Jakob *et al.* (1993), the diffusion coefficients scale as $[n(n+1)]^{-2}$ and are chosen to give a reasonably straight tail to the kinetic energy spectra. Figure 2.1 shows the rate of dissipation as a function of the wavenumber n. Dissipation increases towards higher wavenumbers. The use of $T126$ truncation implies stronger dissipation for all wavenumbers. Unless otherwise specified, it should be assumed that T213 was used in the shallow water experiments that will be shown herafter.

Spectral Truncation	Time Step (s)	$K_4\ (m^4/s)$
T126	2400	6.3×10^{13}
T213	1200	8.0×10^{12}

Table 2.1: Time steps and K_4 used with $T126$ and $T213$ spectral truncations.

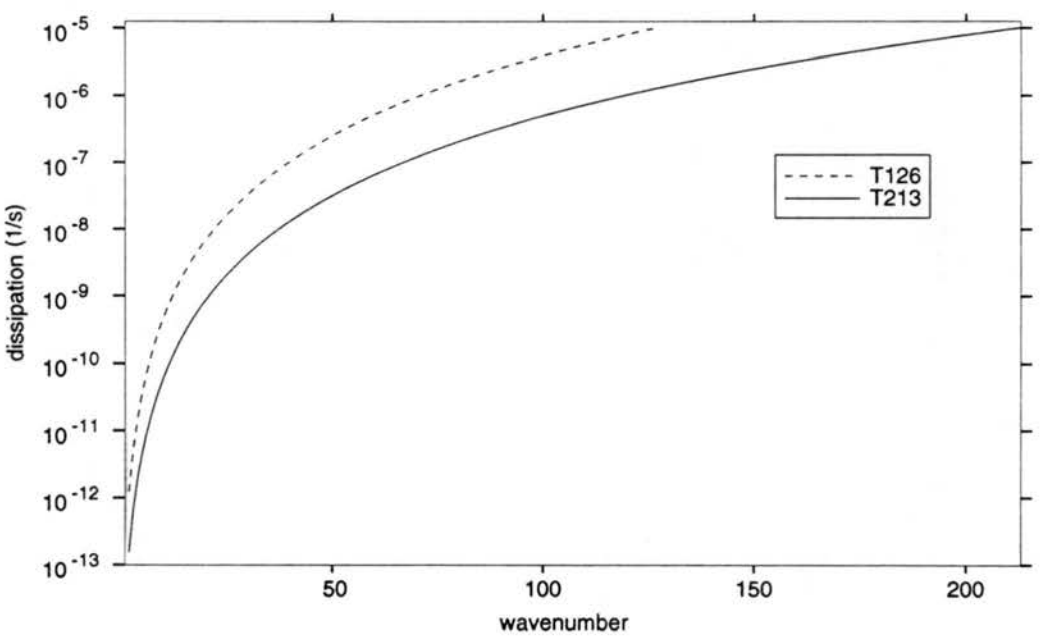

Figure 2.1: Rate of dissipation as a function of wavenumber, n.

The time steps shown in table 2.1 are consistent with the use of a semi-implicit time integration scheme (Appendix A). In a semi-implicit time scheme, the time step

is constrained by the propagation speed of the Rossby modes, rather than that of the gravity modes. This allows larger time steps than would be possible with an explicit time integration scheme.

Note that although the shallow water model used in this work is on the sphere, only the results in selected regions of interest are shown.

Chapter 3

STABILITY STUDIES

The study of stability of idealized basic state flows in the presence of small perturbations is a classical problem in fluid dynamics.

Traditionally, flow stability has been studied within the context of linear normal mode dynamics. Nevertheless, linear stability does not guarantee stability in general. First, the classical linear normal mode approach taken to study linear stability, leaves out possible algebraically growing unstable modes that are part of the continuum frequency spectrum (Case, 1960; Farrel, 1982). Then, there is the question of whether or not linear stability will carry over to nonlinear dynamics in each specific case. a linearly stable mode may either excite unstable modes through nonlinear interactions or simply evolve outside the ambit of linear dynamics. Examples of nonlinear stable evolutions that do not have linear counterparts are wave breaking (Dritschel, 1986; McIntyre and Palmer, 1983 and 1984; Juckes and McIntyre, 1987; Polvani and Plumb, 1992) and vacillation (Dritschel, 1986).

For both linear and nonlinear flows, theorems that establish sufficient conditions for the stability of the flow have been derived. The inherent differences between the concept of instability in linear and nonlinear flows become crucial in the procedures used to obtain their respective stability theorems. In linear dynamics there is no conservation of total energy and the disturbances can continuously draw energy from the basic state and grow unbounded. In nonlinear dynamics, on the other hand, conservation of energy imposes an upper limit on how much energy can be extracted from the basic state by the perturbations, ultimately imposing an upper bound on the size that the disturbance can attain. These inherent differences are reflected in the kinds of stability theorems that can be obtained in each case. In linear normal mode dynamics, stability theorems are derived in such

a way as to guarantee that no exponentially growing normal modes exist. In nonlinear dynamics, on the other hand, stability theorems must establish upper bounds for the growth of disturbances.

Linear stability theorems exist for both the nondivergent and divergent barotropic equations, the quasi geostrophic and semi geostrophic theories. In nonlinear dynamics, stability theorems exist for the nondivergent barotropic flow.

In section 3.1, stability theorems for linear barotropic divergent and non-divergent flows on the sphere are reviewed. A linear normal mode stability analysis of zonally symmetric vorticity strips on the surface of a rotating sphere is presented in section 3.2. Finally, section 3.3 presents derivations of a conservative quantity of the perturbation flow called wave-activity.

3.1 Stability Theory

The simplest possible context in which barotropic instability occurs was described by Rayleigh (1945). It consists of a plane parallel sheared flow, $\overline{u}(y)$, in a nonrotating, unstratified and inviscid fluid. Rayleigh's inflection point theorem states that *a necessary, but not sufficient, condition for instability in this flow is that* $d^2\overline{u}/dy^2$ *changes sign somewhere within the fluid.* Then, if small perturbations are superimposed on this flow, barotropic instability may occur and the perturbations may grow by drawing kinetic energy from the mean flow.

As a review and for the sake of completeness, the derivations of stability theorems for two cases which are relevant in this work will be presented next. First, the theorem for linear stability of barotropic nondivergent flow on the sphere is presented (Schubert *et al.*, 1992). Then, a theorem derived in Ripa (1983) for the stability of linear barotropic divergent flow on the sphere is shown. Schubert *et al.* (1991) shows a theorem derived by Arnol'd, which sets bounds to the nonlinear growth of perturbations in a barotropic non-divergent flow.

3.1.1 Linear Barotropic Nondivergent Stability Theorem

Starting with the barotropic nondivergent equations linearized with respect to a time and longitude independent zonal flow, $(u, v) = (\overline{u}(\phi) + u'(\lambda, \phi, t), v'(\lambda, \phi, t))$

$$\frac{\mathcal{D}\zeta'}{\mathcal{D}t} + v' \frac{d(\overline{\zeta} + f)}{a d\phi} = 0 \tag{3.1}$$

$$\frac{\partial u'}{a \cos\phi \partial\lambda} + \frac{v' \cos\phi}{a \cos\phi \partial\phi} = 0 \tag{3.2}$$

where,

$$\overline{\zeta} = -\frac{\partial(\overline{u}\cos\phi)}{a\cos\phi\partial\phi}, \quad \frac{\mathcal{D}}{\mathcal{D}t} = \frac{\partial}{\partial t} + \overline{u}\frac{\partial}{a\cos\phi\partial t}$$

$\frac{\mathcal{D}}{\mathcal{D}t}$ being the derivative following the basic state zonal flow, and

$$\zeta' = \frac{v'}{a\cos\phi\partial\lambda} - \frac{\partial(u'\cos\phi)}{a\cos\phi\partial\phi} \tag{3.3}$$

Now, define a perturbation meridional particle displacement, η', in the following manner

$$v' = \frac{D\eta}{\mathcal{D}t} \tag{3.4}$$

Substituting (3.4) into (3.1) and integrating in time gives

$$\zeta' + \frac{d(\overline{\zeta} + f)}{a d\mu}\eta\cos\phi = 0 \tag{3.5}$$

given that the perturbations initially obey:

$$\left[\zeta' + \frac{d(\overline{\zeta} + f)}{a d\mu}\eta\cos\phi\right]_{t=t_0} = 0 \tag{3.6}$$

Finally, the wave activity (A) conservation relation is obtained by multiplying (3.5) by $v'\cos\phi$

$$\frac{\mathcal{D}A}{\mathcal{D}t} = -v'\zeta'\cos\phi \tag{3.7}$$

with A given by

$$A = \frac{1}{2}\frac{d(\overline{\zeta} + f)}{a d\mu}\eta^2\cos^2\phi = \frac{1}{2}\zeta'^2\left[\frac{d(\overline{\zeta} + f)}{a d\mu}\right]^{-1} \tag{3.8}$$

Using (3.2) and (3.3) the wave activity conservation relation (3.8) is written as:

$$\frac{\partial A}{\partial t} + \frac{\partial[\overline{u}A + \frac{1}{2}(v'^2 - u'^2)\cos\phi]}{a\cos\phi\partial\lambda} + \frac{\partial[-u'v'\cos^2\phi]}{a\cos\phi\partial\phi} = 0 \tag{3.9}$$

which integrated over the sphere gives

$$\frac{d}{dt}\int\int A\, d\lambda d\mu = 0 \tag{3.10}$$

Since the integral in (3.10) is constant in time, the perturbations η' can only grow in an integrated sense if the meridional gradient of absolute vorticity changes sign somewhere in the domain. This is Rayleigh's famous stability theorem.

3.1.2 Linear Barotropic Divergent Stability Theorem

Ripa (1983) derived the necessary stability criteria for linear shallow water flow on a sphere. Given that a shallow water model on the sphere is used here, Ripa's theorem will be presented below.

The shallow water equations linearized with respect to a time and longitude independent mean zonal flow are given by:

$$\frac{\partial u'}{\partial t} + \frac{\overline{u}}{a\cos\phi}\frac{\partial u'}{\partial \lambda} + \frac{v'}{a}\frac{\partial \overline{u}}{\partial \phi} - \left(2\Omega\sin\phi + \frac{\overline{u}\tan\phi}{a}\right)v' + \frac{\partial \Phi'}{a\cos\phi\partial\lambda} = 0 \tag{3.11}$$

$$\frac{\partial v'}{\partial t} + \frac{\overline{u}}{a\cos\phi}\frac{\partial v'}{\partial \lambda} + \left(2\Omega\sin\phi + \frac{2\overline{u}\tan\phi}{a}\right)u' + \frac{\partial \Phi'}{a\partial\phi} = 0 \tag{3.12}$$

$$\frac{\partial \Phi'}{\partial t} + \frac{\overline{u}}{a\cos\phi}\frac{\partial \Phi'}{\partial \lambda} + \frac{v'}{a}\frac{\partial \overline{\Phi}}{\partial \phi} + \overline{\Phi}\left(\frac{\partial u'}{a\cos\phi\partial\lambda} + \frac{\partial(v'\cos\phi)}{a\cos\phi\partial\phi}\right) = 0 \tag{3.13}$$

The perturbation potential vorticity equation is derived similarly to (2.14)

$$\frac{\mathcal{D}q'}{\mathcal{D}t} + \frac{v'}{a}\frac{d\overline{q}}{d\phi} = 0 \tag{3.14}$$

the perturbation potential vorticity is

$$q' = \frac{1}{\overline{\Phi}}\left[\frac{\partial v'}{a\cos\phi\partial\lambda} - \frac{\partial(u'\cos\phi)}{a\cos\phi\partial\phi} - \overline{q}\Phi'\right] \tag{3.15}$$

which may also be obtained by linearizing the total potential vorticity given in (2.15). Also,

$$\overline{q} = \frac{1}{\overline{\Phi}}\left[-\frac{\partial(\overline{u}\cos\phi)}{a\cos\phi\partial\phi} + f\right] \tag{3.16}$$

The perturbation energy equation is derived by forming $(\overline{\Phi}u'+\Phi'\overline{u})\cdot$ (3.11) $+(\overline{\Phi}v')\cdot$ (3.12) $+(\overline{u}u' + \Phi')\cdot$ (3.13)

$$\frac{\partial E'}{\partial t} + \overline{\Phi}^2\overline{u}v'q' + \frac{\partial[(\overline{u}u' + \Phi')(\overline{\Phi}u' + \Phi'\overline{u})]}{a\cos\phi\partial\lambda} + \frac{\partial[(\overline{u}' + \Phi')\Phi v'\cos\phi]}{a\cos\phi\partial\phi} = 0 \tag{3.17}$$

where

$$E' = \overline{\Phi}\left(\frac{u'^2 + v'^2}{2}\right) + \Phi'\overline{u}u' + \frac{\Phi'^2}{2} \tag{3.18}$$

Integrated over the surface of the sphere, (3.17) becomes:

$$\int_0^{2\pi}\int_{-\pi/2}^{\pi/2}\left(\frac{\partial E'}{\partial t} + \overline{\Phi}^2\overline{\omega}a\cos\phi v'q'\right)\cos\phi d\phi d\lambda = 0 \tag{3.19}$$

where $\overline{\omega} = \overline{u}/(a\cos\phi)$ is the angular momentum associated with the basic state zonal flow.

Note here that in a linear problem there is no conservation of total energy $(\overline{E} + E')$ which implies that in an unstable flow, the perturbations may draw energy from the mean flow indefinitely and grow unbounded.

The equation for perturbation angular momentum is derived by taking $(\Phi' a\cos\phi)$ $\cdot$ (3.11)+$(u' a\cos\phi)\cdot$ (3.13), to obtain:

$$\frac{\partial M'}{\partial t} + \frac{\partial[(\Phi'^2 + \overline{\Phi}u'^2 - \overline{\Phi}v'^2 + 2\overline{u}\Phi'u')\cos\phi]}{2\cos\phi\partial\lambda} + \frac{\partial(\overline{\Phi}v'u'\cos^2\phi)}{\cos\phi\partial\phi} + \overline{\Phi}^2 v'q'a\cos\phi = 0 \tag{3.20}$$

where $M' = u'\Phi' a\cos\phi$. Integrating (3.20) over the surface of the sphere:

$$\int_0^{2\pi}\int_{-\pi/2}^{\pi/2}\left(\frac{\partial M'}{\partial t} + \overline{\Phi}^2 v'q'a\cos\phi\right)\cos\phi d\phi d\lambda = 0 \tag{3.21}$$

Multiplying equation (3.21) by an arbitrary constant, ω_0, and subtracting the result from (3.19) results in:

$$\int_0^{2\pi}\int_{-\pi/2}^{\pi/2}\left[\frac{\partial(E' - \omega_0 M')}{\partial t} + \overline{\Phi}^2 v'q'a\cos\phi(\overline{\omega} - \omega_0)\right]\cos\phi d\phi d\lambda = 0 \tag{3.22}$$

Now, making $v' = \mathcal{D}\eta/\mathcal{D}t$ (where η is an infinitesimal perturbation displacement in the meridional direction) in (3.14) and integrating in time results in:

$$q' = -\frac{\eta}{a}\frac{d\overline{q}}{d\phi} \tag{3.23}$$

Note that in order to obtain the equation above, the perturbations were required to obey:

$$\frac{\partial}{\partial\lambda}\left(q' + \eta\frac{d\overline{q}}{ad\phi}\right) = 0 \quad \text{and} \quad \left(q' + \eta\frac{d\overline{q}}{ad\phi}\right)_{t=0} = 0 \tag{3.24}$$

Multiplying (3.23) by v' gives:

$$v'q' = -\frac{\mathcal{D}}{\mathcal{D}t}\left(\frac{\eta^2}{2a}\frac{d\overline{q}}{d\phi}\right) \tag{3.25}$$

substituting (3.24) into (3.22) gives:

$$\frac{d}{dt}\int\int\left[E' - \omega_0 M' + \frac{1}{2}\overline{\Phi}^2\eta^2\frac{d\overline{q}}{ad\phi}(\omega_0 - \overline{\omega})a\cos\phi\right]\cos\phi d\phi d\lambda = 0 \qquad (3.26)$$

Now, it is necessary to determine under which conditions η^2 is not allowed to grow in an area integrated sense. Note that this implies that the flow is stable. From (3.26) it is clear that η^2 does not grow in an area integrated sense as long as $E' - \omega_0 M' \geq 0$ and $(\omega_0 - \overline{\omega})\cos\phi(d\overline{q}/d\phi) \geq 0$. Rewriting (3.18) as

$$E' = \frac{1}{2}\left[\overline{\Phi}\left(u' + \frac{\Phi'\overline{u}}{\overline{\Phi}}\right)^2 + \Phi'^2\left(1 - \frac{\overline{u}^2}{\overline{\Phi}}\right) + \overline{\Phi}v'^2\right] \qquad (3.27)$$

it is clear that if $\overline{u} \leq \overline{\Phi}$ then $E' \geq 0$. Also, since $E' - \omega_0 M'$ may be written as

$$E' - \omega_0 M' = \frac{\overline{\Phi}}{2}\left[\left(u' + \frac{\Phi'}{\overline{\Phi}}(\overline{\omega} - \omega_0)\,a\cos\phi\right)^2 + \frac{\Phi'^2}{\overline{\Phi}}\left(1 - \frac{(\overline{\omega} - \omega_0)^2 a^2\cos^2\phi}{\overline{\Phi}}\right)\right] \qquad (3.28)$$

if $[(\omega_0 - \overline{\omega})a\cos\phi]^2 \leq \overline{\Phi}$ then $E' - \omega_0 M' \geq 0$.

The above discussion leads to Ripa's stability theorem. Ripa (1983) states that *if there exists any value of* ω_0 *such that*

$$(\omega_0 - \overline{\omega})\cos\phi\frac{d\overline{q}}{d\phi} \geq 0 \quad \text{and} \quad [(\omega_0 - \overline{\omega})a\cos\phi]^2 \leq \overline{\Phi} \qquad (3.29a, b)$$

everywhere, then the flow is stable with respect to infinitesimal perturbations that obey (3.24). However, the above theorem does not ensure that the flow is inertially stable. Inertial stability is guaranteed if f and the potential vorticity, q, have the same sign everywhere (Holton, 1992).

Ripa (1983) also shows a corollary to this theorem which states that choosing $\omega_0 = max(\overline{\omega})$, a weaker sufficient condition for stability is obtained, namely that if:

$$\frac{d\overline{q}}{d\phi} \geq 0 \quad \text{and} \quad max(\overline{\omega}) \leq min\left(\overline{\omega} + \frac{\sqrt{\overline{\Phi}}}{a\cos\phi}\right) \qquad (3.30a, b)$$

everywhere, then the flow is stable with respect to infinitesimal perturbations that satisfy (3.24).

Ripa's theorem reduces to Rayleigh's inflection point theorem for the case of no rotation and $\overline{\Phi} \to \infty$ (nondivergence). In this case, (3.30b) is always obeyed regardless of the value of $\overline{\omega}$ or ω_0, and $d\overline{q}/d\phi \geq 0$ is the necessary, but not sufficient, condition for stability of the flow.

3.1.3 The Nature of Barotropic Instability

Hydrodynamic shear instabilities such as barotropic and baroclinic instabilities have been studied for over a century. The physical mechanism trough which Helmholtz instability (which is a limiting case of barotropic instability) occurs may be simply understood in terms of vorticity dynamics (Drazin and Reid, 1981). Nevertheless, the physical mechanisms involved in the making of barotropic and baroclinic instability are not yet well understood (Lindzen, 1988). Since it is argued here that barotropic instability is important in the ITCZ breakdown process, we shall concentrate on this kind of instability hereafter.

Returning to the subject of the mechanics of how barotropic instability occurs, it is certainly not intuitive how a reversal of sign of the gradient of potential vorticity leads to instability. Hoskins *et al.* (1985), Lindzen and Tung (1978), and Lindzen (1988) propose two different ways of looking at the physical mechanisms of barotropic instability. The former is discussed below.

Hoskins *et al.* (1985) present an explanation of the physical nature of barotropic instability in terms of the interactions between two counter propagating Rossby waves. Figure 3.1*a* shows the variation of vorticity with latitude produced by an idealized ITCZ in the NH. In the NH, the ITCZ convection produces a positive vorticity anomaly which is equivalent to introducing a mass sink in equation (2.14). Along the northern boundary of the high absolute vorticity region there will be an eastward propagating Rossby wave (with speed c_n) due to the locally reversed meridional absolute vorticity gradient. Along the southern boundary, however, there will be a westward propagating Rossby (with speed c_s) wave since there $d(\zeta + f)/d\phi > 0$. In figure 3.1*b* the two waves are depicted along with their induced circulations and their influence on each other. Note that the circulations related to the westward propagating wave influence the easterly propagating wave acting to slow it down (in a phase locking process) and amplify it. The eastward propagating wave has a similar effect upon the westward propagating wave. The end result is that the two waves amplify and propagate together at a speed c_r, or, as stated in Hoskins *et al.* (1985), *the induced velocity field of each Rossby wave keeps the other in step and makes the*

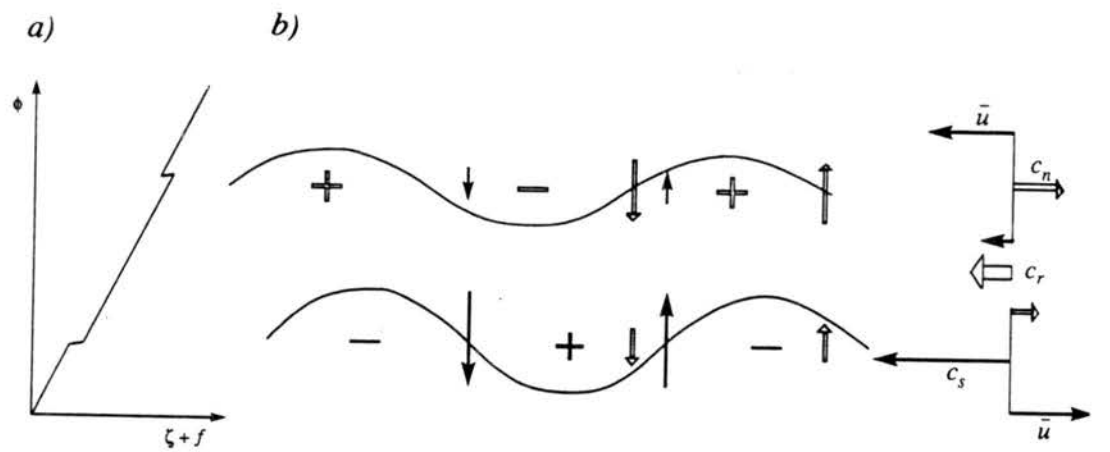

Figure 3.1: Interpretation of the physical mechanism for barotropic instability through the interactions between two counter propagating Rossby waves; *a)* Zonal wind and absolute vorticity meridional profiles for a three region model; *b)* schematic of the interactions between the two counter propagating waves. (See text for details).

other grow. For the two waves to interact in the way described they should be separated by a distance no farther than the horizontal scale of the waves. The same mechanism is proposed for the explanation of baroclinic instability, in which case the two waves would be stacked in the vertical.

3.2 Linear Normal Mode Stability Analysis of Vorticity Strips

It was shown in section 3.1 that a necessary, but not sufficient, condition for barotropic instability to occur is the existence of a meridional reversal of the absolute vorticity gradient. Once it is determined that a given basic state is barotropically unstable, a linear stability analysis is valuable as it offers a quantitative description of the favored patterns of instabilities and their respective growth rates.

Previous studies of stability of zonally symmetric vorticity strips on both the f (Guinn and Schubert, 1993) and β-planes (Kuo, 1973; Schubert *et al.*, 1992) have shown that *1)* the growth rate of the most unstable mode increases as the shear increases (by either increasing the vorticity of the strip or decreasing its width); *2)* the wavelength of the most unstable mode increases as the vorticity of the strip increases; and *3)* the wavelength of the most unstable mode increases as the width of the strip increases. On an f-plane in particular, it is possible to show that the wavelength of the most unstable mode is approximately eight times the width of the strip (see Guinn, 1992, for example). Using a three layer contour dynamics model on a non rotating sphere, Dritschel and Polvani (1992) found that the results summarized above for the planar case still hold. In addition, they find that *1)* strips of vorticity are more prone to become unstable on the sphere than on a planar surface; *2)* the closer a vorticity strip is to the equator, the easier it is for it to break down into small, long lived vortices; and *3)* contrary to what occurs in the planar case where an annular region of vorticity is stable to wavenumber two perturbations (Dritschel, 1989), on the sphere, wavenumber two perturbations do become unstable. Regarding the effect that adverse shear would have in stabilizing those vorticity strips, they conclude that when a thin vorticity strip is sufficiently far from the polar region, the adverse shear (Dritschel, 1986) due to the polar vortex is not sufficient to stabilize it.

In this section a linear normal mode stability analysis of zonally symmetric vorticity strips on the surface of a rotating sphere is performed still within the framework of the barotropic nondivergent equations. The method used for these calculations is delineated in Appendix B.

3.2.1 Stability Results

The linear normal mode stability of a vorticity strip of width α, with constant relative vorticity, ζ_r centered at a latitude ϕ_c is now studied using the method outlined in Appendix B. The number of equally spaced vorticity jumps used, J, was 200, which gives a meridional resolution of approximately 0.9 degrees. However, this resolution was doubled for strips narrower than 10° of latitude.

Fig. 3.2 shows the characteristics of the most unstable modes selected as a function of width and central latitude of vorticity strips in the NH with $\zeta_r = 3.0 \times 10^{-5} s^{-1}$. It is important to keep in mind that only integer wavenumbers are possible on the sphere. Note that for each latitude, there is a width beyond which the meridional vorticity profile becomes monotonical and therefore no instability occurs. The following conclusions may be drawn: *1)* wavenumber one and two modes become unstable on a rotating sphere, albeit with slower growth rates; *2)* the ratio between wavelength and width of the modes decreases with increasing width of the strip; *3)* the growth rate decreases slowly with latitude, presenting a sharper decrease towards the lower wavenumbers.

The dependency of the e-folding time and the wavenumber of the most unstable mode on the intensity of the vorticity strip is seen in figure 3.3. The vorticity strip is 7° wide and centered at $10°N$. Both the e-folding time and the wavenumber of the most unstable mode increase as the intensity of the strip decreases. This dependency is weak, however, for strips with $\zeta_s \geq 2.0 \times 10^{-5} s^{-1}$.

Figure 3.4 shows the growth rate of modes associated with vorticity strips whose $\zeta_s = 3.0 \times 10^{-5} s^{-1}$, centered at $10°N$ for varying widths.

The linear time evolution of a vorticity strip centered at $10°N$ and 7° wide is shown in Fig. 3.5. Meridional cross sections of the zonal wind and absolute vorticity are shown in figure 3.6. The latter shows a reversal in the meridional gradient of absolute vorticity,

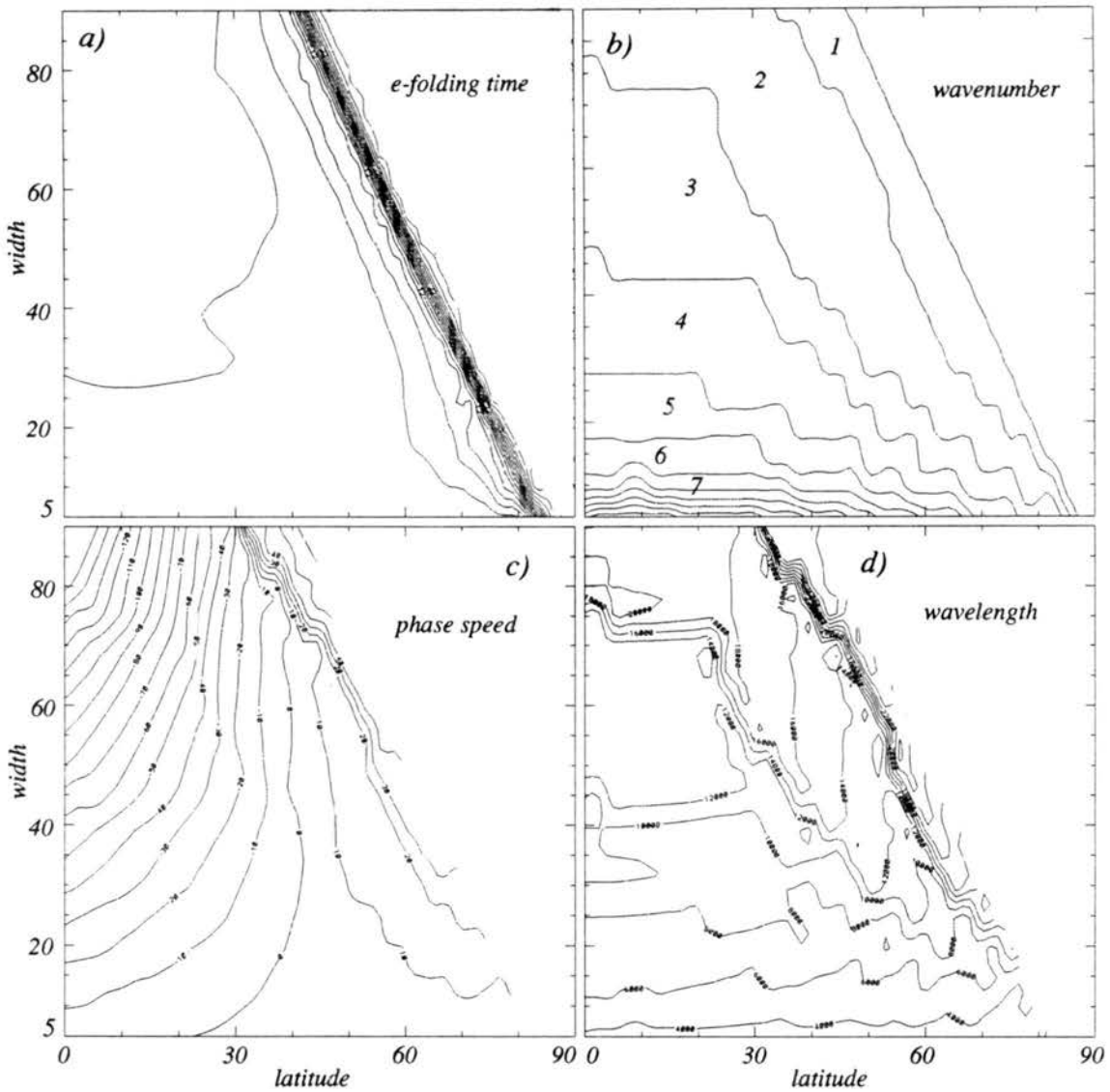

Figure 3.2: Stability characteristics of vorticity strips centered at a given latitude and with a certain width. it a) e-folding time (days), *b)* nondimensional wavenumber, *c)* phase speed (m/s), and *d)* wavelength (km).

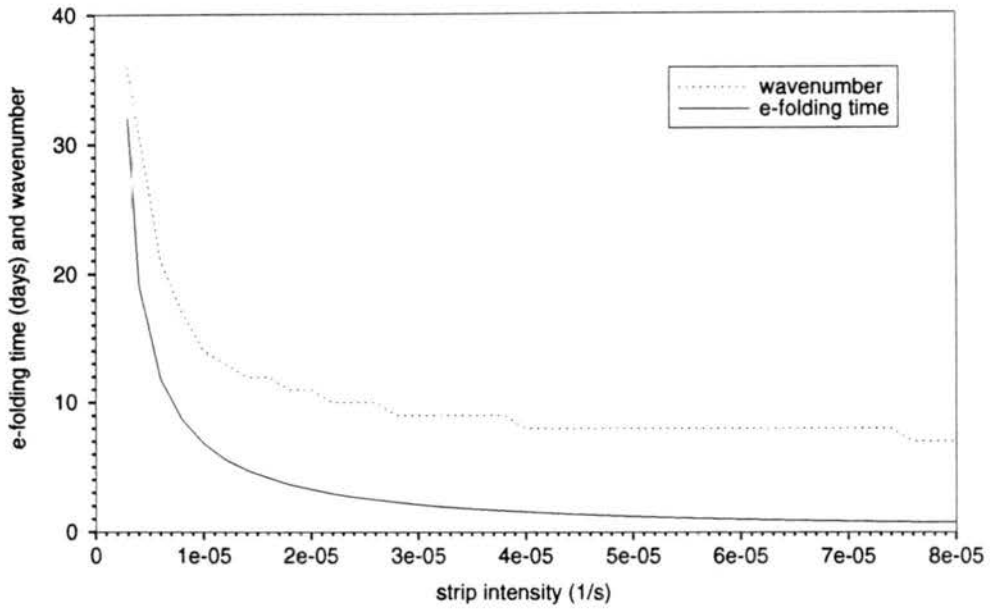

Figure 3.3: E-folding time and wavenumber of the most unstable mode as a function of the intensity of the vorticity strip.

indicating that the flow is prone to barotropic instability. Although this vorticity strip is unstable to wavenumber nine disturbances (see Fig. 3.2), only one wave is shown here. The streamlines are initially unperturbed and after eight e-folding time intervals, the barotropically unstable mode is evident leaning against the shear.

In addition, the results found in previous studies that the wavelength and growth rate of the instability increase with increasing shear are corroborated here.

3.3 Wave-activity Diagnostics

In this section, the concept of wave-activity is introduced and its mathematical formulation for certain cases is derived.

It is often convenient to decompose an atmospheric flow into a basic state and disturbances therefrom. After making this arbitrary decomposition of the flow, it is possible to derive a conservation relation for wave-activity (or generalized Eliassen-Palm relation) of the following form

$$\frac{\partial A}{\partial t} + \nabla \cdot \mathbf{F} = S + O(\alpha^3) \tag{3.31}$$

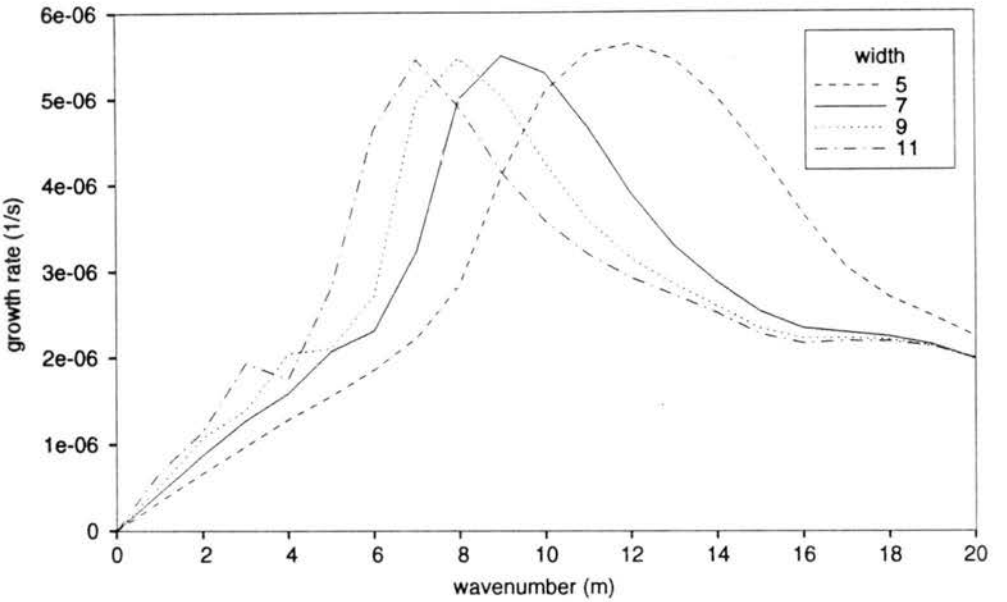

Figure 3.4: Growth rate spectra for vorticity strips of different widths centered at $10°N$ with $\zeta_s = 3.0 \times 10^{-5} s^{-1}$. Strip widths are 5, 7, 9 and 11°.

where the wave-activity, A, and its flux, $\mathbf{F}$, are quadratic (or higher order) functions of disturbance amplitude (α), and the source term, S, contains diabatic and frictional effects for the case of nonconservative flows (Edmon *et al.*, 1980; Andrews, 1987). The definition of A is not unique and is established in order to produce a conservative quantity of squared wave amplitude.

The relevance of the above relation in fluid dynamics is now briefly discussed. The most tangible benefit that can be obtained from (3.31) is that the term $\nabla \cdot \mathbf{F}$ gives a quantitative measure of the effect of the eddies on the mean flow. Wave-activity conservation relations are most easily obtained for linear flows (see, for instance, Edmon *et al.*, 1980; Andrews and McIntyre, 1976), but have also been derived for nonlinear flows (Andrews and McIntyre, 1978) with the requirement of resorting to a generalized Lagrangian mean formulation that presents enormous obstacles to quantitative calculations. Unfortunately, the nonlinear wave-activity relation derived in this section does not possess this attractive property of representing the forcing of the mean flow by the eddies. The wave-activity concept is also useful in the quest for flow stability theorems. Namely, Arnol'd's stability

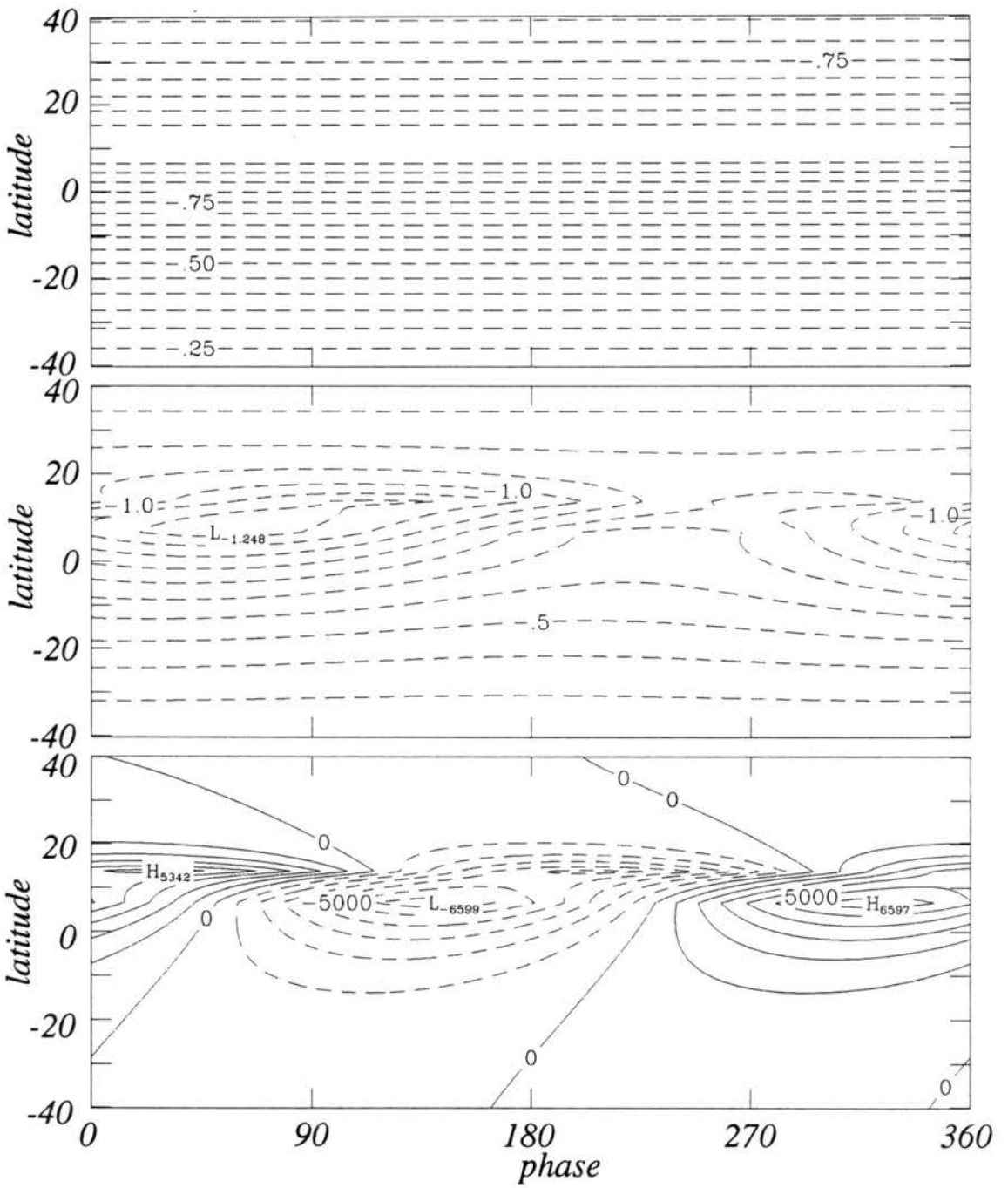

Figure 3.5: Streamfunctions showing the time evolution of the most unstable mode for $\phi_c = 10°$ and $\alpha = 7°$. Fields are at 0, 8 and 16 e-folding times.

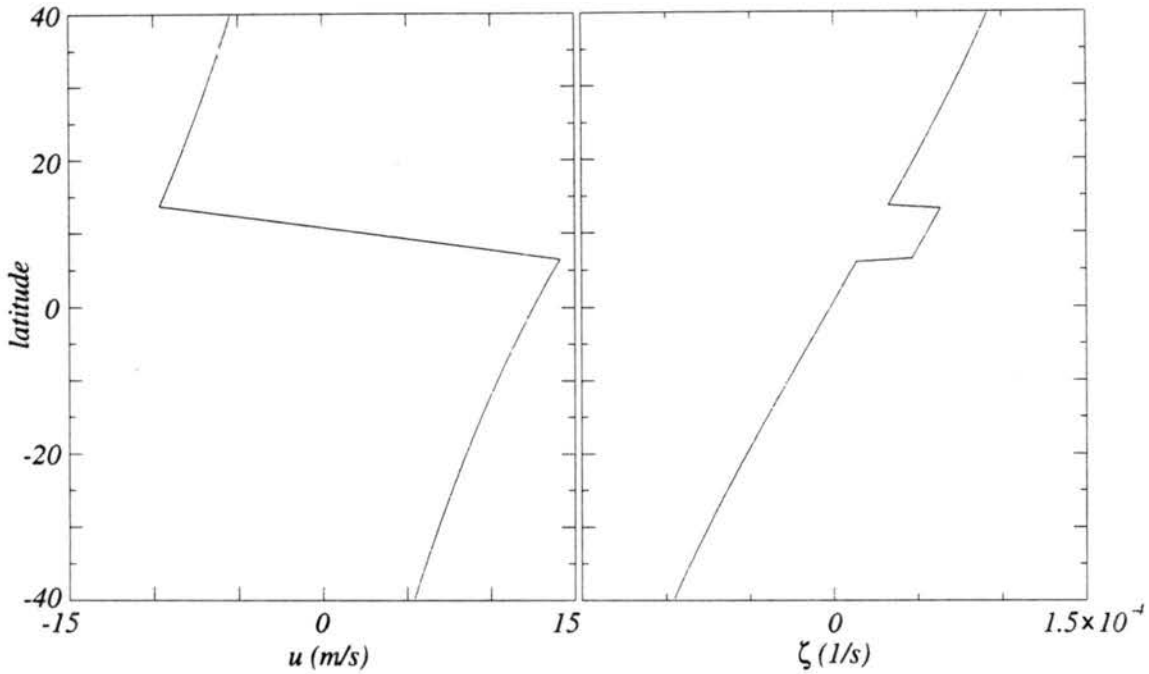

Figure 3.6: Meridional wind and vorticity profiles for a vorticity strip centered at $\phi_c = 10°$ and with width $\alpha = 7°$.

method consists of finding an exact disturbance invariant (*i. e.* the wave-activity) and bounding it between two norms (Shepherd, 1990).

Here, the approach presented in Haynes (1988) is followed in the derivation of two different finite-amplitude wave-activity conservation relations for diabatic, frictionless shallow water flows on the sphere. The first relation is derived for steady, zonally symmetric flows, based on the principle of angular momemtum conservation, the so-called disturbance pseudo-momentum.

3.3.1 Disturbance Pseudo-Momemtum

Using the continuity equation (2.3), it is possible to write the PV and momentum equations (2.14 and 2.19, respectively) in their flux forms:

$$\frac{\partial(q\Phi)}{\partial t} + \frac{\partial(uq\Phi)}{a\cos\phi\partial\lambda} + \frac{\partial(v\cos\phi q\Phi)}{a\cos\phi\partial\phi} = 0 \tag{3.32}$$

$$\frac{\partial(M\Phi)}{\partial t} + \frac{\partial(uM\Phi + \frac{\Phi^2}{2}a\cos\phi)}{a\cos\phi\partial\lambda} + \frac{\partial(v\cos\phi M\Phi)}{a\cos\phi\partial\phi} = MQ \tag{3.33}$$

At this point an arbitrary function $C(q,t)$ (a so called Casimir), which is monotonic in q, is introduced. Multiplying (3.32) by $C_q(q)$ (where $C_q(q) = \frac{\partial C}{\partial q}(q)$) and using the continuity equation, results in the following prognostic equation for $C(q,t)$ in flux form

$$\frac{\partial(C\Phi)}{\partial t} + \frac{\partial(uC\Phi)}{a\cos\phi\partial\lambda} + \frac{\partial(v\cos\phi C\Phi)}{a\cos\phi\partial\phi} = [C - qC_q(q)]\,Q \tag{3.34}$$

Adding (3.33) and (3.35), gives

$$\frac{\partial[(C+M)\Phi]}{\partial t} + \frac{\partial\left[u\Phi(C+M) + \frac{\Phi^2}{2}a\cos\phi\right]}{a\cos\phi\partial\lambda} + \frac{\partial[v\cos\phi\Phi(C+M)]}{a\cos\phi\partial\phi} = [M + C - qC_q(q)]\,Q \tag{3.35}$$

The total flow is now decomposed into $u(\lambda,\phi,t) = \overline{u}(\phi) + u'(\lambda,\phi,t)$, $v(\lambda,\phi,t) = v'(\lambda,\phi,t)$, $\Phi(\lambda,\phi,t) = \overline{\Phi}(\phi) + \Phi'(\lambda,\phi,t)$, where the bars indicate basic state variables and the primes denote disturbances or eddies. No linearization is done which implies that the perturbations are of finite amplitude. Note that the basic state geopotential depth and zonal wind are in balance. Also, this basic state is a steady, zonally symmetric solution of the original equations.

Following Haynes (1988), the next step is to choose a $C(q)$ such that the disturbance part of $\Phi(M+C)$ can be written as a divergence, plus a term which is explicitly second order in wave amplitude. The disturbance part of $\Phi(M+C)$ is defined as

$$\{\Phi\,[M + C(q)]\}' = \Phi\,[M + C(q)] - \overline{\Phi}\left[\overline{M} + C(\overline{q})\right] \tag{3.36}$$

After some manipulation and using $C(q) = C(\overline{q}) + q'C_q(\overline{q}) + O(\alpha^2)$ and $q'\Phi = \zeta' - \overline{q}\Phi'$, (3.36) may be written as:

$$\begin{aligned}[\Phi(M+C)]' \;=\; & \Phi\,[C - C(\overline{q}) - q'C_q(\overline{q})] + \Phi'M' + \\ & + \frac{\partial\,[v'C_q(\overline{q})]}{a\cos\phi\partial\lambda} - \frac{\partial\,[M'C_q(\overline{q})]}{a^2\cos\phi\partial\phi} + \\ & + M'\left[\overline{\Phi} + \frac{\partial C_q(\overline{q})}{a^2\cos\phi\partial\phi}\right] + \Phi'\left[\overline{M} + C(\overline{q}) - \overline{q}C_q(\overline{q})\right]\end{aligned} \tag{3.37}$$

The first line on the right hand side of (3.37) is second order in the disturbance amplitude and will turn out to be the wave-activity. The second line is the divergence of a flux. Next, $C(q)$ will be chosen in such a way that the last line in (3.37) vanishes. The choice

$$C(q) = -\int_0^q m(\tilde{q})d\tilde{q}, \tag{3.38}$$

where

$$m(\overline{q}(\phi)) = \int_0^{\phi} \overline{\Phi}(\tilde{\phi}) a \cos\tilde{\phi} d\tilde{\phi} = -C_q(\overline{q}), \tag{3.39}$$

and $m(\overline{q}(0)) = 0$, makes the last term in the square brackets in (3.37) vanish, as is next verified. Since

$$-\frac{\partial}{a\cos\phi\partial\phi}\left[\overline{M} + C(\overline{q}) - \overline{q}C_q(\overline{q})\right] = \overline{q}\left[\overline{\Phi} + \frac{\partial C_q(\overline{q})}{a\cos\phi\partial\phi}\right], \tag{3.40}$$

and since the right hand side of (3.40) vanishes according to (3.38) and (3.39). Then, $\overline{M} + C(\overline{q}) - \overline{q}C_q(\overline{q}) =$ constant. This constant is zero because the left hand side vanishes at $\phi = \pi/2$. Thus, the entire third line in (3.37) vanishes allowing it to be written as

$$[\Phi(M + C)]' = A + \frac{\partial\left[v' C_q(\overline{q})\right]}{a\cos\phi\partial\lambda} - \frac{\partial\left[M' C_q(\overline{q})\right]}{a^2\cos\phi\partial\phi} \tag{3.41}$$

where the wave-activity, A, is given by

$$A = \Phi\left[C - C(\overline{q}) - q' C_q(\overline{q})\right] + \Phi' M' \tag{3.42}$$

This particular definition of wave-activity is also referred to as a disturbance pseudomomentum, since its derivation is based on M.

The disturbance momentum equations are

$$\frac{\partial u'}{\partial t} - \frac{\partial}{a\cos\phi\partial\lambda}\left(\frac{u'^2 + v'^2}{2} + \overline{u}u' + \Phi'\right) - v' q\Phi = 0 \tag{3.43}$$

$$\frac{\partial v'}{\partial t} + \frac{\partial}{a\partial\phi}\left(\frac{u'^2 + v'^2}{2} + \overline{u}u' + \Phi'\right) + u' q\Phi + \overline{u}\zeta' = 0 \tag{3.44}$$

Finally, substituting (3.41) into (3.37), multiplying the result by $a\cos\phi$ and adding it to $\partial/\partial\phi[C_q(\overline{q})\cos\phi\times$ (3.43)] $-\partial/\partial\lambda[C_q(\overline{q})\times$ (3.44)], gives the following prognostic equation for wave-activity

$$\frac{\partial A}{\partial t} + \frac{\partial\left[uA + \frac{\Phi'^2}{2} a\cos\phi + \frac{\overline{\Phi}}{2}\left(u'^2 - v'^2\right) a\cos\phi\right]}{a\cos\phi\partial\lambda} + \frac{\partial\left[v'\cos\phi A + a v' u'\cos^2\phi\overline{\Phi}\right]}{a\cos\phi\partial\phi} = Q\left(\frac{A + \overline{\Phi}M'}{\Phi}\right) \tag{3.45}$$

with the wave-activity (3.42) rewritten as

$$A = \Phi' u' a\cos\phi + \Phi\int_{\overline{q}}^{q}\left[m(\tilde{q}) - m(\overline{q})\right] d\tilde{q}, \tag{3.46}$$

In the absence of mass sources or sinks and friction, (3.45) expresses conservation of wave-activity when integrated over the sphere. Equation (3.45) is a nonlinear shallow water vesion of (3.31) for steady, zonally symmetric basic flow. However, the divergence term on its left hand side has no counterpart in the equation that governs the basic state, and consequently, says nothing about wave-mean flow interactions.

Relations (3.45)- (3.46) allow diagnostic analysis of the shallow water model results in terms of wave-activity and its flux by following these steps: 1) partition the solution into a steady, zonally symmetric basic state whose potential vorticity varies monotonically with latitude, plus disturbances therefrom; 2) use (3.39) and (3.46) to compute A; and 3) use (3.45) to compute the flux and forcing terms. Application of these wave-activity relations is left for future work.

Chapter 4

ITCZ BREAKDOWN

In this chapter, the formation of tropical disturbances through the ITCZ breakdown process is studied. Although the ITCZ breakdown is believed to occur due to combined baroclinic and barotropic instabilities of the zonal flow (Hack *et al.* 1989; Schubert *et al.*, 1991 and 1992; Guinn, 1992), only the latter can be studied in a shallow water model such as the one used here.

In the low levels, ITCZ convection produces a positive PV anomaly in the NH. This results in a reversed meridional PV gradient on the poleward side of the ITCZ. According to the Charney-Stern theorem (Eliassen, 1983), a flow that has a reversal in the poleward gradient of PV may be unstable with respect to small disturbances. The ITCZ then starts undulating under the influence of combined barotropic and baroclinic instability and breaks down into a series of tropical disturbances. In this sense, the ITCZ convection produces favorable conditions for its own instability and breakdown.

Guinn (1992) used a doubly periodic shallow water model on an f-plane to show that strips of high (low) vorticity in the Northern (Southern) Hemisphere undulate and break down into vortices in a way that resembles the ITCZ breakdown observed in satellite images. He then associated the thin strips of high vorticity that link these vortices to the outer bands of hurricanes.

In this model, either initially imposed PV anomalies or mass sinks are used as proxies of the ITCZ. The PV anomaly then undulates and breaks down due to barotropic instability of the mean flow in a way that resembles what is observed in satellite images such as the sequence shown in Fig. (1.3). This should not imply that barotropic instability is the sole process involved in the ITCZ breakdown, but it tries to isolate what may be an important aspect of its dynamics.

In section 4.1, initial value experiments showing the nonlinear breakdown of vorticity strips on the sphere are presented. The interaction of a zonally symmetric vorticity strip and a nearby vortex is then studied in initial value experiments discussed in section 4.2. In section 4.3, perhaps more realistic experiments with localized zonally elongated mass sinks are performed. In section 4.4, results obtained when the mass sink is wider on its eastern side are presented. Finally, section 4.5 presents an analysis of the frequency of tropical cyclone formation in the Eastern Pacific Ocean in the past 14 years.

4.1 Zonally Symmetric Vorticity Strips

In this section, the nonlinear breakdown of zonally symmetric vorticity strips on the sphere is simulated in a series of initial value experiments. These vorticity strips may be interpreted as a highly idealized zonally symmetric ITCZ which breaks down into a number of tropical cyclones.

The initial absolute vorticity field is simply given by

$$\zeta(\lambda,\phi,0) = \begin{cases} \zeta_s + f & \text{for } |\phi - \phi_c| \leq b/2 \\ f & \text{otherwise} \end{cases} \tag{4.1}$$

where ζ_s, ϕ_c and b are the magnitude of the vorticity strip, the latitude where it is centered and its width, respectively. Note that this initial vorticity profile satisfies Rayleigh's necessary, but not sufficient, criterion for barotropic instability (see section 3.1). A sinusoidal perturbation of zonal wavenumber m and amplitude of $10^{-7}\,s^{-1}$ was added to the vorticity strip. This is done to provide the fluid with a finite initial disturbance which will grow by extracting energy from the mean flow through the barotropic instability process.

Given the above vorticity field, the corresponding initial wind and geopotential fields are obtained from (4.1) and (2.22) as explained in section 2.4. The mean geopotential depth, $\overline{\Phi}$, was set to $4500\,m^2/s^2$ in this case which implies in a Rossby radius of $\sim 1800\,km$ at $15°N$.

Figure 4.1 shows meridional cross sections of the wind and vorticity fields for a 7° wide zonal vorticity strip centered at $15°N$ with maximum intensity $\zeta_s = 3.0 \times 10^{-5}\,s^{-1}$ (or about $0.8\,f$). This vorticity strip has a meridional wind shear of about $21\,m/s$ across

its 7° of width (see figure 4.1 for the initial meridional profiles of absolute vorticity and zonal wind for this strip). Although time averages of zonal winds in the region do not show such large meridional shears (see, for example, Tai and Ogura, 1987), it is possible that high shear exists on individual days. Also, as seen in figure 3.3, weaker shear profiles

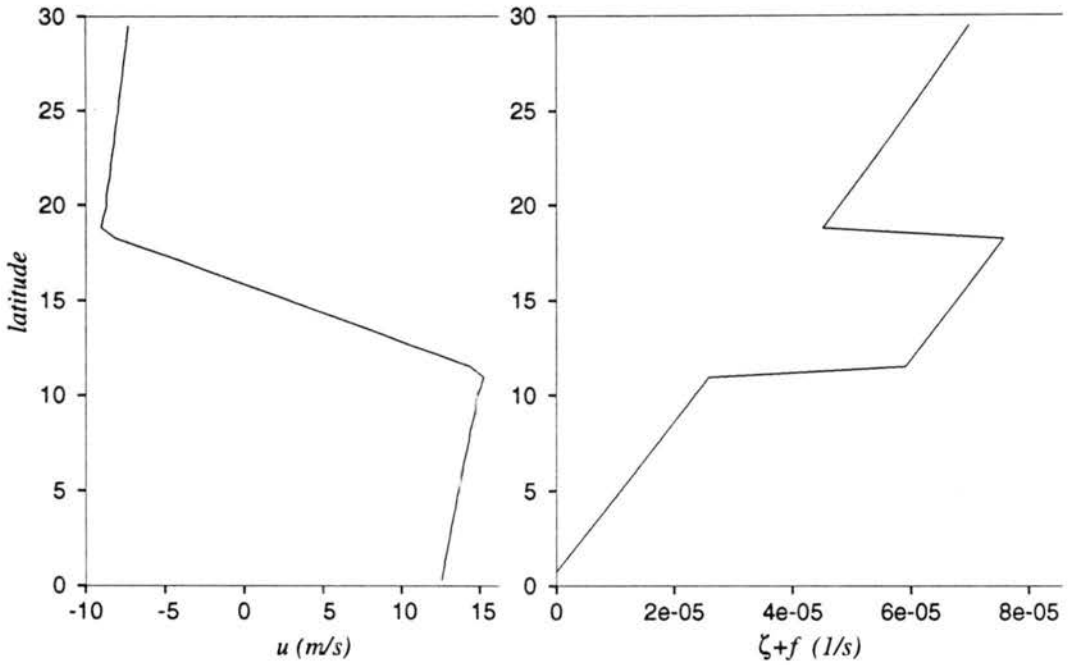

Figure 4.1: Initial zonal wind and absolute vorticity profiles across a 7° wide zonally symmetric vorticity strip centered at $15°N$ with maximum intensity $\zeta_s = 3.0 \times 10^{-5}\, s^{-1}$.

will break down as well, but with slower growth rates. A wavenumber ten perturbation is imposed to the initial fields. Wavenumber 10 is chosen because it is one of the most unstable modes selected for the same vorticity strip in the linear normal mode stability analysis (see figure 3.3). Moreover, when this simulation was repeated with a white noise initial perturbation (not shown), an unstable disturbance of wavenumber 10 emerged.

The temporal evolution of this PV strip in the shallow water model is shown in figure 4.2. Initially, the geopotential, wind and PV fields are basically zonally symmetric, with small departures from symmetry introduced by the wavenumber 10 perturbation. Five days into the simulation, the PV field is undulating due to the growth of the initial imposed perturbation through barotropic instability. After 11 days, the PV strip has broken down into ten vortices (of which only three are shown in Fig. 4.2) that are linked

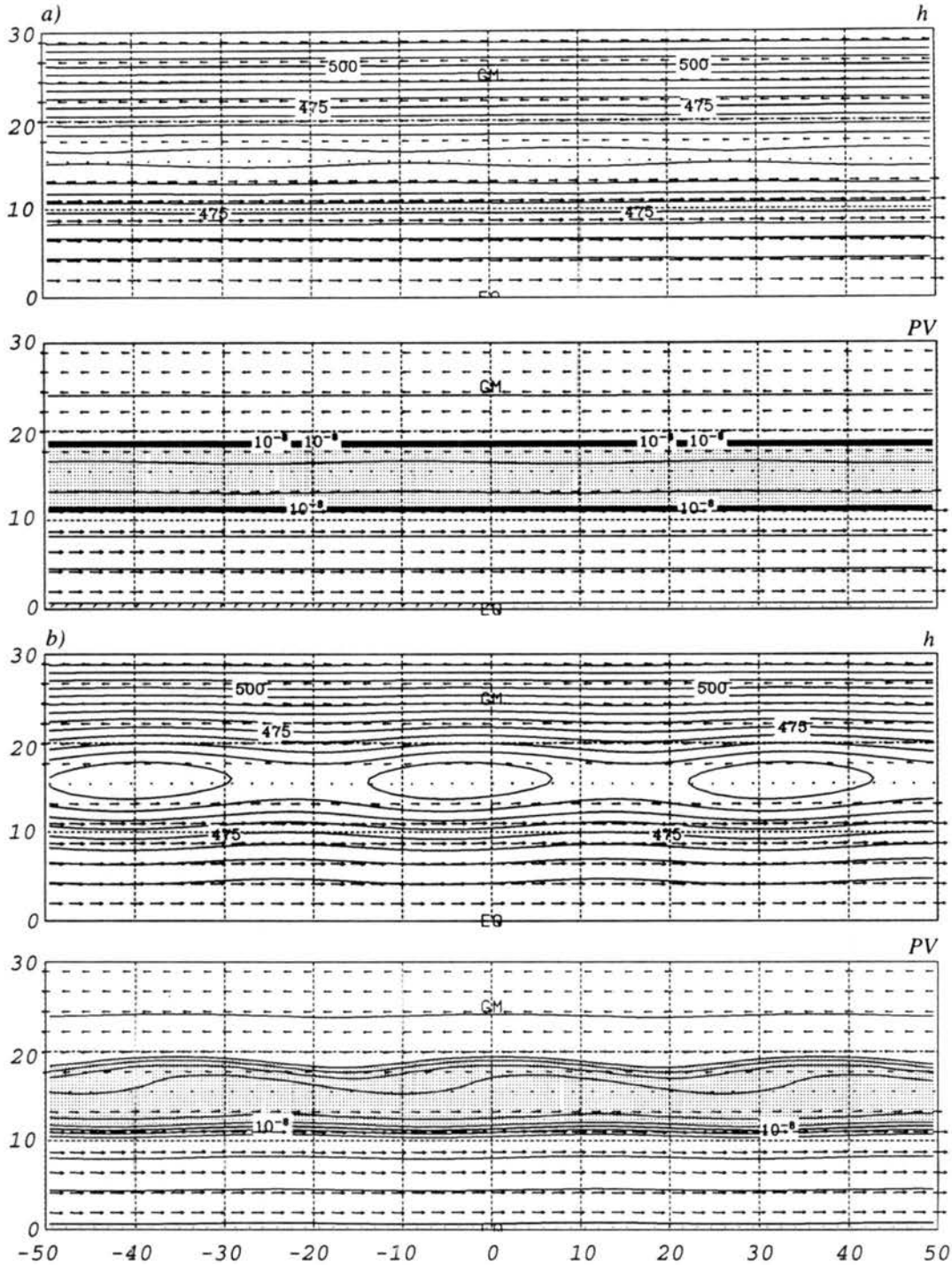

Figure 4.2: Breakdown of a 7° wide zonally symmetric vorticity strip centered at 15°N with maximum intensity $\zeta_s = 3.0 \times 10^{-5}\, s^{-1}$; *a)* initial height (in m), PV (in $s\,m^{-2}$, with contours from 0. to 1.6×10^{-8} by 0.2×10^{-8}) and wind fields (in m/s); *b)* same fields at 5 days. In the PV plot, values greater than $1.4 \times 10^{-8} s\,m^{-2}$ are dotted. Maximum wind vectors are 20 m/s and span the distance between two plotted grid points.

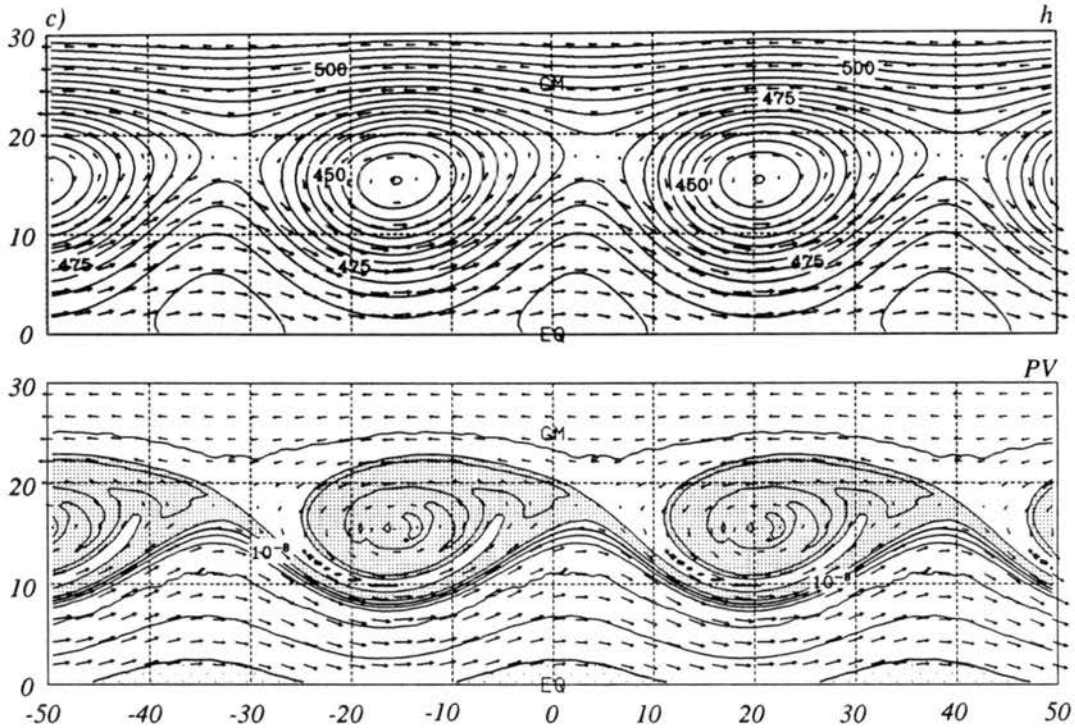

Figure 4.2: Continued. *c)* Same at 11 days.

by thin PV filaments. These PV filaments are what Guinn and Schubert (1993) call the outer spiral bands of hurricanes. The horizontal scale of the resulting instabilities is approximately 3800 km with westward propagation of $\sim 2\,m/s$, very close to the 2.3 m/s westward propagation predicted by the linear normal mode stability calculation for the same mode (see figure 3.1*c*). It is relevant to mention that the significance of the time frame in which breakdown occurred in this experiment is limited because breakdown is expedited by imposition of a larger initial perturbation. The fact that a larger amplitude initial disturbance causes break down in less model time offers support to the idea that if easterly waves indeed propagate from the Atlantic into the East Pacific (Simpson *et al.*, 1969; Frank, 1976; Frank, 1987; Avila and Clark, 1989) they may trigger a faster breakdown of the ITCZ and perhaps allow tropical cyclone genesis to occur in the latter region.

When the PV strip starts breaking down, the resulting vortices are elongated in the zonal direction. As time proceeds, azimuthal symmetrization of each individual vortex

is observed. This axisymmetrization is related to the stripping of vorticity by the thin filaments that link the vortices (Melander *et al.*, 1985; Guinn, 1992).

It is interesting to note that to the southwest (southeast) of each of these vortices, there is intrusion of negative (positive) PV air from the Southern (Northern) into the Northern (Southern) Hemisphere. In these regions, the necessary condition for occurrence of inertial instability, that is $f\overline{q} < 0$, is met. However, inertially unstable modes have very slow growth rates for flows with a large $\overline{\Phi}$ (Schubert *et al.*, 1992) and therefore are not apparent in the simulations shown here.

Additional experiments were run (not shown here) to see the effect of width and intensity changes upon the breakdown of the PV strip. In agreement with the linear normal mode stability analisis results, wider (narrower) PV strips broke down into larger (smaller) vortices and an increase (decrease) in shear resulted in faster (slower) breakdown.

4.2 Interaction Between a Vortex and a Zonally Symmetric PV Strip

In this section, experiments aimed at investigating the interaction of the ITCZ with a nearby tropical cyclone are performed. These are initial value experiments in which a vortex is placed near the zonally symmetric PV strip used in the previous section.

An interesting example of this interaction occurred in the E. Pacific basin in July, 1978 and is portrayed in Fig. 4.3. Hurricane Fico began as a tropical depression in the ITCZ at $10.8°N$, $105.9°W$ on July 9. It was upgraded to a hurricane on July 10 near $13.6°N$,$111.4°W$. Hurricane Fico then followed a long trajectory due west at an average speed of about 5.3 m/s until July 21 when it recurved and moved into higher latitudes (Gunther, 1979). On July 17, the hurricane was detached from the ITCZ which lied about 5° to its south. By July 18, the circulation of the hurricane had produced a perturbation on the ITCZ that accompanied the storm in its westward movement until it recurved on July 21. As the hurricane moved into higher latitudes, its influence on the ITCZ decreased and so did the amplitude of the perturbation in the ITCZ. Hurricane Gilma followed Fico in that season and similarly perturbed the ITCZ, though it had a more northward track and ceased to influence the ITCZ in a shorter period of time.

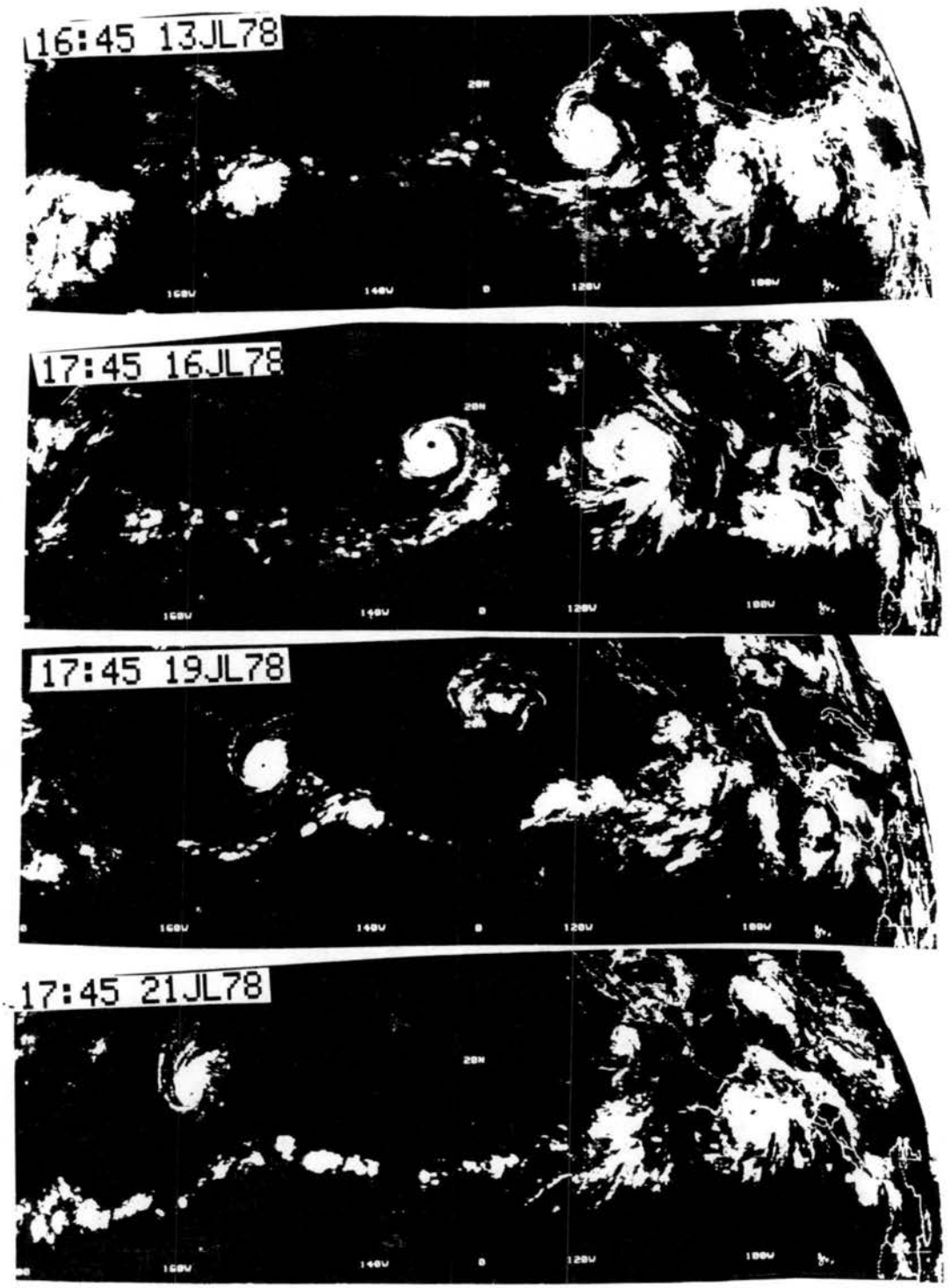

Figure 4.3: GOES infrared satellite images for the E. Pacific during the period between 13 and 21 July 1978 (time is UTC). The sequence illustrates the interaction of Hurricane Fico with the ITCZ.

A highly idealized barotropic counterpart of that process is obtained if the model is initialized with a zonally symmetric PV strip with a circular cyclonic vortex nearby. The circular vortex is initialized by

$$\zeta(\lambda,\phi,0) = \begin{cases} \zeta_v & \text{for } \left|\sqrt{\left(\frac{1+sm-b_1\sin\phi}{b_2}\right)^2 + \sin^2\phi(1+\cos^2\phi)}\right| \leq 1 \\ 0 & \text{otherwise} \end{cases} \tag{4.2}$$

where

$$sm = \frac{b_1^2\cos\gamma}{\sqrt{b_1^2+b_2^2}}\left(1+\frac{b_1^2}{b_2^2}\right) - 1,$$

γ is the length of the arc comprised by the radius of the vortex, and the latitude where the vortex is centered is $\phi_{cv} = \arctan(b_1/b_2)$. Equation (4.2) is obtained by calculating the intersection of a plane with the surface of the sphere and imposing a step function radial variation. The zonally symmetric vorticity strip is again given by equation (4.1).

The radial distributions of relative vorticity and non-divergent tangential wind for a vortex centered at 15° N with $\zeta_v = 2 \times 10^{-4}\, s^{-1}$ and 2° in radius are shown in figure 4.4. The outer core wind distribution in figure 4.4 falls within the observed range of outer core tangential winds of tropical cyclones (Merrill, 1984). A higher spatial resolution would be needed to obtain a good representation of the inner core winds. However, it may be the case that the interaction of the idealized vortex with the PV strip is more dependent on the outer core winds than on the intensity of the storm, just as it is the case for tropical cyclone motion (Chan and Williams, 1987).

The interaction of the vortex described above with a 7° wide zonally symmetric PV strip centered at 10°N with $\zeta_s = 2. \times 10^{-5}\, s^{-1}$ is shown in Fig. 4.5. In order to allow a reasonable initially balanced state, it was necessary to set $\overline{\Phi} = 4.5 \times 10^4\, m^2 s^{-2}$, which gives a Rossby radius of about $5600\, km$ at 15°N. The initial wind, height and PV fields are shown in figure 4.5*a*. Added to the westerly flow to the south of the PV strip and easterly flow to its north, are the strong meridional and zonal winds introduced by the vortex. Note also that just to the north of the PV strip, the necessary criterion for barotropic instability is met. By day two (fig. 4.5*b*), the vortex is wrapping the PV strip around itself, producing sharp perturbations on the PV strip directly to its SE and SW.

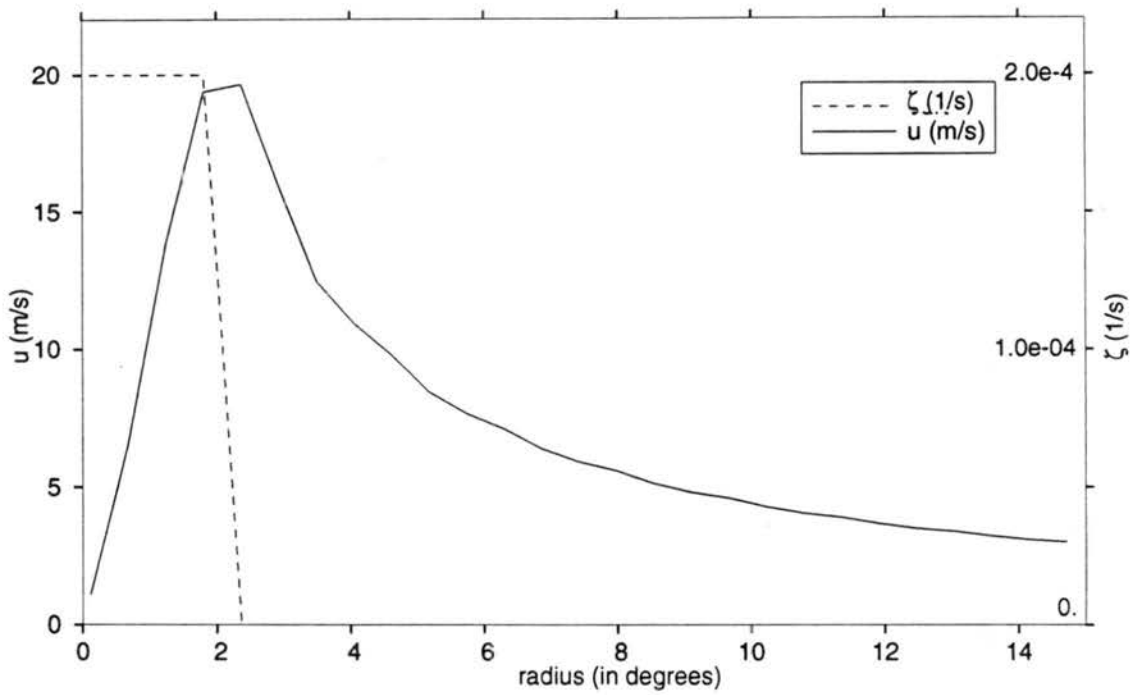

Figure 4.4: Radial relative vorticity and wind distributions of the vortex used in the simulation of the interactions between a zonally symmetric PV strip and a nearby vortex.

The perturbation on the SW side is constrained to the region near the vortex. On the southeastern side, however, eastward propagation of short Rossby wave energy causes the PV strip to undulate with an amplitude that decreases with increasing distance from the vortex. As time proceeds, these undulations will amplify through barotropic instability, causing the PV strip to break down into a series of vortices (fig. 4.5*d*). Throughout the simulation, the vortex continuously moves towards W-NW at an average speed of $\sim 9.1\, m/s$. The initial perturbation on the PV strip just to the SE of the vortex follows the westward movement of the vortex at a somewhat slower speed. By the end of the simulation, the vortex has increased in size and its influence on the PV strip is decreasing. This bears resemblance with the effect of Hurricane Fico on the ITCZ in the satellite image sequence shown in figure 4.3.

Regarding the breakdown of the part of the PV strip that lies to the east of the vortex, additional experiments (omitted here) showed that the closer the vortex is to the strip, the larger the perturbation it causes, implying in faster breakdown.

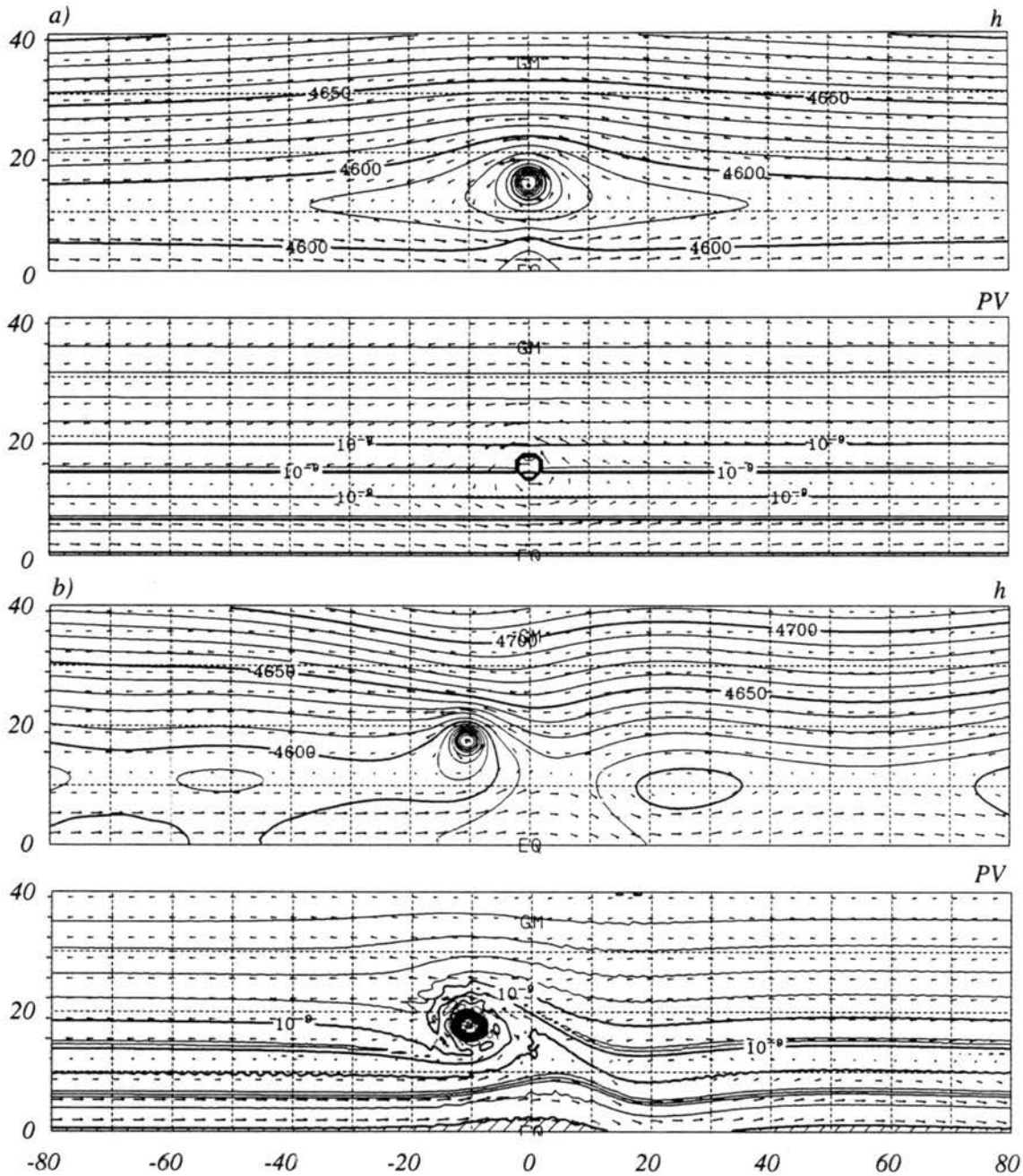

Figure 4.5: Interaction of a vortex centered at $15°N$ with $\zeta_v = 2 \times 10^{-4}\, s^{-1}$ and $2°$ in radius with a $7°$ wide zonally symmetric PV strip centered at $10°N$ with $\zeta_s = 3 \times 10^{-5}\, s^{-1}$. Height (m), wind (m/s) and PV ($s\, m^{-2}$) fields at *a)* initial fields; *b)* 2 days. PV contours are from 0. to $5.6 \times 10^{-9} s^2/m$ by $0.2 \times 10^{-9} s^2/m$ and maximum wind vector is $20\, m/s$ in modulus and spans the distance between two plotted grid points.

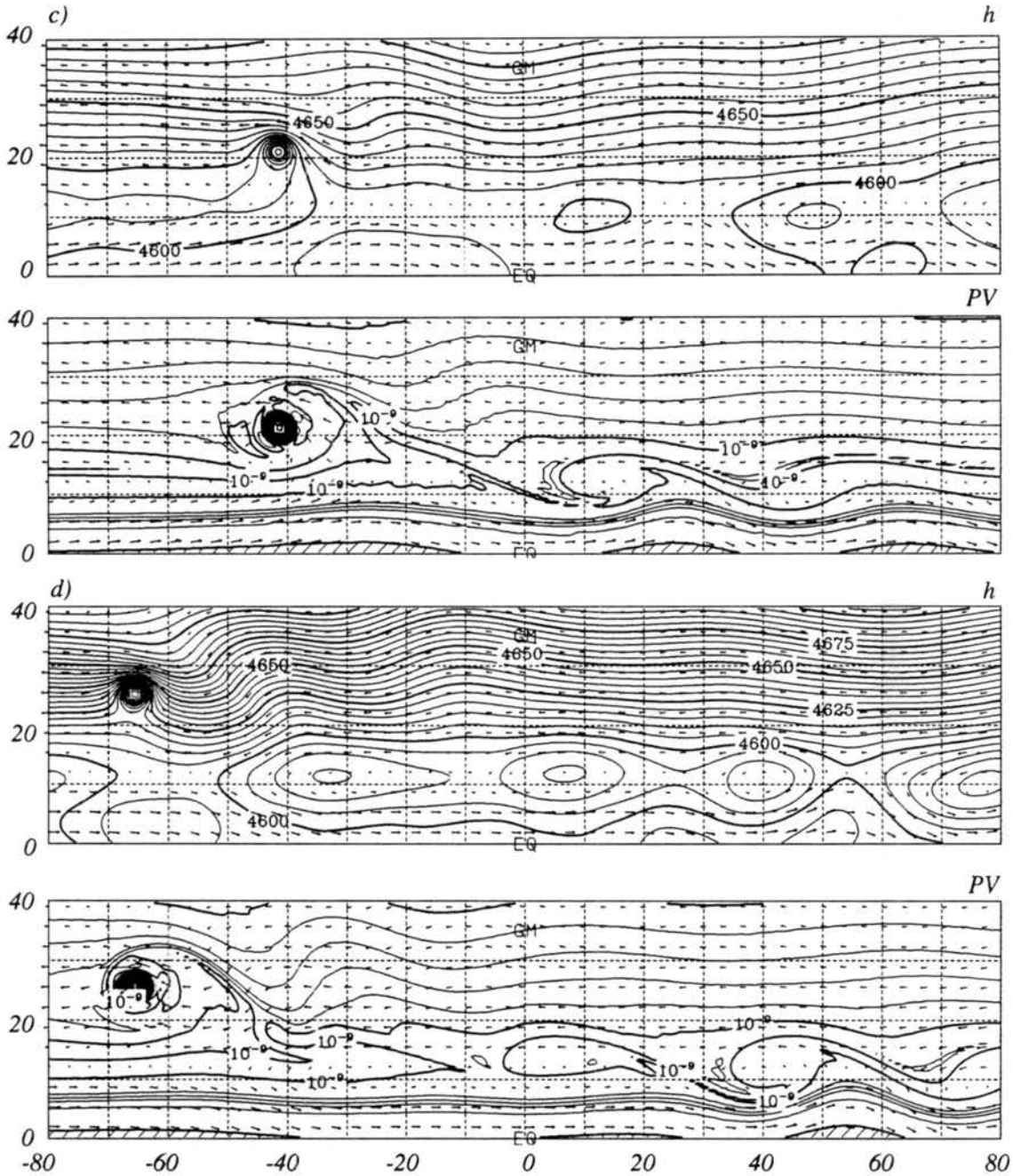

Figure 4.5: Continued. *c)* At 6 days; *d)* at 9 days.

Figure 4.6 shows the effect of the PV strip on the trajectories of vortices initially centered at different latitudes. The track of the same vortex centered at 10°N in a quiescent environment is shown for comparison (VOR). In a resting environment, the vortex follows a northwestward trajectory (in the NH) known as β-drift. This movement is due to linear and nonlinear interactions between the circulation of the vortex and the meridionally varying planetary vorticity (Elsberry, 1987; Chan and Williams, 1987; Li and Wang, 1994; and references therein). The introduction of a zonally symmetric PV strip (NPV) to the south of this vortex adds a steering flow that changes both the speed and direction of the β-drift movement of the vortex, resulting in a faster and more zonal propagation. If the vortex and the PV strip are initially centered at the same latitude (CPV), the vortex initially propagates northward and then westward (CPV). Finally, when vortex is initially centered to the south of the PV strip (SPV), its initial movement is to the NE, turning to northward once it crosses the center of the strip and then to the W-NW as soon as it exits the northernmost boundary of the PV strip. The presence of the PV strip affects the movement of the vortex mainly through advection by its steering flow, but also through the change in background vorticity it introduces (Evans *et al.*, 1991).

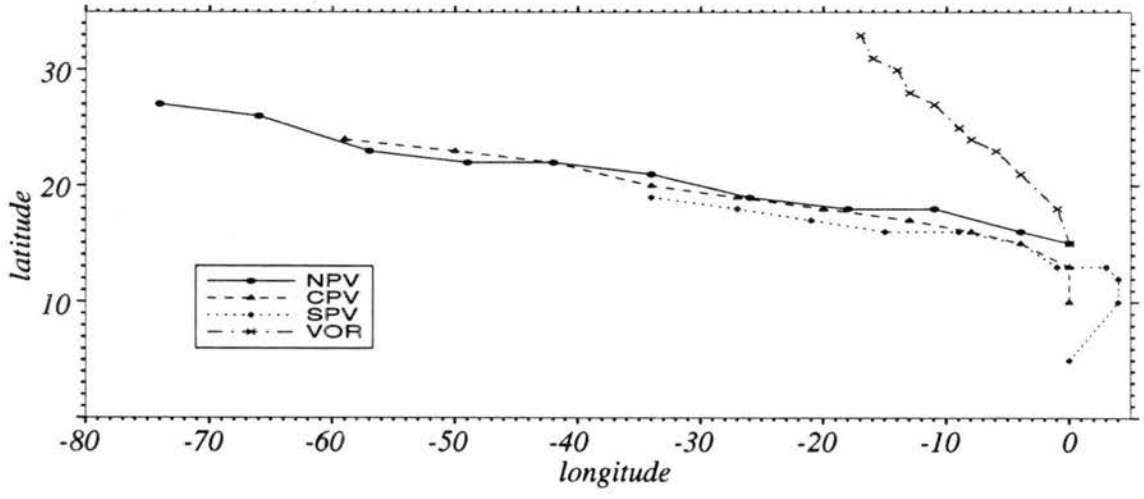

Figure 4.6: Trajectories followed by vortices initially centered at 15° (NPV), 10° (CPV) and 5° (SPV), under the influence of a zonally symmetric PV strip centered at 10°. The trajectory of a vortex centered at 10° in a quiescent environment (VOR) is included for comparison. Symbols denote vortex positions at 24h intervals.

Figure 4.7 shows the height and PV fields at 9 and 15 days for a simulation that started with the vortex depicted in figure 4.4 embedded in a quiescent environment. In

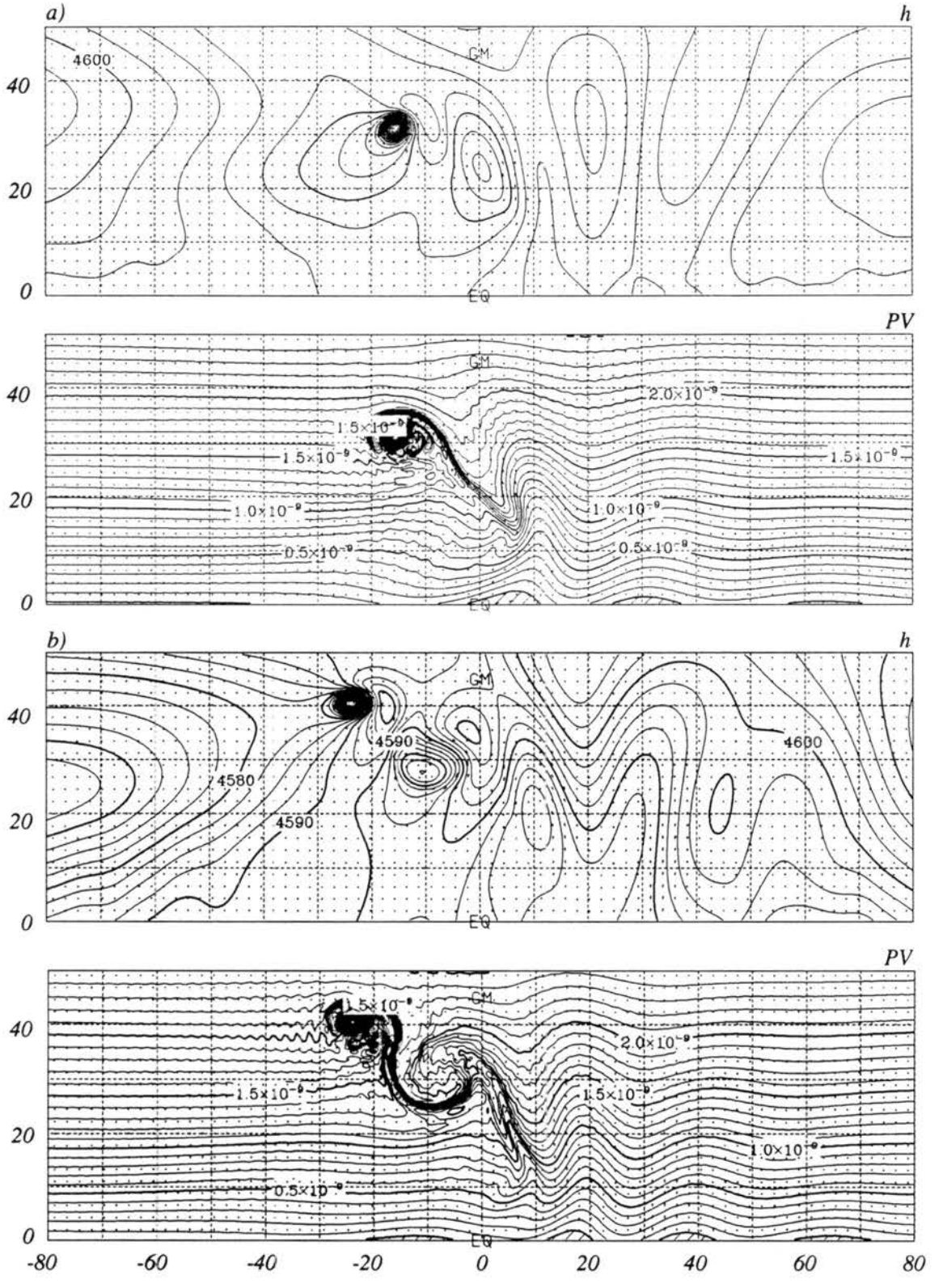

Figure 4.7: Height (m) and PV ($s\,m^{-2}$) fields for a 2° radius vortex with $\zeta_v = 2 \times 10^{-4}\,s^{-1}$ and $\phi_c = 15°N$ in a quiescent environment. *a)* at 9 days; *b)* at 15 days.

the height field it is evident that dispersion of short Rossby waves produces a train of waves to the SE of the vortex (Hoskins *et al.*, 1977). After 15 days, a cyclone has been produced just to the SE of the initial cyclone with half of its intensity. In a 20 year observational study in the W. Pacific, Frank (1982) found that typhoons are twice as likely to form to the east of existing typhoons than to their west. The simulation shown in figure 4.7 suggests that Rossby wave dispersion may be the mechanism that causes the formation of a new cyclone in the wake of an existing typhoon (Holland, 1994). However, the intensity of this secondary cyclone is considerably reduced when a PV strip is located to the south of the vortex as shown in experiment SV (compare figures 4.5 and 4.7 at 9 days). This seeming preference for the formation of new storms to the east of existing ones may also be an artifact of the westward movement of the cyclones away from preferred regions of origin. Another possible mechanism to explain the observed higher frequency of tropical cyclone genesis to the east of existing cyclones is the breakdown of the ITCZ under the influence of a nearby vortex, as suggested in figure 4.5.

4.3 Elliptical Mass Sink

In the previous sections, the ITCZ was idealized as a zonally symmetric PV strip circling the sphere near the equator. However, at any individual time, the ITCZ is a rather discontinuous zonal band of convection of varying widths. For this reason, perhaps a more realistic representation of the transient ITCZ in the model would be in the form of localized elliptical mass sinks near the equator. Results obtained in experiments with one such elliptical mass sink of varied dimensions and different locations are discussed in this section.

The spatial variation of the mass sink, $Q(\lambda, \phi, t)$ is given by

$$F(\lambda,\phi) = \begin{cases} 1 - \exp\left[-\frac{k_s}{r}\exp\left(\frac{1}{r-1}\right)\right], & \text{for } 0 < r < 1 \\ 0, & \text{otherwise} \end{cases} \tag{4.3a}$$

with

$$r(\lambda,\phi) = \sqrt{\frac{(\lambda\cos\phi - \lambda_0\cos\phi_0)^2}{(c\pi/180)^2} + \frac{(\phi-\phi_0)^2}{(\gamma_{dist}\, d\pi/180)^2}}, \tag{4.3b}$$

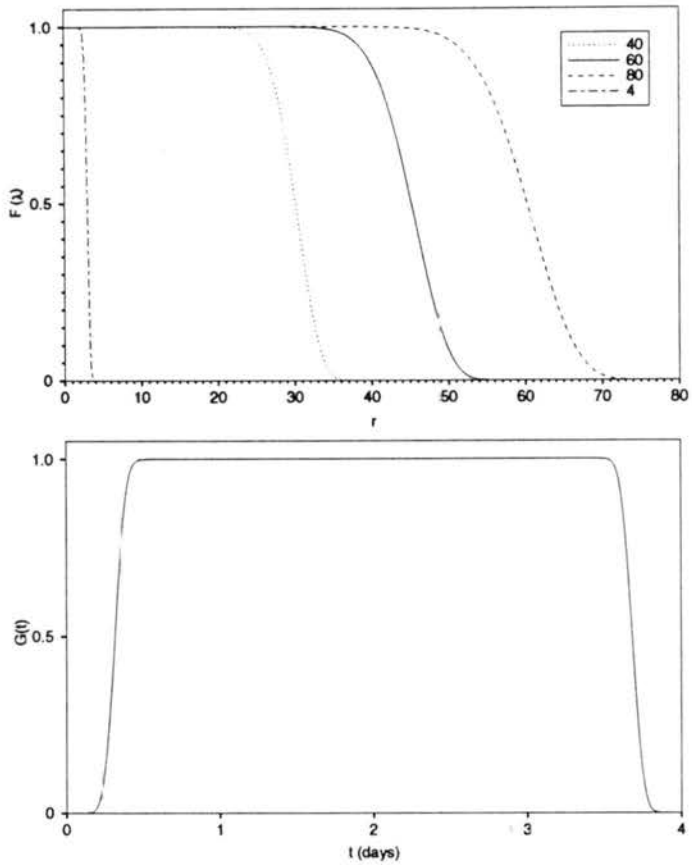

Figure 4.8: Nondimensional radial ($F(\lambda)$) and temporal ($G(t)$) variations of the mass sink as given by equations 4.3 and 4.4. *a)* $F(r)$ for $k_s = 30$ and $c = 4$, 40, 60 and 80 (radius is in degrees from the center of the ellipse); *b)* $G(t)$ for $k_t = 320$, and $\tau = 4$ days.

λ_0 and ϕ_0 are the longitude and latitude where the forcing is centered, γ_{dist} is a parameter used to distort the ellipsoid ($\gamma_{dist} = 1$, in this case), c is the distance between the focus and the center of the ellipse and d is the size of its minor axis (in degrees). Figure 4.8 shows the variation of F with λ (Melander *et al.*, 1985). In equation (4.3), setting $r(\lambda, \phi)$ equal to different constants, defines a family of elliptical curves of aspect ratio $2c/d$.

The time variation of the mass sink has the form

$$G(t) = \begin{cases} 1 - \exp\left[-\frac{k_t}{p}\exp\left(\frac{1}{p-1}\right)\right], & \text{for } 0 < t < \tau \\ 0, & \text{otherwise} \end{cases} \tag{4.5a}$$

where

$$p(t) = \sqrt{\left(\frac{2t}{\tau} - 1\right)^2} \tag{4.5b}$$

and τ is the duration of the forcing (in days). The steepness parameters, k_s and k_t, determine how fast the mass sink decreases with increasing radius, and how fast the mass

sink is turned on and off, respectively. Figure 4.8 shows the nondimensional time variation of the mass sink when $\tau = 4$ days.

Finally, equations (4.3) and (4.4) are combined to define the mass sink function

$$Q(\lambda, \phi, t) = \left| \frac{\partial \Phi}{\partial t} \right| F(\lambda, \phi) G(t) \tag{4.5}$$

where $\mid \partial\Phi/\partial t \mid$ is the time rate of change of geopotential. Table 5 of Fulton and Schubert (1985) shows that the second internal mode calculated for the Marshall Islands apparent heating vertical profile has phase speed of 46.66 m/s, $\Phi = 2177.15\ m^2 s^{-2}$ and $\mid \partial\Phi/\partial t \mid = 541\ m^2 s^{-2} day^{-1}$. The steepness parameters, k_s and k_t, are set to 30 and 320, respectively and will be kept constant hereafter.

The model runs are initialized with a basic state at rest upon which the mass sink in equation (4.5) is imposed. The dimensions of the mass sink were chosen to roughly approximate the dimensions of observed ITCZs in the E. Pacific.

Figure 4.9 shows the temporal evolution of the height, PV and wind fields produced when a zonal elliptical mass sink centered at $10°N$ with dimensions given by $c = 60°$ and $d = 4°$ (see figure 4.8), is applied for 4 days.

A reversal in the PV gradient first appears during day 2 of integration (diagram not shown), providing the necessary condition for the occurrence of barotropic instability. This is in agreement with the conclusion in Hack *et al.* (1989) that only a couple of days of convection are needed to produce a reversal in the meridional PV gradient. Figure 4.9*a* shows the results at 5 days, when the mass sink has already been turned off. The positive PV strip produced by the mass sink has rotated cyclonically around its center due to self-advection. Similar f-plane calculations by Guinn (1992) show a PV strip that rotates almost 60° around its axis by the time it breaks down into two vortices. Here, the presence of a meridionally varying planetary vorticity inhibits this rotation and the PV strip seems to find an equilibrium inclination with respect to the equator. It would be interesting to check if similar patches of ITCZ convection display a preferred tilt in the tropics. By day 10 (figure 4.9*b*), the PV strip is undulating and breakdown has begun on its westernmost portion. After 15 days (fig. 4.9*c*), the PV strip has broken down into

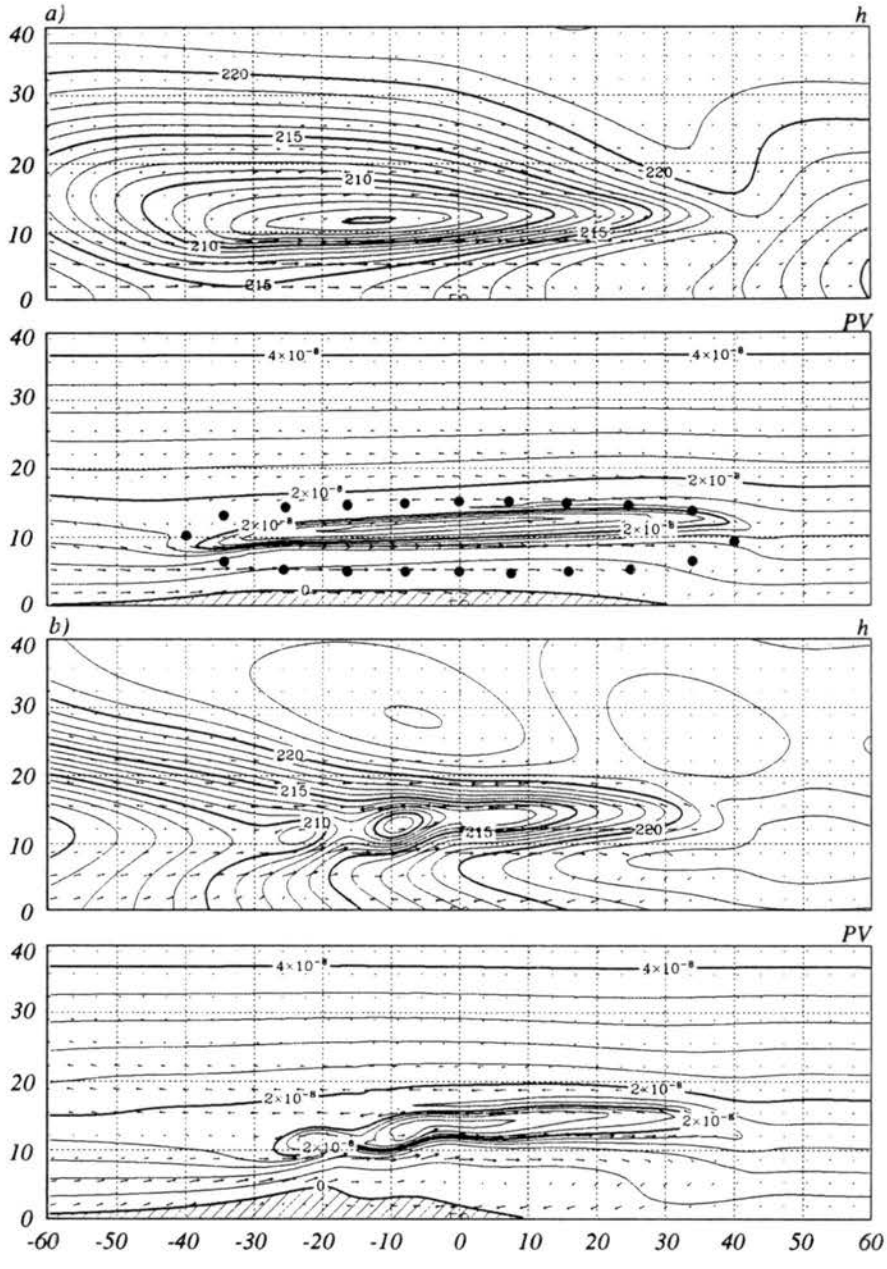

Figure 4.9: Evolution of height (m), PV ($s\,m^{-2}$) and wind (m/s) fields for the case in which a zonally oriented elliptical mass sink centered at $\phi_c = 10°N$, with $c = 60$, $d = 4$ and $\tau = 4$ is imposed. Hatched regions in the PV plot denote regions of negative PV. Heavy dots indicate shape and location of mass sink; *a)* at 5 days; *b)* at 10 days.

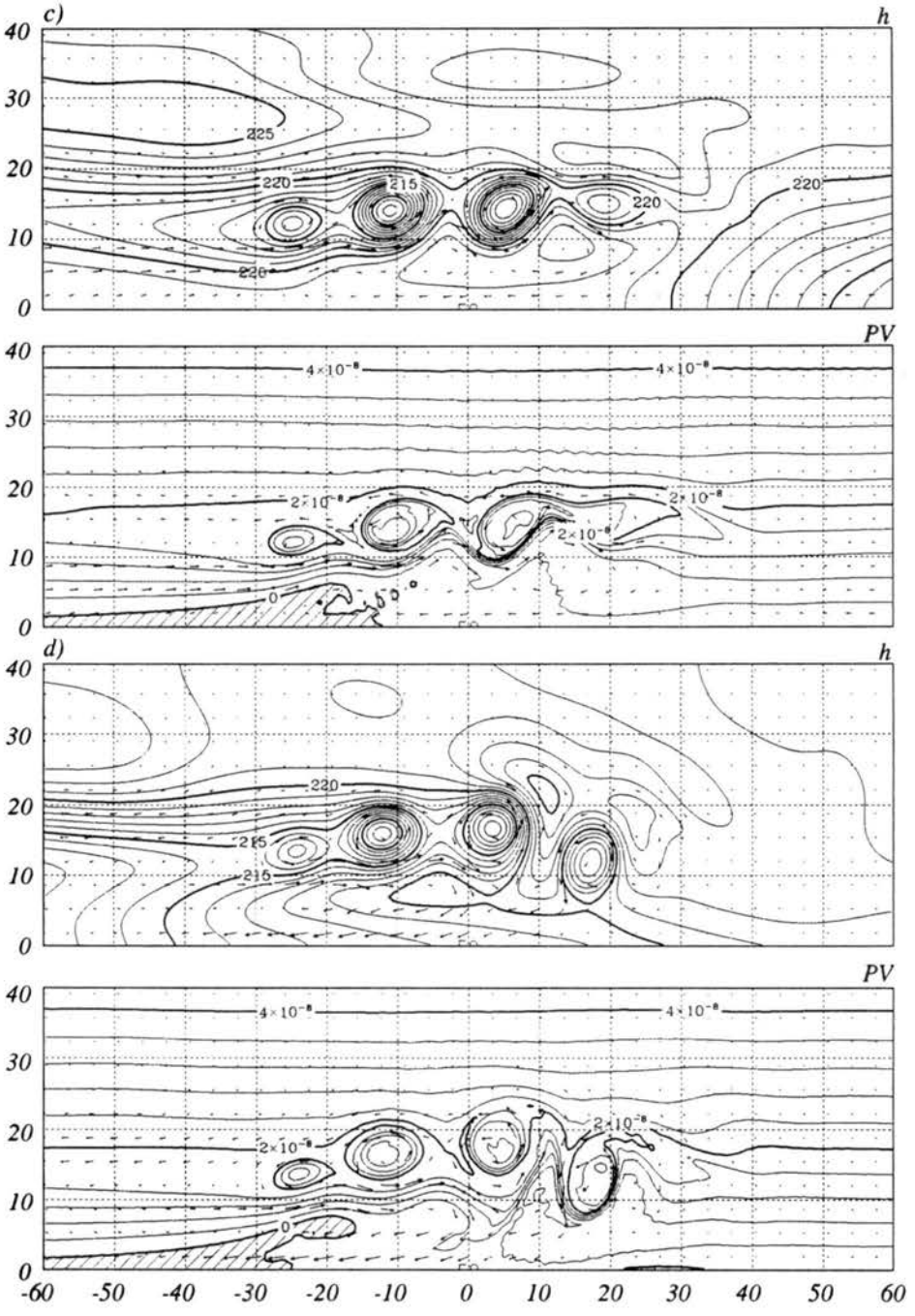

Figure 4.9: Continued. *c)* At 15 days; *d)* at 20 days.

three vortices linked by thin filaments of high PV, and a fourth one is being produced on its easternmost end. After 20 days (fig. 4.9*d*), the PV strip has completely broken down into four distinct vortices whose horizontal scale is about $1000\,km$. Finally, at 25 days (fig. 4.9*e*), the westernmost vortex is being stretched into a strip by its neighbor and will eventually be merged into it. Also, the easternmost vortex is being stretched into a strip by the ambient flow. It is also noteworthy that the vortices that resulted from the breakdown of the strip did not move farther than 10° away from their formation region.

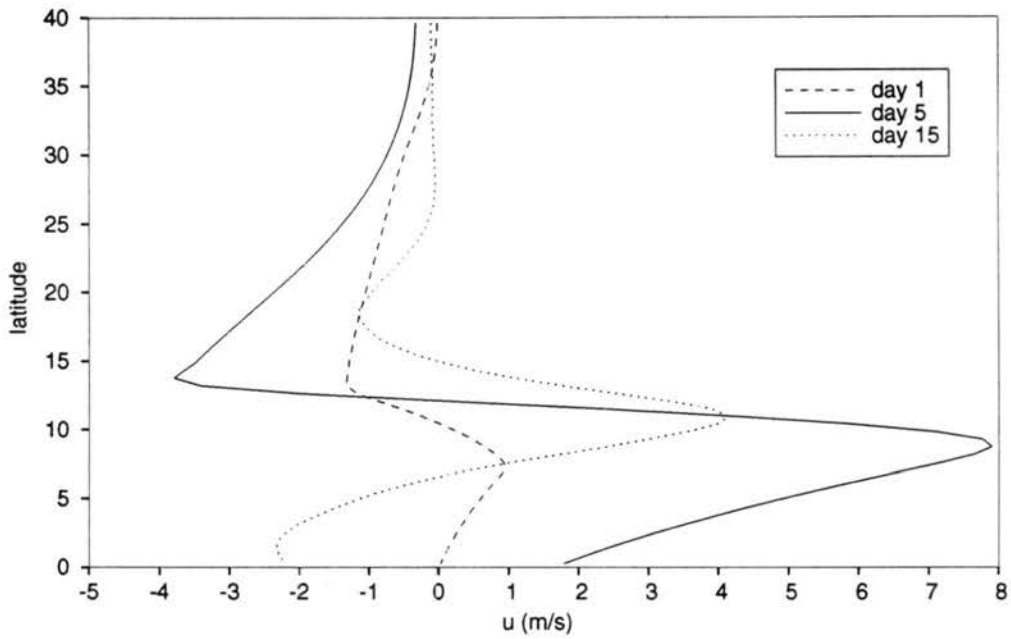

Figure 4.10: Meridional profiles of zonal winds across the center of the PV strip after 1, 5 and 15 days.

Figure 4.10 shows meridional cross sections of the zonal winds through the center of the PV strip on days 1, 5 ond 15 of the simulation. As expected, in the first 4 days of the simulation, the mass sink is producing westerlies to its south and easterlies to its north. This flow structure resembles the tropical monsoon trough circulation pattern. The winds generated by the mass sink attain maximum intensity when the forcing is turned off, weakening thereafter. On day 5, the westerlies to the south of the PV strip are approximately twice as strong as the easterlies to its north. This difference in strength between the easterlies and westerlies is due to weaker inertial stability to the south of

the PV anomaly. This weaker inertial stability region allows stronger meridional winds to the south of the PV anomaly and therefore stronger zonal winds are produced due to the Coriolis effect. As mentioned before, the establishment of the monsoonal flow in the model is due to the presence of the imposed mass sink suggesting that tropical monsoonal circulations are forced by equatorial convection. This is in agreement with observations (Mapes and Houze, 1992; Sui and Lau, 1992; Phoebus, 1993) that indicate that the monsoon flow is forced by the embedded deep convection. After 15 model days, the extent of the monsoonal westerlies is confined to the region just to the south of the PV strip, with easterlies near the equator.

The behaviour of the breakdown at different latitudes is compared by varying ϕ_0 and keeping all other parameters constant. The results (not shown here) showed that the farther the mass sink is placed away from the equator, the faster breakdown will occur. This is expected because since the zonal wind shear around the mass sink is produced by the effect of the Coriolis force, the farther this forcing is from the equator, the faster the monsoon-like shear layer will evolve, expediting the breakdown process.

Another feature observed in the model results is that the larger the zonal extent of the PV anomaly, the slower the breakdown process evolves and the smaller its cyclonic tilt with respect to the equator.

Results obtained by varying the width of the PV anomaly show that wider strips break down into vortices of larger horizontal scales, as expected from previous work (Guinn, 1992) and dictated by the linear stability theory.

4.4 Distorted Ellipsoidal Mass Sink

Often times in the Eastern Pacific, the ITCZ is wider near Central America, perhaps reflecting the sea surface temperature pattern in that region and the presence of the American continent. It is also near Central America that the majority of hurricanes form in the E. Pacific. Figure 4.11 shows the formation of Hurricane Aletta in late May, 1978. On May 28, the ITCZ in the E. Pacific is an elongated line of convection that is wider on its eastern side. A tropical storm formed on the 30th near the coast of Mexico where the

ITCZ was wider. On May 31 the storm was upgraded to Hurricane Aletta and continued moving to the NW with landfall in Mexico that same day (Gunther, 1979).

In this section, experiments with a mass sink that is wider on its eastern side are performed in order investigate how this may change the ITCZ breakdown and whether it can account for cases like Hurricane Aletta and perhaps offer an alternative explanation to the higher frequency of tropical cyclone genesis events near the Central American coast.

The asymmetric mass sink used in this section is obtained by setting the distortion parameter, γ_{dist}, in equation (4.5b) to

$$\gamma_{dist} = \frac{\alpha_i(\alpha_r - 1)}{\alpha_r\, c}\left[a\lambda\cos\phi - \frac{c}{2} + \frac{\alpha_r\, c}{(\alpha_r - 1)}\right]$$

where α_i and α_r determine how much the original ellipse is distorted.

Figure 4.12 shows the evolution of the height, wind and PV fields produced by a zonally oriented distorted ellipsoidal mass sink centered at $\phi_c = 10°N$, with $c = 40$, $d = 4$, $\tau = 4$, $\alpha_i = 2$ and $\alpha_r = 2$. In this mass sink, the width at $c/2$ is twice that at $-c/2$. The experiments shown in this section are run using truncation T126 rather than T213. Similarly to the evolution of the elliptical mass sink, the flow produced by the mass sink is barotropically unstable after a couple of days of forcing. After 5 days, the cyclonic region produced by the mass sink is slowly rotating cyclonically around its axis, beginning the axisymmetrization process. After 10 days, axisymmetrization is occurring as the initially elongated PV strip sheds two high PV filaments. After 15 days, one cyclone has been produced where one of the filaments is still apparent.

Figure 4.13 shows the solution after 15 days for a mass sink of the same dimensions of the mass sink above, but perfectly elliptical rather than distorted. It shows that when the mass sink is elliptical, the resultant PV strip breaks down into three vortices as opposed to symmetrizing into one as in the distorted case.

Additional experiments run with longer mass sinks showed that the longer the mass sink, the wider its eastern side has to be in order to suppress breakdown and produce axisymmetrization into only one vortex instead.

The model results shown so far, support the possibility that barotropic instability is an important component of the ITCZ breakdown process. Some observational support to the occurrence of ITCZ breakdown in the E. Pacific is provided in the next section.

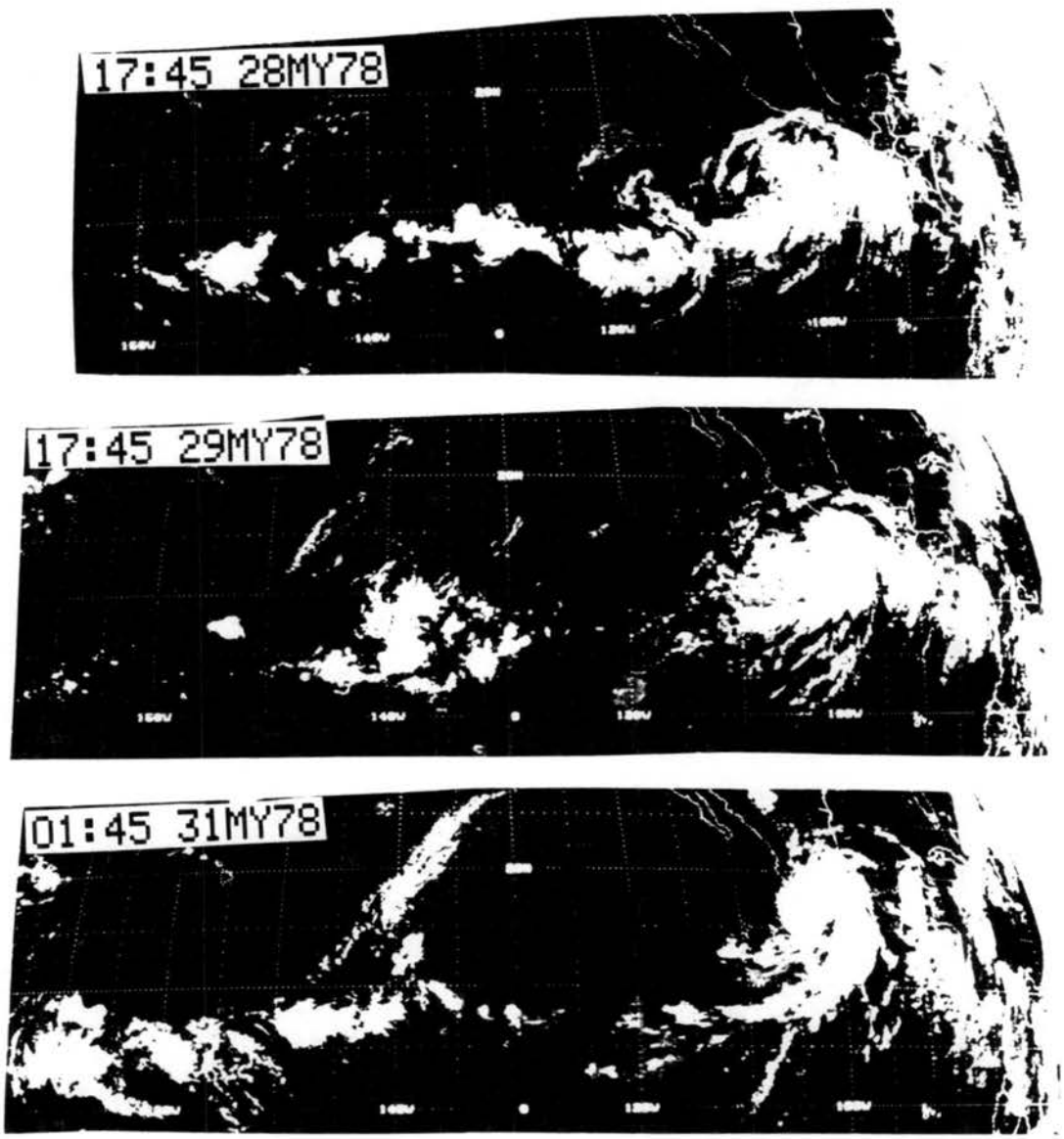

Figure 4.11: GOES IR satellite images for 28, 29 and 31 of May, 1978, showing the formation of Hurricane Aletta (time is in UTC).

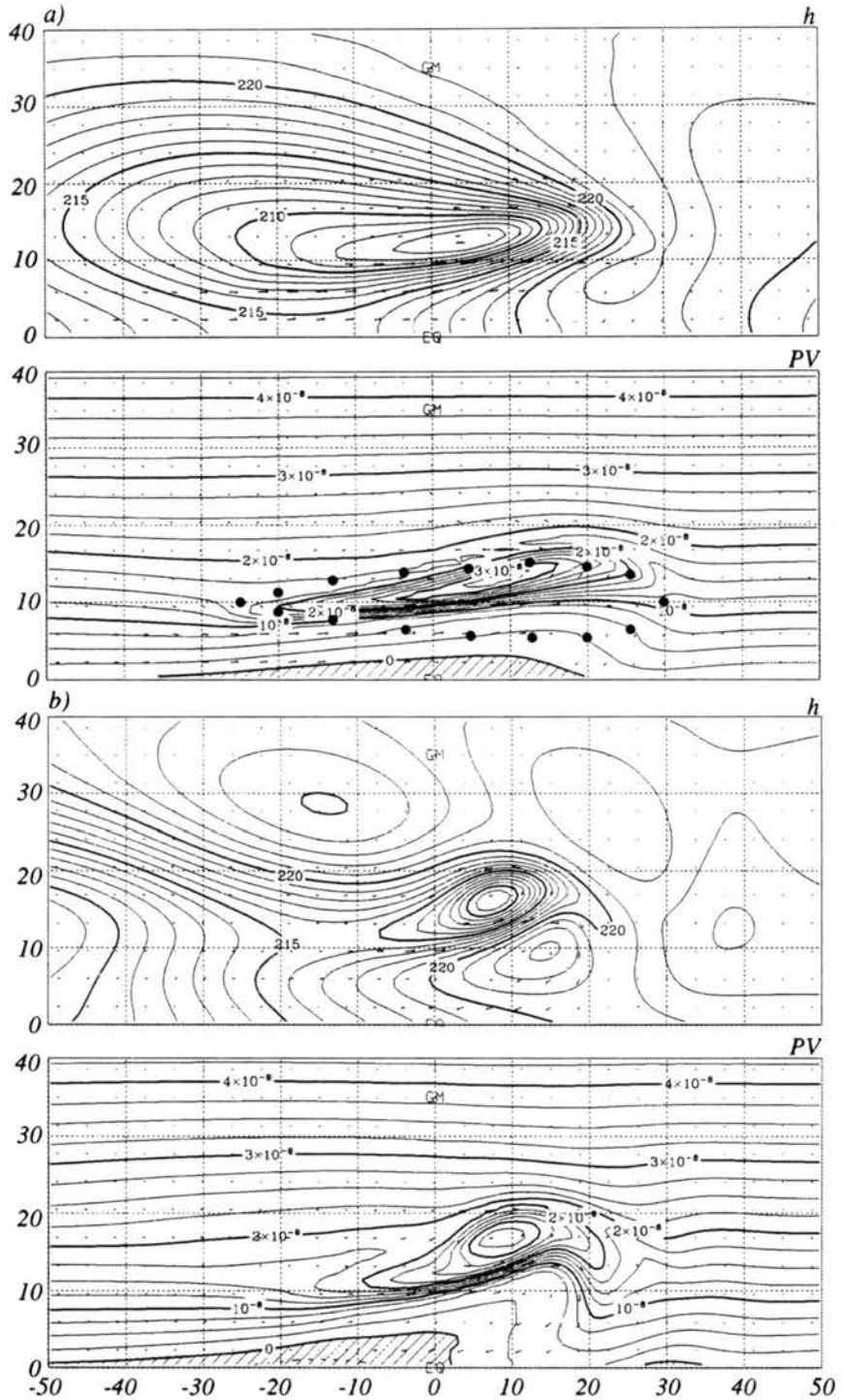

Figure 4.12: Evolution of a zonally oriented distorted ellipsoidal mass sink centered at $\phi_c = 10°N$,, with $c = 40$, $d = 4$, $\tau = 4$, $\alpha_i = 3$ and $\alpha_r = 3$. Heavy dots indicate shape and position of mass sink; *a)* Height (m), wind (m/s) and PV ($s\,m^{-2}$) fields at 5 days; *b)* Same at 10 days.

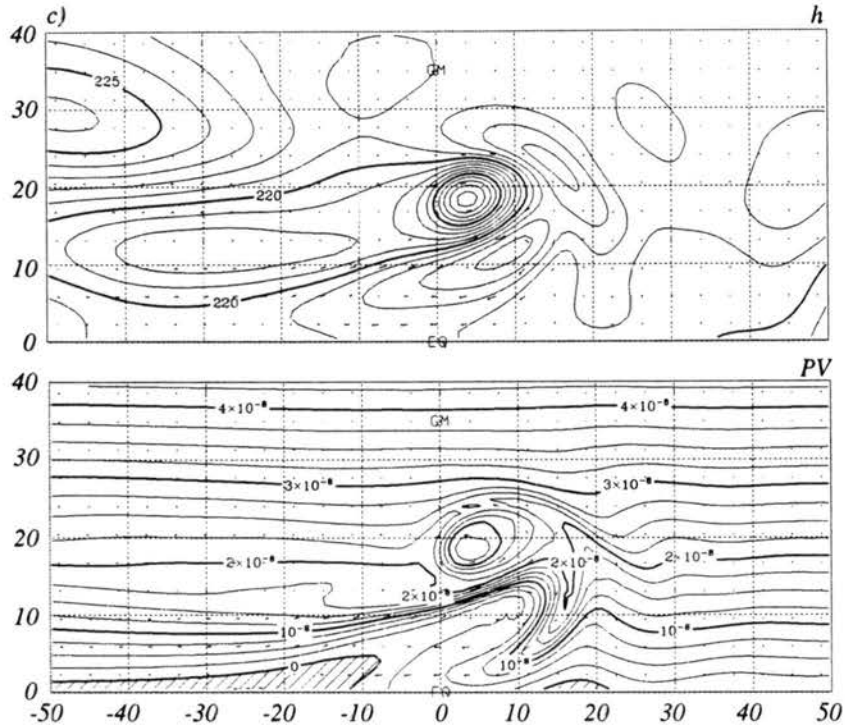

Figure 4.12: *b)* Same at 15 days.

4.5 Frequency of Tropical Cyclone Genesis in the Eastern Pacific

Figure 4.14 shows all Eastern Pacific tropical cyclones of at least tropical storm intensity that occurred from 1980 to 1993. The storms are dated by their first denotation as a tropical depression. In average, 18 tropical storms formed every year in that basin, 10 of which reached hurricane intensity. The average duration of the tropical cyclone season for that period was 148 days, implying an average time interval between the formation of two storms (hereafter referred to as intergenesis period) of about 8.4 days. It is evident in figure 4.14 that tropical cyclones tend to cluster in time, with periods of frequent cyclogenesis interspersed with inactive periods. This time clustering becomes more evident in figure 4.15, which shows the frequencies of intergenesis periods for the storms in figure 4.14. About 51% of these storms formed within 6 or less days from each other.

Gray (1979) observed a similar tendency for tropical cyclones to cluster in time on a global scale, with active tropical cyclone periods lasting about 1-2 weeks, followed by 2-4 week long inactive periods. He proposed that large scale, slowly varying anomalies alter the

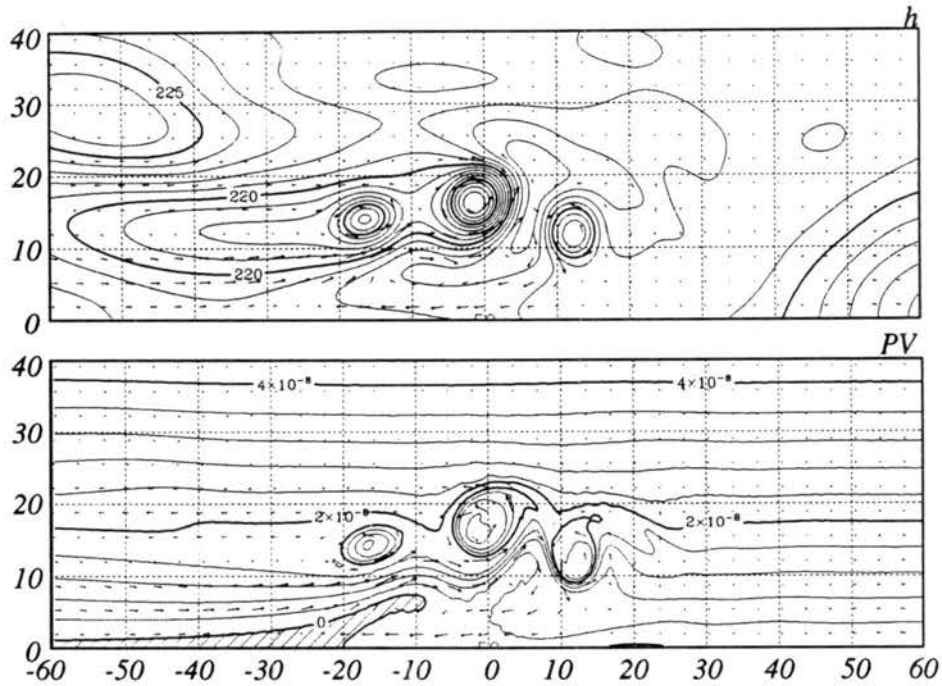

Figure 4.13: Evolution of a zonally oriented elliptical mass sink centered at $\phi_c = 10°N$, with $c = 40°$, $d = 4°$ and $\tau = 4$. Heavy dots indicate position and shape of the mass sink. Height (m), wind (m/s) and PV ($s\,m^{-2}$) fields at 15 days.

environmental genesis parameters such as to periodically hinder or enhance cyclogenesis, resulting in the observed time clustering.

Liebmann *et al.* (1993) suggested that the Madden-Julian Oscillation could be responsible for time clustering of tropical cyclones in the Indian and West Pacific Oceans. They observed that more tropical cyclones form in these regions during the wet phase of the MJO, when a larger number of tropical depressions are present.

Zehnder (1991) observes similar time clustering of tropical cyclones in the E. Pacific Ocean. He proposes that the interaction of a quasi-persistent favorable large scale flow with the topography could explain the clustering in time (and space) of tropical cyclogenesis in the Eastern Pacific.

Another possible explanation for this observed time clustering of tropical cyclones is the ITCZ breakdown. As seen in the previous sections, the ITCZ breakdown would tend to produce several tropical cyclones in an interval of a few days. The observed inactive periods of cyclogenesis could be accounted for by the need of some time for the ITCZ to reorganize and produce a shear zone.

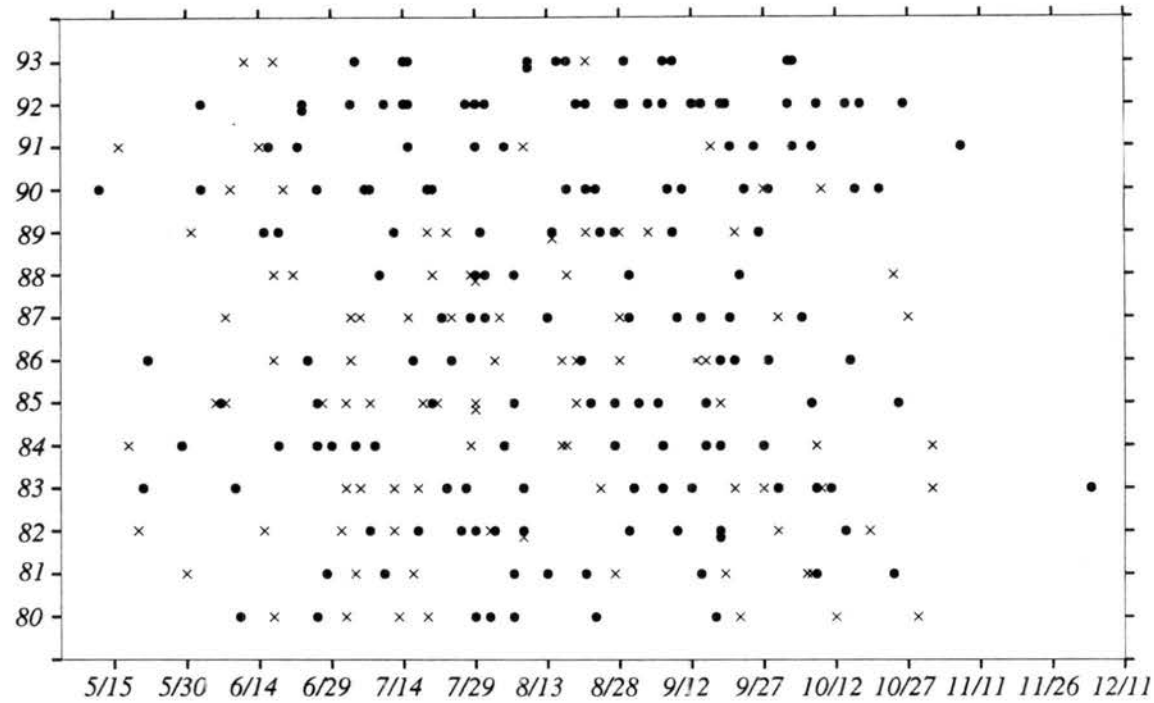

Figure 4.14: Tropical storms in the E. Pacific between 1980 and 1993. Tropical storms are denoted by crosses and hurricanes by dots.

Approximately 46% of the storms in figure 4.14 formed within 0 to 4 days apart. Figure 4.16 shows the initial longitude and reference date of each storm in clusters of storms that formed within 4 days of each other. It is noteworthy that in 60% of these time clusters, the formation of the westernmost storm precedes that of the easternmost ones. This tendency has also been observed in the W. Pacific (Frank, 1982).

For the storms in the time clusters defined above, figure 4.17 shows the frequencies with which storms formed at certain longitudinal distances from each other. About 50% of the tropical storms formed between 5 and 14° from each other.

The above observed clusterings in time and space and the sequential formation of tropical storms from west to east are also characteristics of the ITCZ breakdown as seen in section 4.3. This offers some support to the possibility that the ITCZ breakdown may actually occur in the E. Pacific.

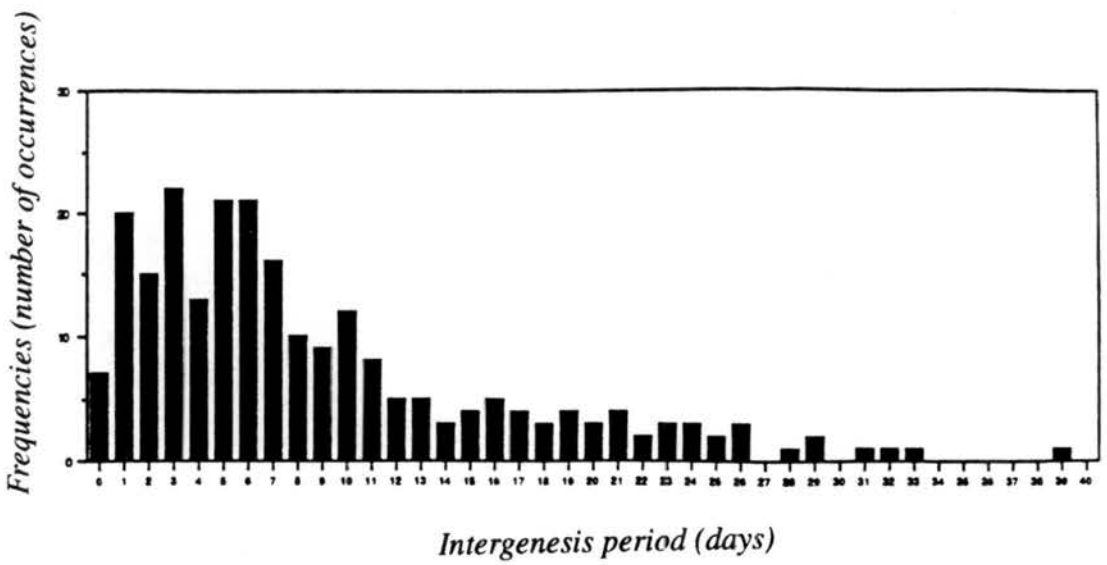

Figure 4.15: Frequencies of occurrence of intergenesis intervals (in days) between all storms during 1980 through 1993.

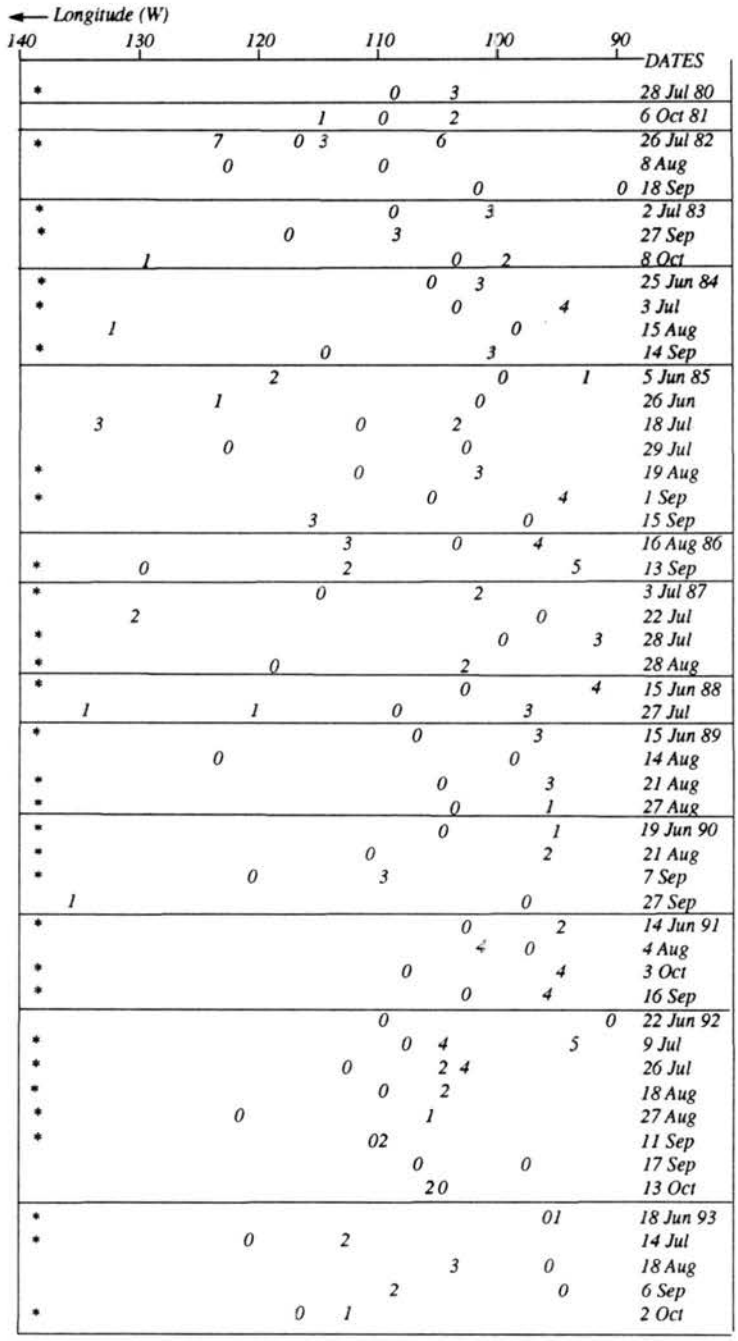

Figure 4.16: Longitudes of formation of storms found in time clusters from 1980 to 1993. Dates on the right column indicate date of formation of storm '0'. Storm '1' formed a day later, and so forth.

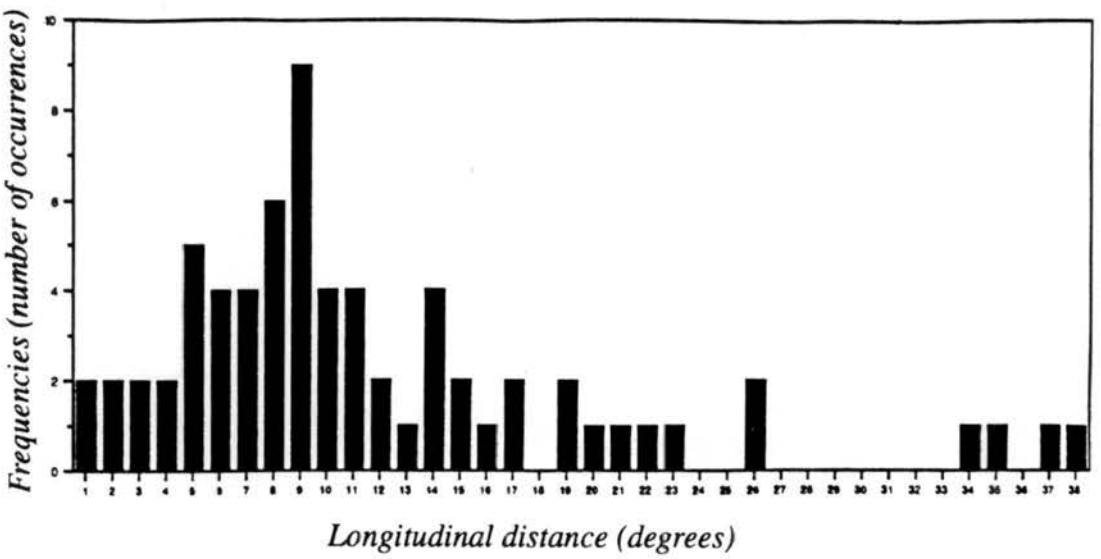

Figure 4.17: Frequencies of occurrence of longitudinal distances between storms that formed within the same time cluster.

Chapter 5

TWIN TROPICAL CYCLONES

Exclusively in the West Pacific and Indian Oceans, there are occasions of nearly simultaneous formation of two tropical cyclones straddling the equator at about the same longitude and between $10°N$ and $10°S$. These storms are called twin tropical cyclones, reflecting their symmetry about the equator, or simply tropical cyclone pairs.

In section 5.1, observational work on twin tropical cyclones is reviewed and a subjective 11 year climatology of their occurrence is presented. Shallow water model experiments illustrating twin tropical cyclone formation are shown in section 5.2. A possible explanation for the existence of preferred regions for twin tropical cyclone formation is offered in section 5.3. Finally, section 5.4 presents some results of initial value problems on tropical cyclone twin movement.

5.1 Observations

In the W. Pacific, twin tropical cyclones occur between October and May, with higher frequencies during the austral summer (Keen, 1982). The occurrence of tropical cyclone twins requires the presence of a super cloud cluster at the equator. This requirement precludes the occurrence of W. Pacific twins in the austral winter, when the ITCZ in the W. Pacific attains its farthest position from the equator (figure 1.2). In the Pacific Ocean, east of the dateline, and in the Atlantic Ocean no tropical cyclones occur south of the equator because the ITCZ is always in the Northern Hemisphere.

In the past few years, twin tropical cyclones have received increased attention in the literature due to their possible connection with westerly wind bursts and the El Niño phenomenon.

Nakazawa (1988) found that the convection associated with each active phase of the MJO is composed of several super cloud clusters (SCC) that move eastward. Super cloud clusters are areas of convection of horizontal scale on the order of $10^3\ km$ that propagate eastward at speeds between 5 and 15 m/s and last from 2 to 10 days (Nakazawa, 1988; Sui and Lau, 1992; Mapes and Houze, 1993). The building blocks of each SCC are westward moving cloud clusters of horizontal scale on the order of $10^2\ km$ and life times between 1 and 2 days. The eastward propagation of the SCC is due to the continuous formation of new cloud clusters on its east side.

Observational studies have shown that the convection (SCC) associated with the MJO forms and intensifies while stationary in the central equatorial Indian Ocean. The SCC then slightly weakens while moving over Indonesia. Upon reaching the W. Pacific, the convection again intensifies near $160°E$, and finally becomes stationary and dies off near the dateline (Wang and Rui, 1990; Weickman and Khalsa, 1990).

Westerly wind bursts (WWB) are sporadic periods of intense equatorial westerly winds that occur in the warm pool region and may last for up to a few weeks (Torrence, 1993; Hartten, 1993). During WWB, the low level winds at the equator, which are usually easterly, blow from the west at speeds in excess of $\sim 10\ m/s$. The origin of the WWB is still a subject of debate. Possible mechanisms to produce and intensify WWB are cold surges originating in the midlatitudes (Love, 1985), or the MJO and its associated SCC (Nakazawa, 1988; Lau *et al.*, 1989; Sui and Lau, 1992), or still the genesis and intensification of tropical cyclones near the equator (Philander, 1990; Raymond, 1993; Phoebus, 1993; Chen, 1993). In particular, it has been observed that equatorial westerly winds are sharply strengthened in the presence of twin tropical cyclones within about 10° of the equator (Lander, 1990; Phoebus, 1993).

The causal relationships between WWB and the El Niño are not yet well understood. However, it is believed that the former produces a perturbation in the ocean in the form of an equatorial Kelvin wave that advects warm water eastward along the equator, perhaps contributing to triggering or enhancing El Niño events (Luther *et al.*, 1983; Miller *et al.*, 1988; Phoebus, 1993; Torrence, 1993).

The discussion above suggests a possible link between the formation of twin tropical cyclones and El Niño events which remains to be further investigated.

5.1.1 A 'Canonical' Tropical Cyclone Pair

A series of GMS (Japanese Geostationary Meteorological Satellite) infrared satellite images illustrating the formation and evolution of a set of twin tropical cyclones in the Western Pacific in 1986 is shown in figure 5.1. On May 12 through 14, an SCC was located on the equator at $\sim 155°E$. Two days later, on the 16th, the convection right on the equator had decreased and two circular regions of convection had formed a few degrees away from and on either side of the equator. On May 17, these two regions of convection had evolved into two tropical cyclones straddling the equator. These twin tropical cyclones later became Supertyphoon Lola and Tropical Cyclone Namu and moved apart and away from the equator. This set of twins caused a strong WWB in the Western Pacific that produced a disturbance in the sea level of maximum amplitude of 13 cm which was observed to propagate across the Pacific ocean reaching $98°W$ (Miller *et al*, 1988). This set of twin tropical cyclones and their associated WWB are among four cases of twins that happened in 1986 in the W. Pacific and are believed to have contributed to triggering the 1986-1987 El Niño.

According to the ECMWF (European Centre for Medium Range Weather Forecast, 1987) 850 mb wind analyses, from mid April through May 9, easterly winds prevailed at the equator in the W. Pacific basin. Selected ECMWF 850 mb wind analyses during May 1986 are shown in figure 5.2. Westerly winds first appeared at the equator on May 9. Within the next few days, these westerly winds were intensified by the SCC shown in figure 5.1. On May 14, the westerly wind burst had increased in areal extent and attained its easternmost position. Also on the 14th, the two cyclonic circulations straddling the equator were first noticeable. On May 17, the WWB attained its highest intensity, with wind speeds in excess of 15 m/s in the region between the two tropical cyclones. As the tropical cyclones moved away from the equator, the equatorial westerlies decreased in both intensity and areal extent and retreated to the west (see ECMWF analysis for May 20, for instance). On May 22 easterly winds again prevailed in the W. Pacific. This pattern of

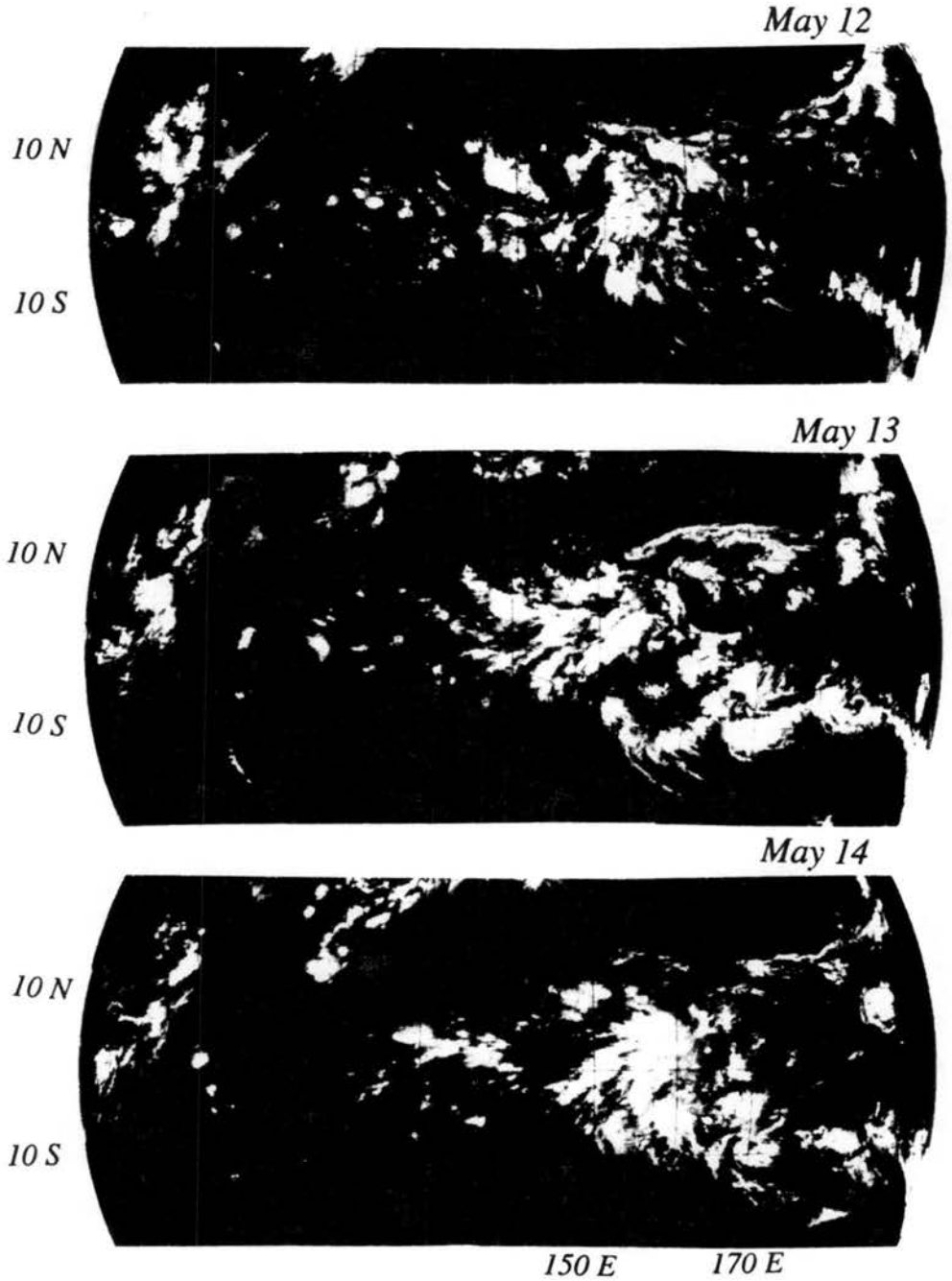

Figure 5.1: GMS IR images for May 12 through May 20, 1986, showing the formation and evolution of twin tropical cyclones in the W. Pacific Ocean. The storms were called Supertyphoon Lola and Tropical Cyclone Namu, in the Northern and Southern Hemispheres, respectively. Images are every 24 hours at 03:00Z (JMSC,1986)

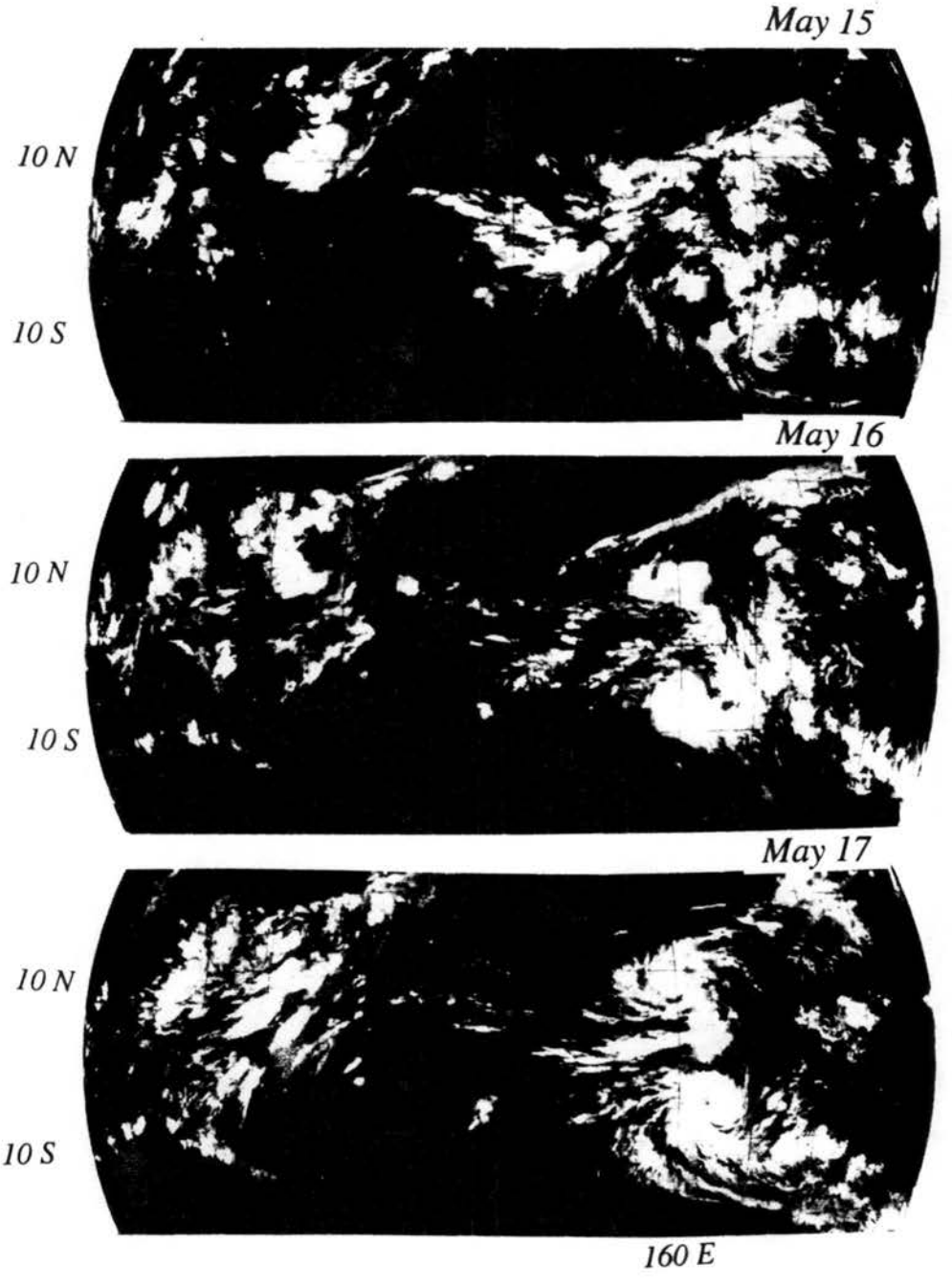

Figure 5.1: Continued.

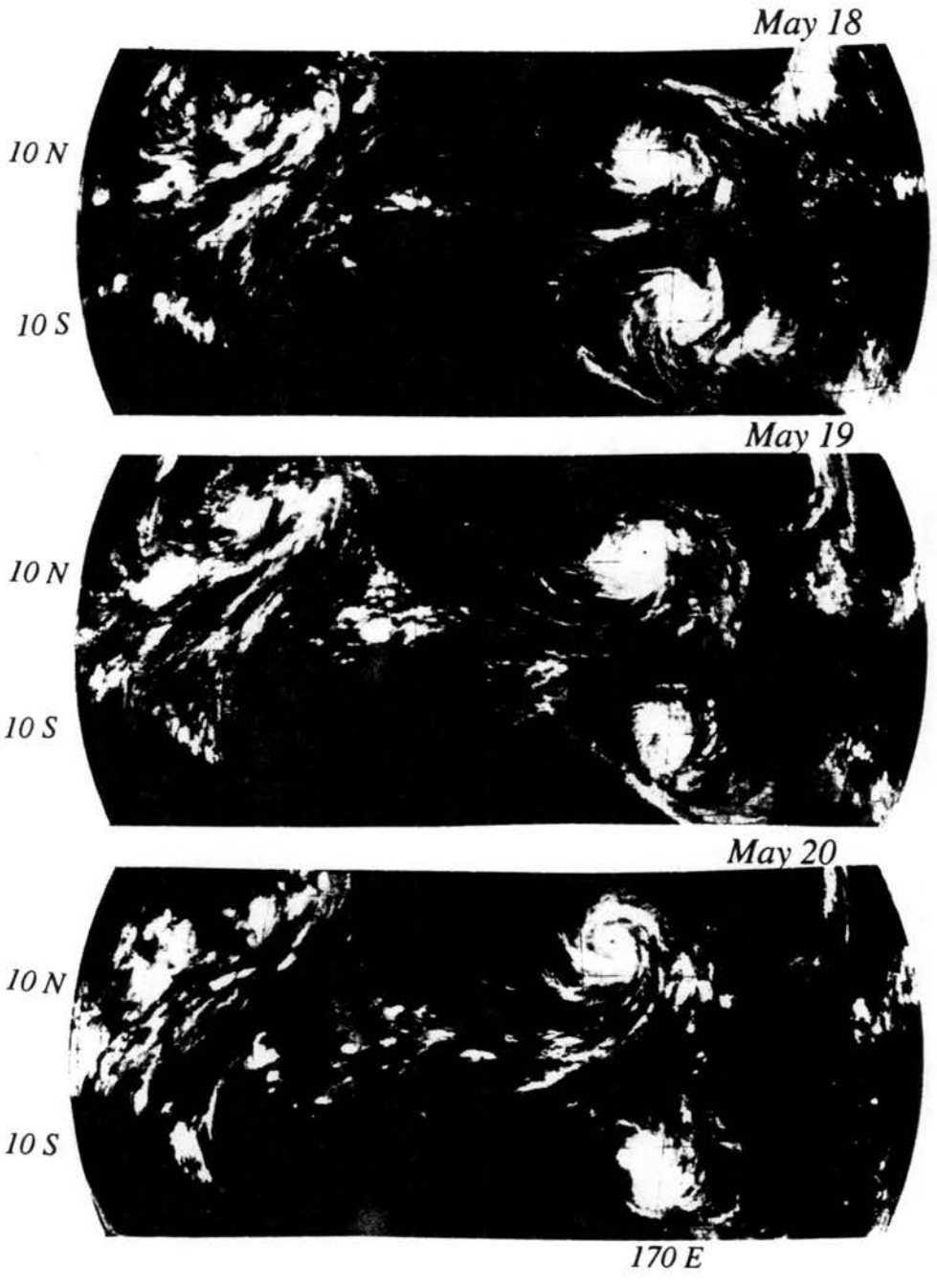

Figure 5.1: Continued.

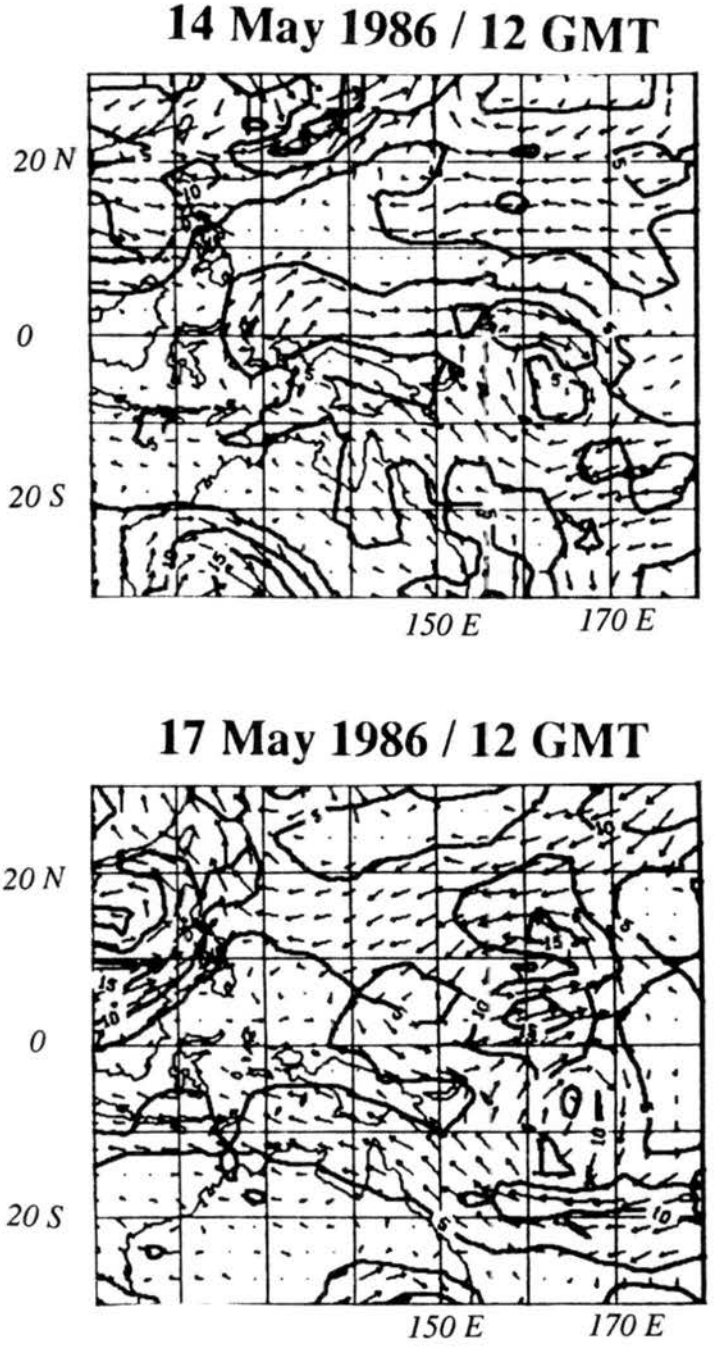

Figure 5.2: ECMWF 850 mb wind analyses for the Western Pacific during the formation and demise of Supertyphoon Lola and Tropical Cyclone Namu. Analyses are for May 8, 10, 14, 17, 20 and 22, 1986 at 12 GMT (ECMWF, 1987).

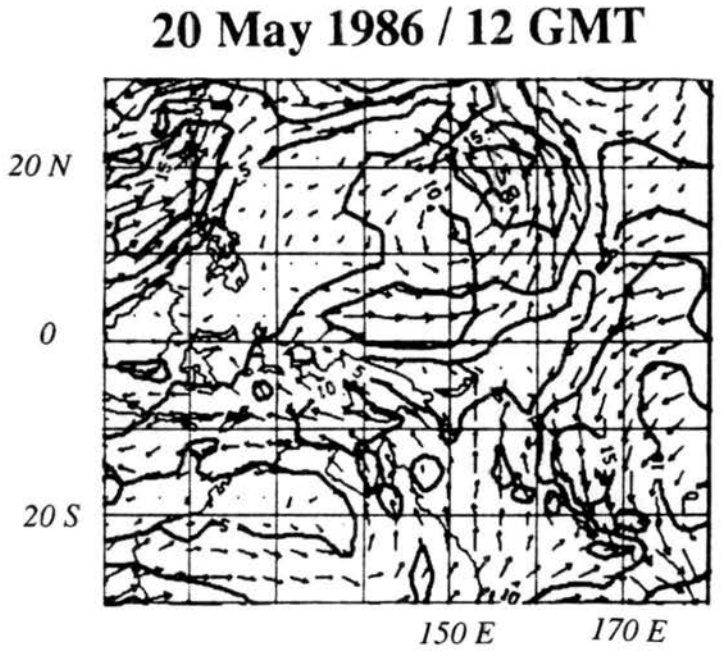

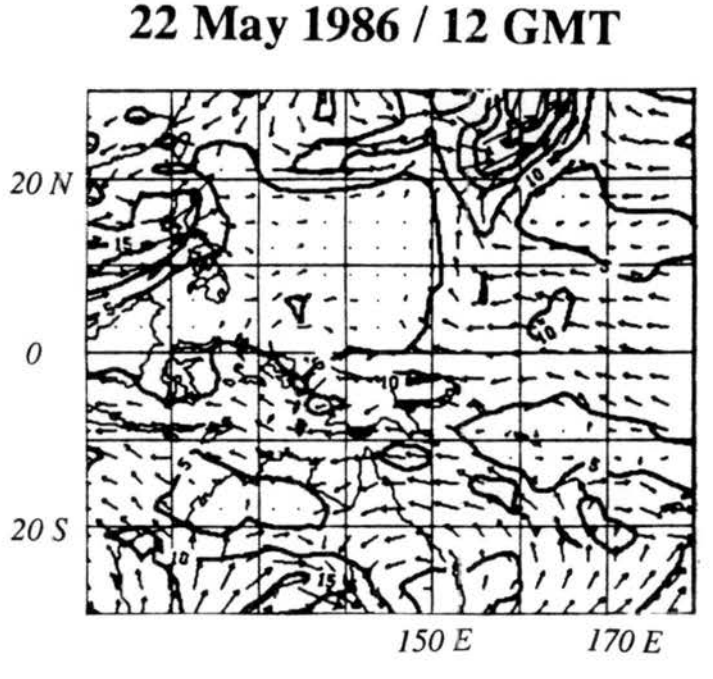

Figure 5.2: Continued.

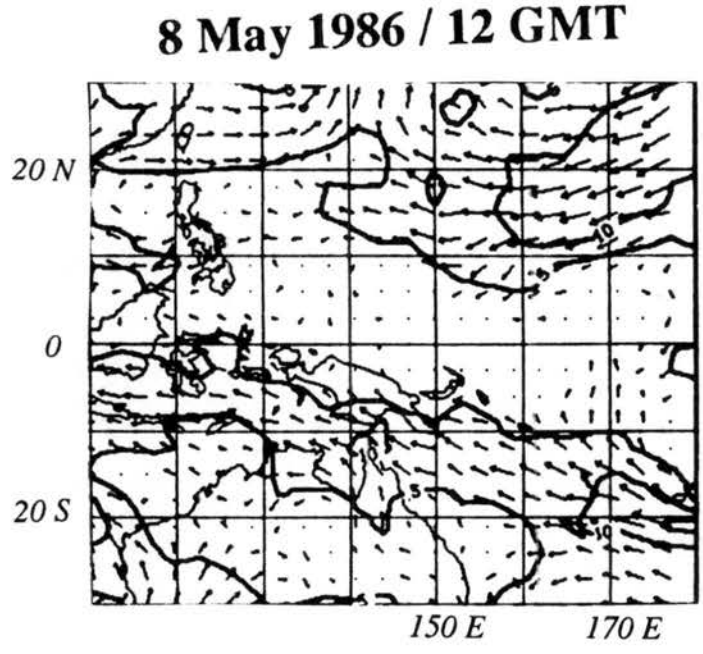

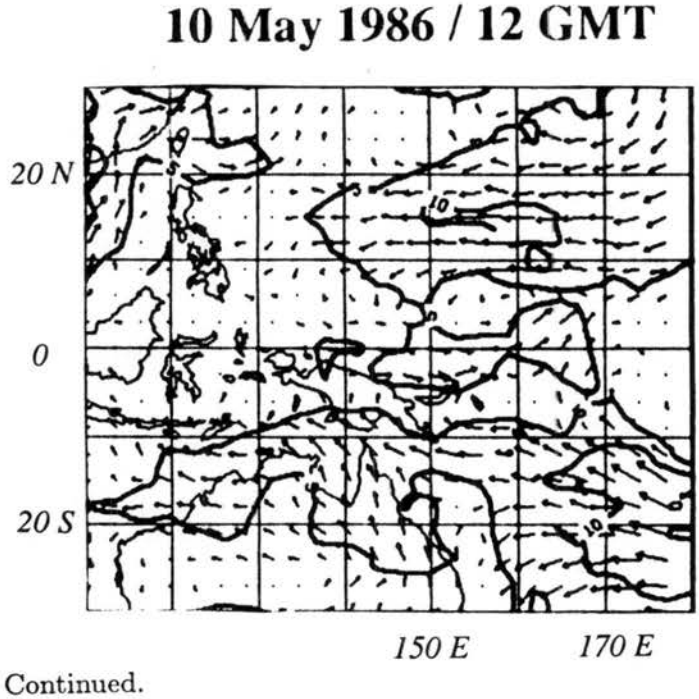

Figure 5.2: Continued.

evolution of the WWB consisting of formation, eastward advance and intensification, and retreat and decay, is also observed by Phoebus (1993) in connection with different sets of twins.

Both the cloud patterns and the circulations described above are believed to be typical to the formation and evolution of twin tropical cyclones. The sequence of events that lead to the formation of the tropical cyclone twins may be summarized as follows: *a)* a SCC and its associated westerly winds are located across the equator; *b)* a few days later, the convection dies off at the equator and two new regions of cyclonic circulation and strong convection appear straddling the equator to the west of the original SCC; and finally *c)* the two regions of convection on either side of the equator produce twin tropical cyclones. Lander (1990) points out that a dynamically similar evolution is obtained by Gill (1980) in a linear, steady state shallow water model when a mass sink is applied at the equator. In that model, on the eastern side of the mass sink, easterlies are produced by eastward propagating Kelvin waves and to the west of the mass sink, westerlies occur due to Rossby wave influence. Another effect of the Rossby waves is the formation of the two cyclonic regions straddling the equator. This circulation pattern is also seen in the composite wind fields for four SCCs shown in Nakazawa (1988). Lander (1990) proposes that the two cyclonic circulations straddling the equator described above are the precursors of tropical cyclone twins.

The two cyclonic circulations mentioned above may be interpreted as tropical disturbances. The formation or not of tropical cyclones in these disturbances depends on the occurrence of the remaining steps in figure 1.1. Several occasions were observed when the two circulations were apparent in the satellite images, but did not produce two tropical cyclones.

5.1.2 A Short Climatology of Tropical Cyclone Twins

Table 5.1 lists tropical cyclone twins that occurred during 11 years, from January 1983 to December 1993, in the tropical belt comprised between $70°E$ and $150°W$. Inspection of that region in search of tropical cyclone twins was subjective and so was the decision process of whether or not an event was found. The tropical cyclone twins listed in table

5.1 share the following common characteristics: *a)* they formed nearly simultaneously in association with the same SCC; *b)* they formed within 10° longitude of each other; *c)* they formed on either side of the equator, no farther than 20° apart in latitude; and *d)* they subsequently moved into higher latitudes. The twins are listed by dates when their parent SCCs were still present at the equator and by an average longitude were they first formed.

Twin Tropical Cyclones			
Date			Longitude ($°E$)
6	Dec	84	135
2	Jan	86	80
18	Apr	86	150
3	May	86	85
14	May	86	160
8	Dec	86	170
19	Dec	86	180
2	Apr	87	155
1	Jan	88	170
14	Dec	90	170
3	May	91	155
2	Jan	92	170
8	Mar	93	165

Table 5.1: Dates and approximate longitude of formation of twin tropical cyclones between January 1983 and December 1993 in the tropical strip between $70°E$ and $150°W$.

Table 5.1 shows that in the W. Pacific, twin tropical cyclones were observed once a year between $155°E$ and the dateline. Another interesting feature in table 5.1 is that four out of the 11 cases of twins occurred in 1986 in the Western Pacific. If this is taken into account, the average frequency of observed twin formation comes down to one case every one and a half years in the W. Pacific. Lander (1990) says that this frequency is about one case every two or three years while Keen (1982) observes two per year. The differences in observed frequencies are due to differences in the definition of tropical cyclone twins as well as differences in the periods of time considered. Note that table 5.1 contains

only the so called 'canonical' twins. However, some cases were observed in which the two cyclonic circulations straddling the equator were produced by an SSC, but only one cyclone resulted. Inclusion of these cases in this study would have resulted in a higher frequency of formation.

The high frequency of formation of twin tropical cyclones during 1986 is worthy of note, especially since there was an El Niño in 1986-1987. As mentioned before, the causal relationship between twin tropical cyclones and El Niño events is yet to be elucidated.

It is also worth mentioning that the formation of Supertyphoon Lola and Tropical Cyclone Namu occurred only about ten days after the formation of twin cyclones in the Indian Ocean. The formation of twins in the Indian ocean followed by occurrence of twins in the W. Pacific within a few days has been observed on other occasions. This suggests a dynamical link between these storms which may be provided by a planetary scale circulation system such as the MJO, for example. This possibility is investigated later on in this chapter in a series of shallow water simulations.

5.2 Twin Tropical Cyclone Formation

In this section, the formation of twin tropical cyclones is illustrated within the framework of a shallow water model. The model is initialized with a resting basic state upon which a meridionally elongated ellipsoidal mass sink is imposed. This mass sink is meant to simulate the presence of an SCC.

The mass sink used is given by equation (4.5), with $c = 10°$, $d = 15°$ (see figure 5.3*a*), $\tau = 5$ days (see figure 5.3*b*), $\overline{\Phi} = 2177.15\ m^2 s^{-2}$ and $\mid \partial\Phi/\partial t \mid = 864\ m^2 s^{-2} day^{-1}$.

Figure 5.4 shows the temporal evolution of h, PV and winds produced by the mass sink described above, when centered at the equator.

After one day of simulation, there is already evidence of Kelvin wave propagation to the east of the mass sink, where weak zonal easterly winds with extrema at the equator are observed. To the west of the mass sink, equatorial westerly winds produced by westward propagating Rossby waves are also present. The mass sink is producing two cyclonic anomalies on opposite sides of the equator. These cyclonic anomalies are produced by the

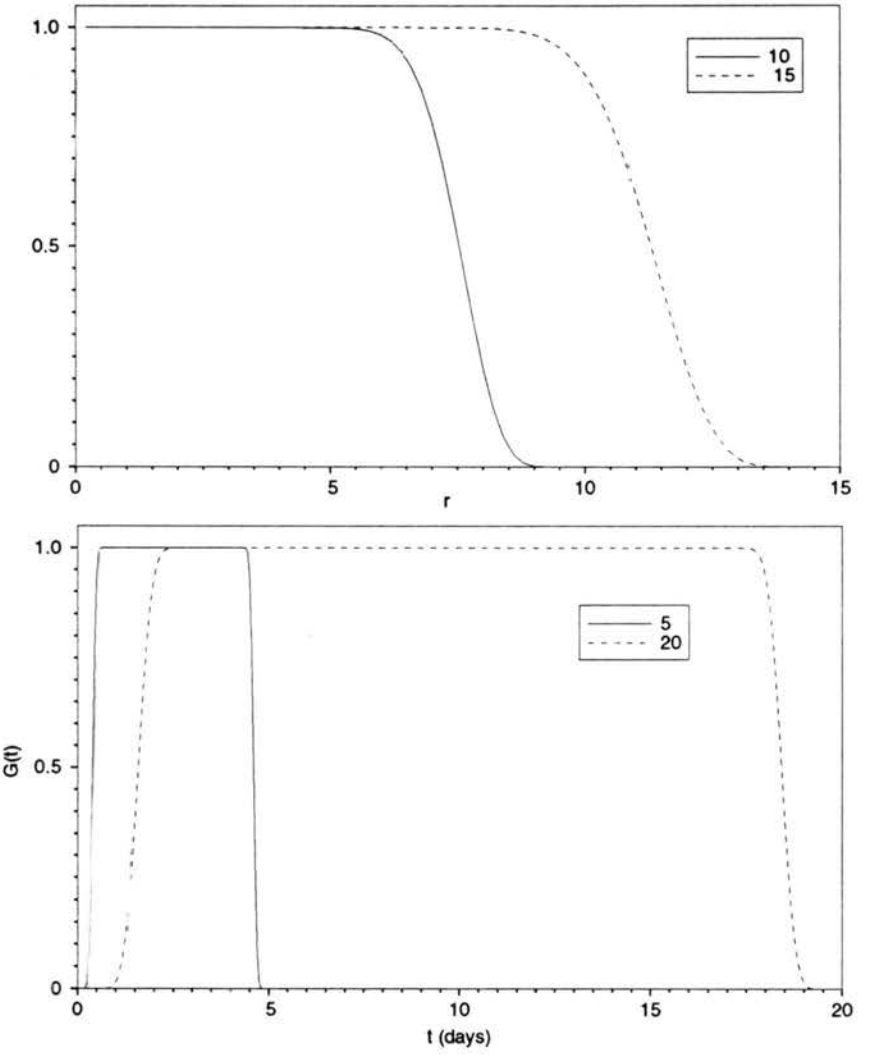

Figure 5.3: Nondimensional radial ($F(\lambda)$) and temporal ($G(t)$) variation of the mass sink as given be equations (4.2) and (4.3). *a)* $F(r)$ for $k_s = 30$, $c = 10°$ and $15°$. Radius is in degrees from the center of the ellipse; *b)* $G(t)$ for $k_t = 320.$ and $\tau = 5$ and 20 days.

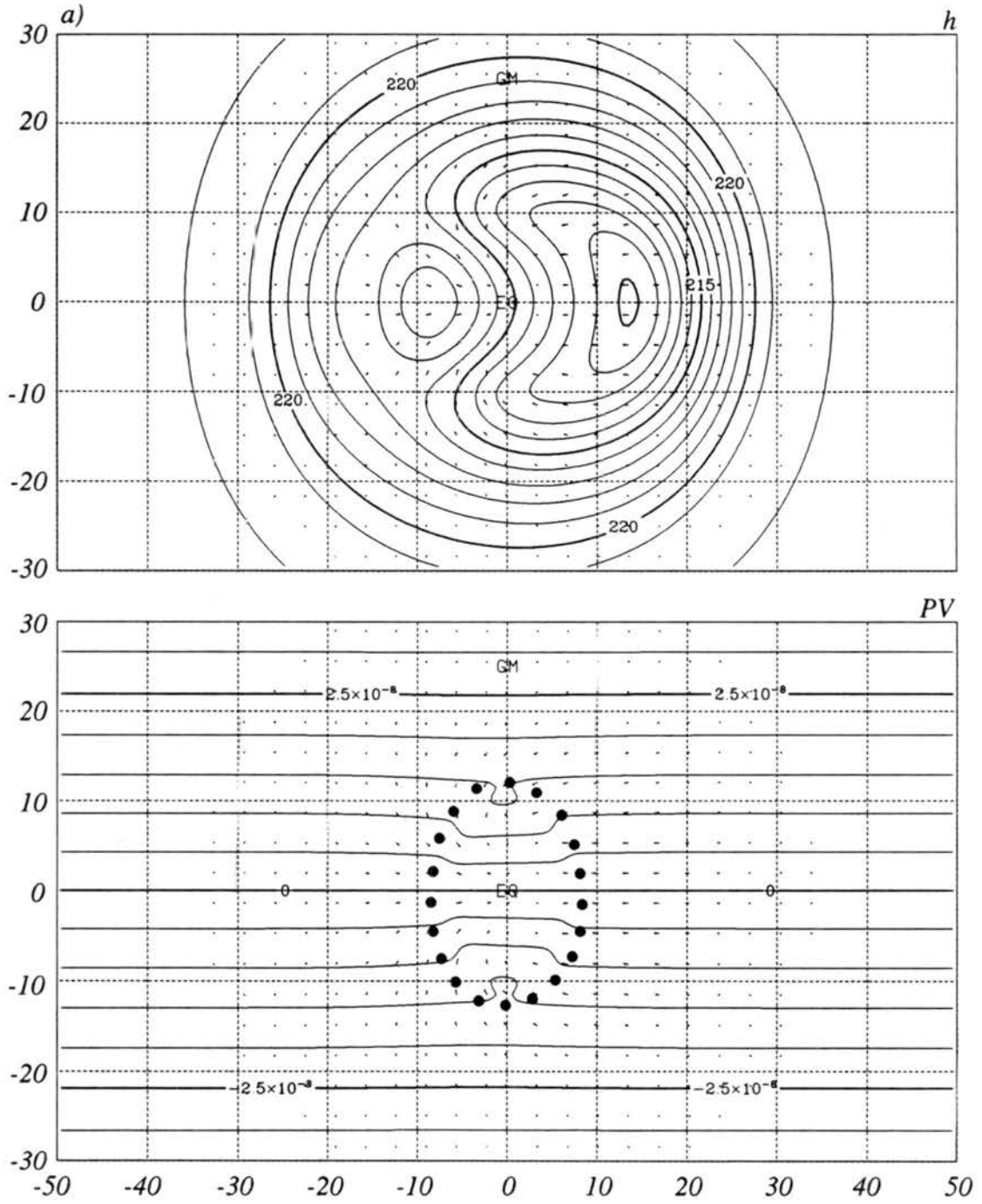

Figure 5.4: Evolution of PV ($s\,m^{-2}$), height (m) and wind (m/s) fields produced by a mass sink centered at the equator with $c = 10°$, $d = 15°$, $\tau = 5$, $\overline{\Phi} = 2177.15$ and $\mid \partial\Phi/\partial t \mid = 864\ m^2 s^{-2} day^{-1}$. Heavy dots indicate the shape and location of the mass sink. *a)* Solution at day 1.

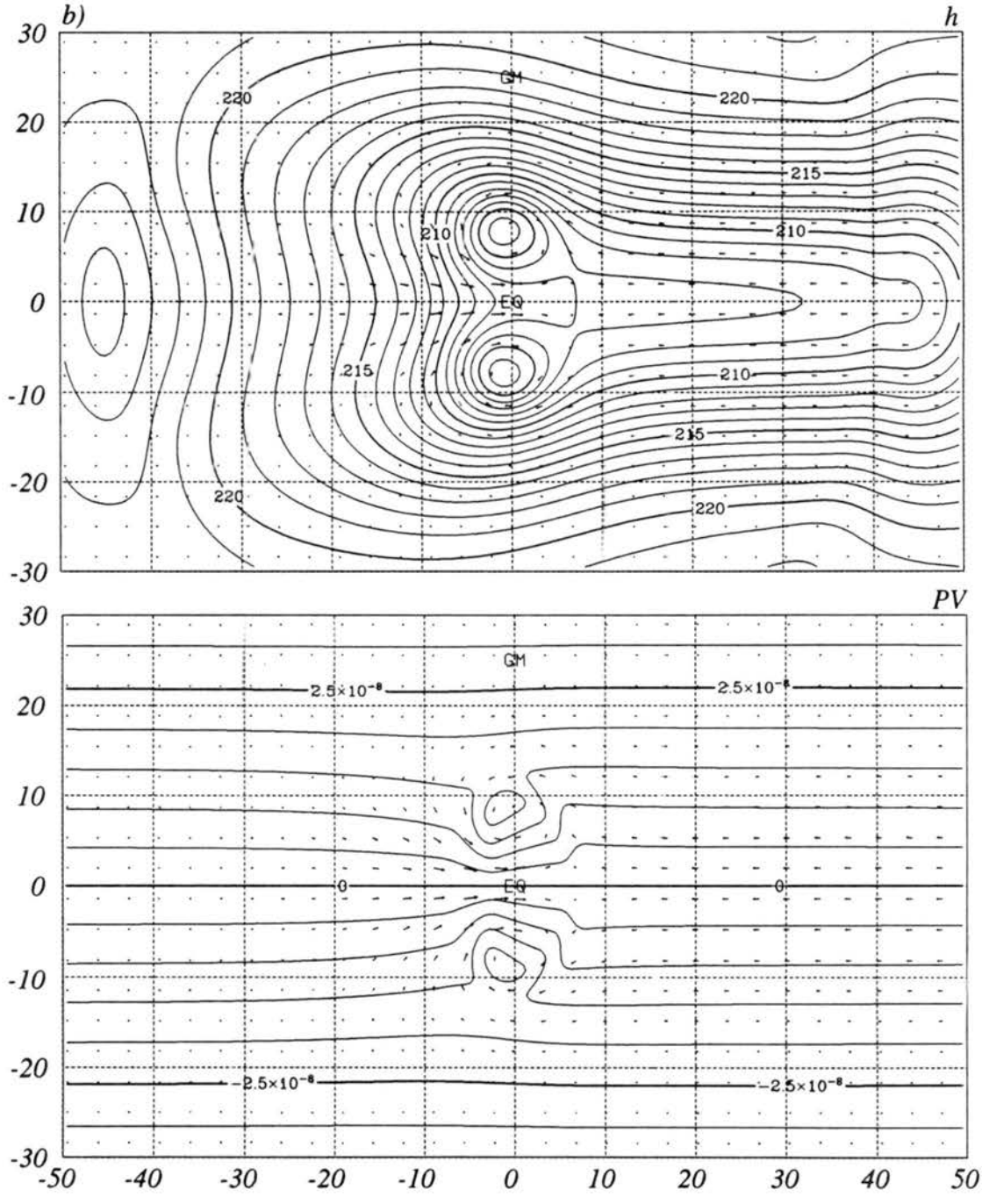

Figure 5.4: *b)* Same at 2 days.

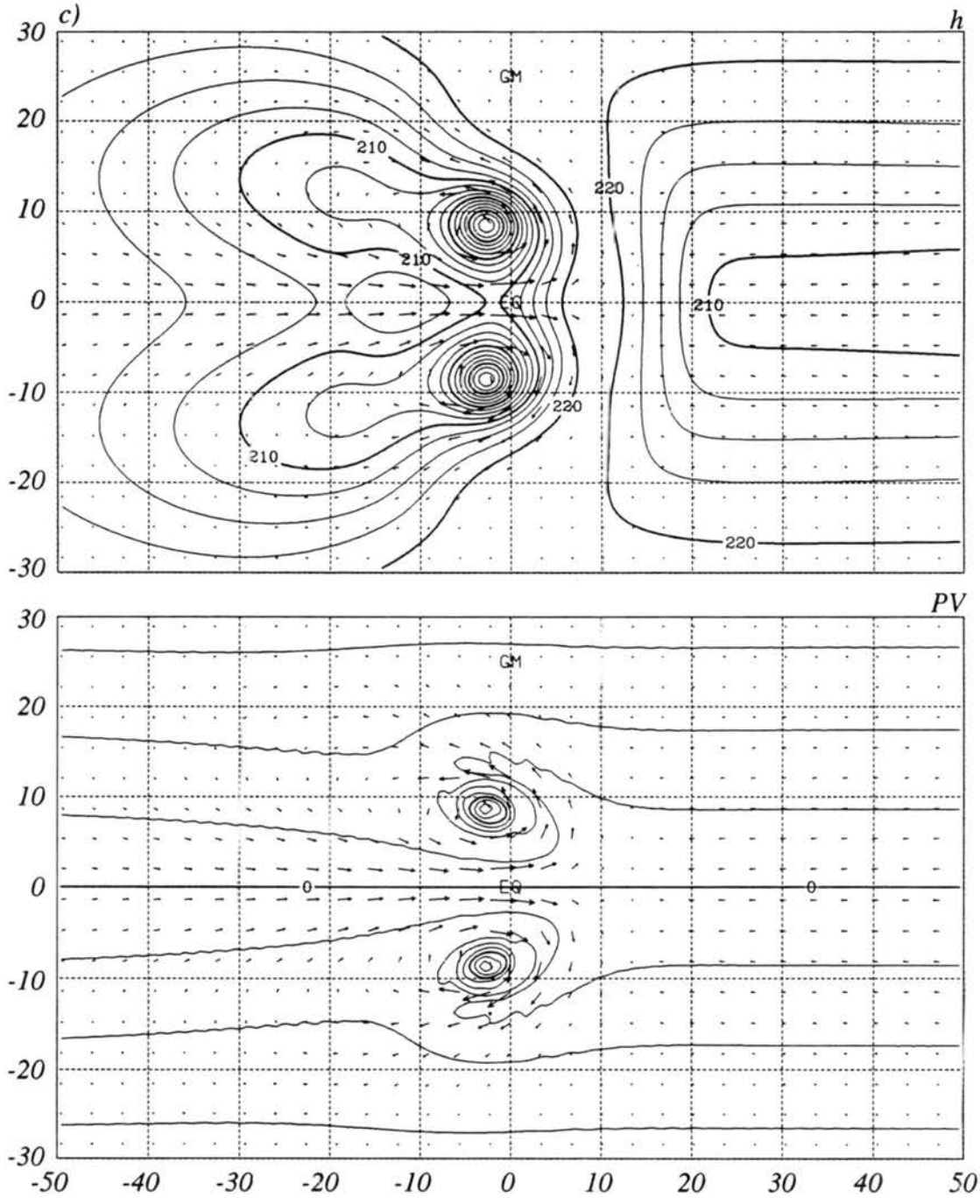

Figure 5.4: *c)* Same at 5 days.

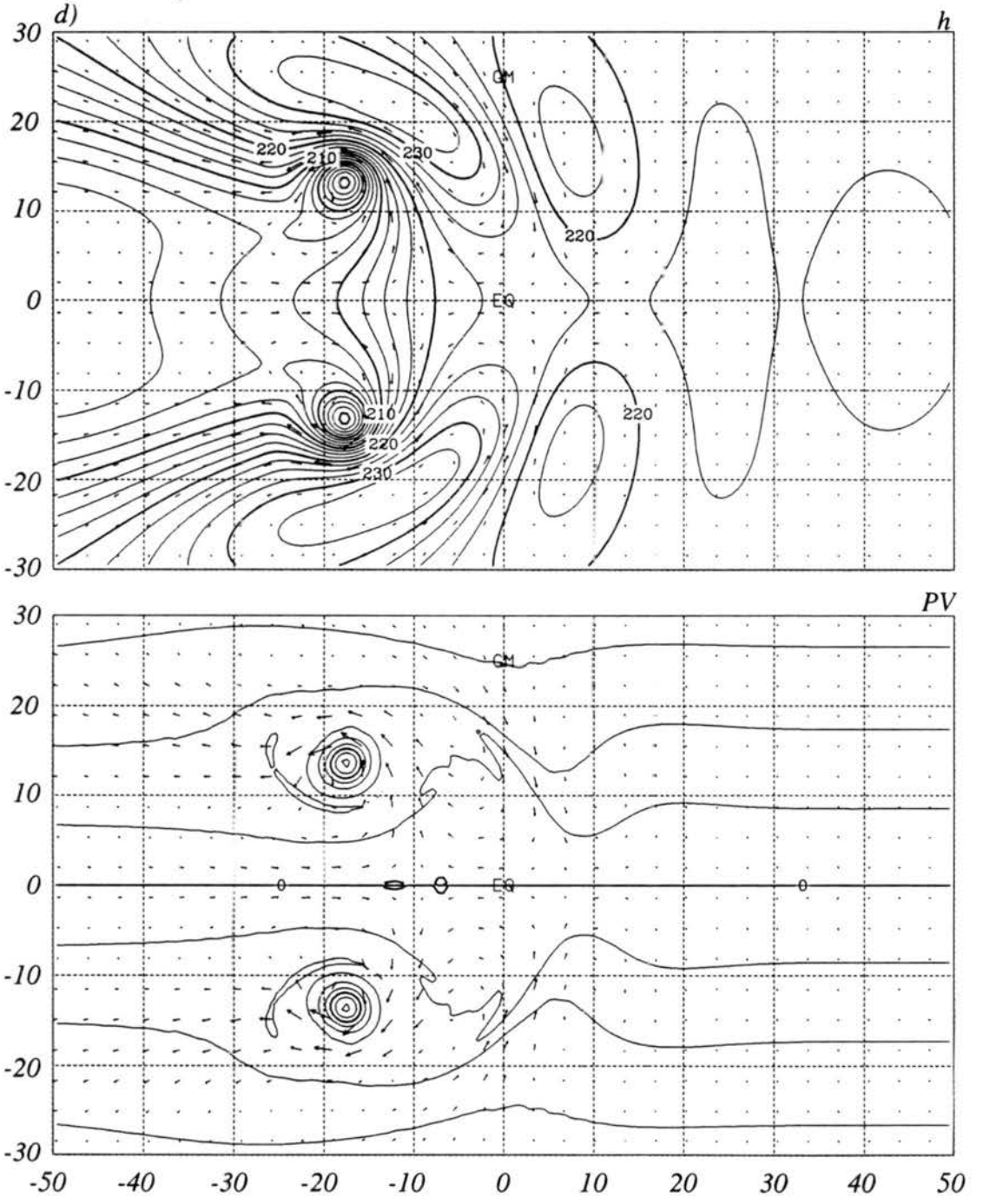

Figure 5.4: *d)* Same at 10 days.

mass sink through the $-(qQ/\Phi)$ term in the PV prognostic equation (2.14). Since this term is zero right on the equator, there is no anomaly produced there. These two cyclonic anomalies straddling the equator will intensify until the mass sink is turned off on day 5 of the simulation. On day two, the height and wind fields look very similar to the steady state results obtained by Gill (1980) when a mass sink is centered at the equator. The signatures of both the aforementioned Kelvin and Rossby waves are more pronounced and the winds are strengthening. The PV field shows two cyclonic regions symmetric about the equator and to the west of the mass sink. For as long as the forcing was active, a tightening of the PV isolines occurred near the equator. In the upper levels, the opposite, that is, a loosening of the PV isolines, would be expected. Interestingly, a loosening of the PV lines occurs in the W. Pacific and Indian Ocean 150 mb ECMWF analyses (Hoskins *et al.*, 1989; Hoskins, 1991). At five days, the mass sink is turned off and these two cyclones have attained their maximum intensity. At this point, the Kelvin wave is seen to leave the region of the mass sink and propagate to the east. The westerly winds at the equator have also reached their maximum speed which is of about 15 m/s. The leading edge of the westerly winds have their farthest east position during the simulation. It is after this point in time that the two cyclones start to move westward and away from the equator. As the cyclones move into higher latitudes, the leading edge of the equatorial westerly winds retreats to the west and their intensity decreases. This is seen in figure 5.4*d* which contains the results at 10 days of simulation. During the entire simulation, the zero PV line remains undisturbed, indicating that there is no exchange of mass between the two hemispheres. The formation of a Rossby wave wake to the east of each cyclone is also evident of this simulation, producing the easterly winds just to the east of the equatorial westerlies at 10 days. The evolution of both the cyclone circulations and the equatorial westerly winds in the model is similar to the evolution of the cyclonic circulations and WWB associated with Supertyphoon Lola and Tropical Cyclone Namu discussed in section 5.1.1. Note that as the two cyclones move away from the equator, the tightening of the PV isolines is relaxed.

Figure 5.5 shows the results obtained when the same mass sink is displaced 2.5° away from the equator. This case evolves similarly to the previous case, with some exceptions.

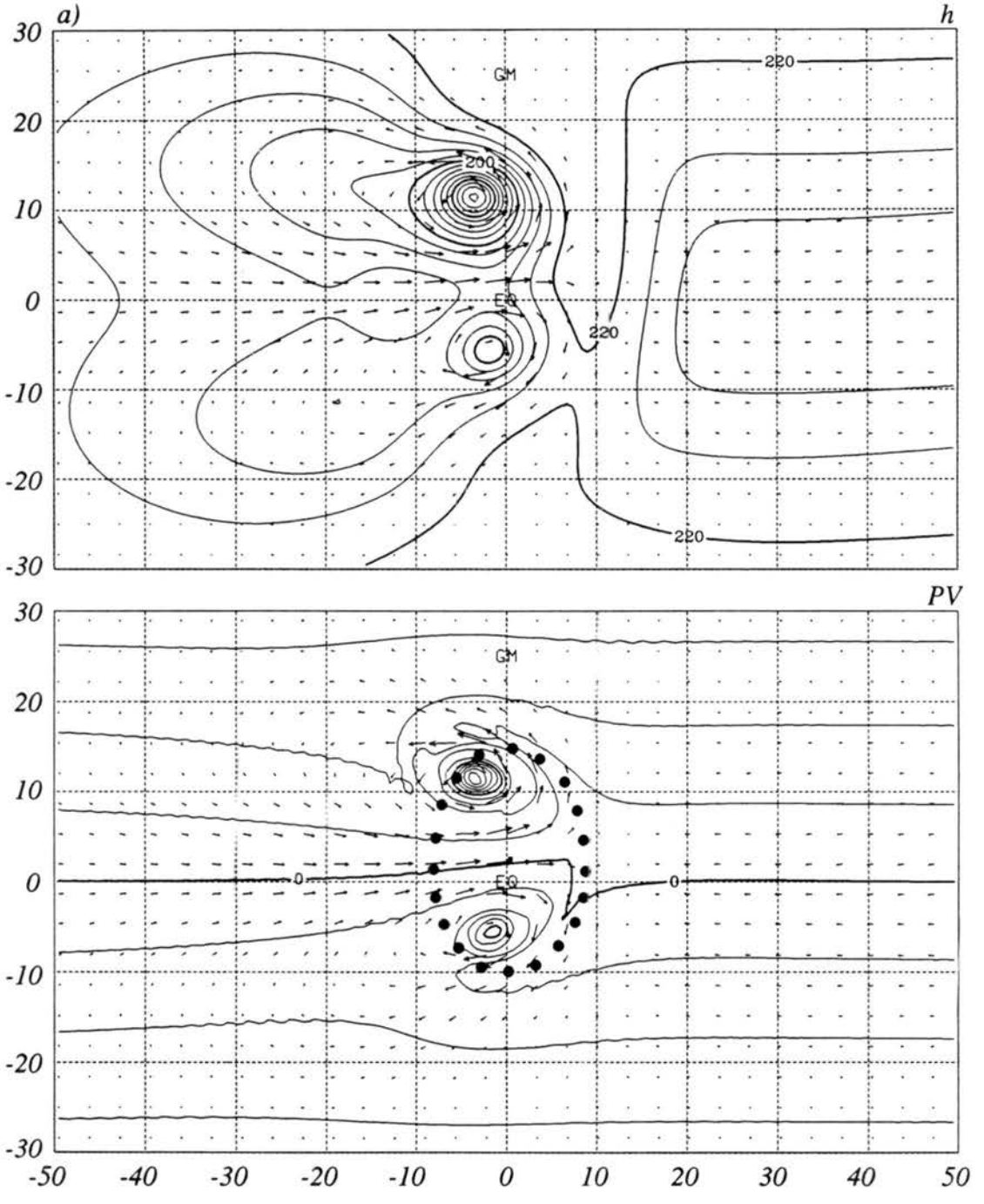

Figure 5.5: Evolution of PV ($s\,m^{-2}$), height (m) and wind (m/s) fields produced by a mass sink centered at $2.5°N$ with $c = 10°$, $d = 15°$, $\tau = 5$, $\overline{\Phi} = 2177.15\ m^2 s^{-2} day^{-1}$ and $\mid \partial\Phi/\partial t \mid = 864\ m^2 s^{-2} day^{-1}$. Heavy dots indicate the shape and location of the mass sink. *a)* Solution at day 5.

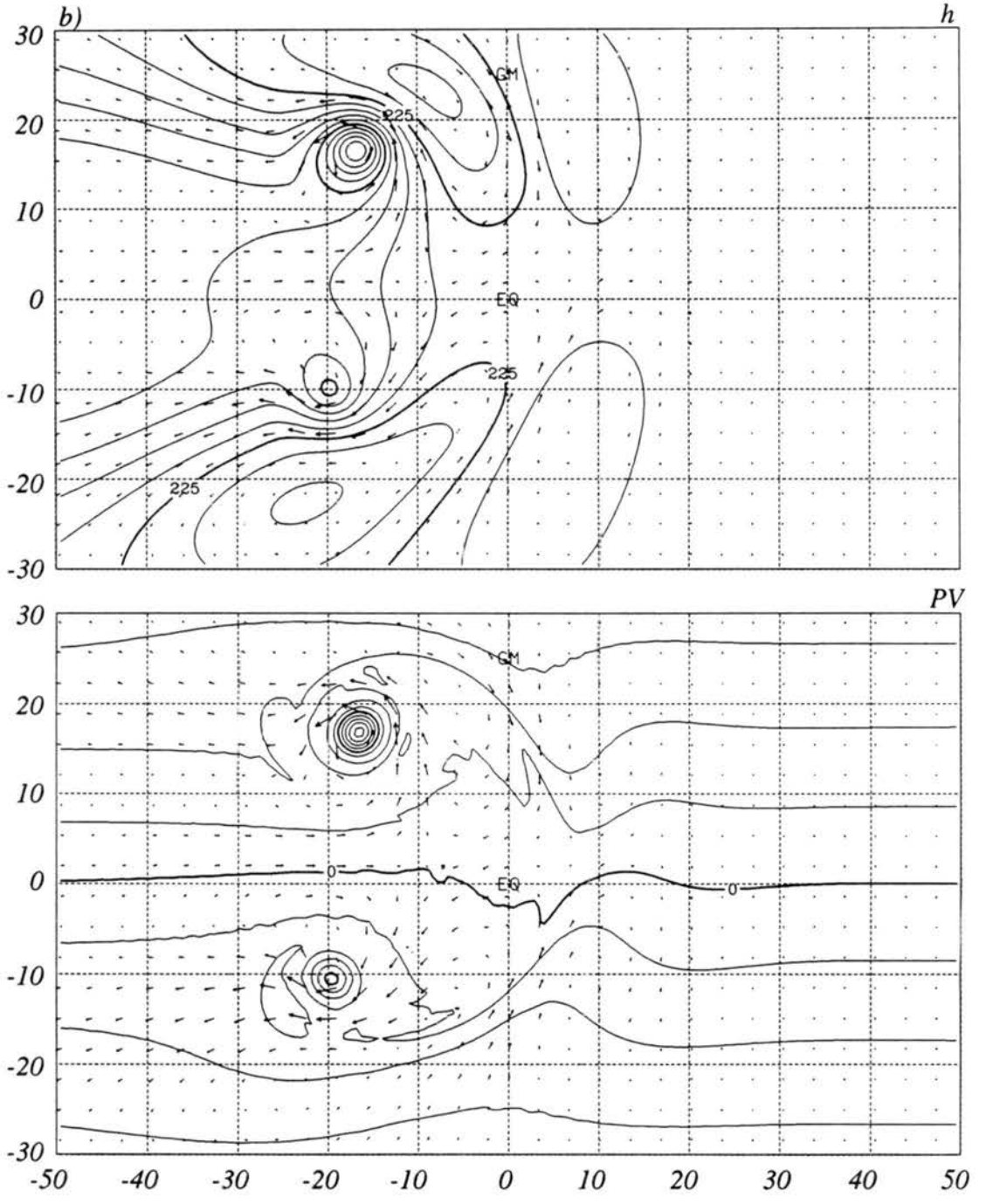

Figure 5.4: *b)* Idem at 10 days.

As expected, the results are not perfectly symmetric about the equator as in the previous experiment. When the mass sink is turned off, at 5 days, the NH cyclone is stronger than the SH one. This occurs because the NH cyclone forms farther away from the equator, where f is larger (again, this is due to the $-qQ/\Phi$ term in equation (2.14)). For the same reason, the NH cyclone in this simulation is also stronger than both vortices formed in the previous simulation. The maximum intensity of the equatorial westerly winds is again ~ 15 m/s, but its center is shifted northwards. As in the previous simulation, after the mass sink is turned off, the two cyclones begin their movement due west and away from the equator, causing the equatorial westerlies to weaken and retreat to the west. Moreover, in this case there is exchange of mass between the two hemispheres producing a region where inertial instability is possible near the equator. This simulation may help explain the observations of SCCs that produced two cyclonic circulations straddling the equator with only one of them resulting in a tropical cyclone. Obviously other factors such as unfavorable environmental genesis parameters may also have acted to hinder the formation of one of the tropical cyclones.

The foregoing experiments offer a qualitative picture of how twin tropical cyclone genesis might be initiated. In the next section, a series of experiments are performed in order to try to understand the existence of preferred regions for twin tropical cyclone genesis.

5.3 Preferred Regions for Twin Tropical Cyclone Formation

The existence of preferred regions for twin tropical cyclone formation is evident in the short climatology presented in section 5.1.2., where the vast majority of the observed twins formed in the W. Pacific, between $155°E$ and the dateline (in agreement with Keen, 1982). In this section, some experiments aimed at understanding the existence of preferred regions for the formation of twin cyclones are performed.

The two forthcoming experiments consist of the same mass sink used in the previous section, centered at the equator, but this time, moving eastward at speeds of 5 and 10 m/s. The mass sink is again turned off at $\tau = 5$ days. This is done to try to simulate the effect of the motion of the SCC on the formation of twin cyclones.

Figure 5.6 shows the PV, winds and height fields at 5 days for a meridionally elongated mass sink that travels eastward at a speed of 5 m/s. In this case, the mass sink moves $\sim 20°$ of longitude due east after 5 days. Regarding the equatorial westerlies, the main differences caused by the introduction of a moving mass sink are the larger area they cover, their extension further east and somewhat weaker wind speeds. As in the case that had a stationary mass sink centered at the equator, two vortices are produced here on either side of the equator. These vortices, however, are slightly weaker, form farther east and are initially more elongated. As time proceeds (not shown) these vortices tend to axisymmetrize and move due west and away from the equator.

The results at 5 days for the same mass sink moving due east at 10 m/s are shown in figure 5.7. This mass sink moves $\sim 40°$ of longitude due east by the time it is turned off at 5 days. In this case, an even larger area of westerlies is formed. The leading edge of the westerlies is at about $43°E$, compared to $25°E$ in the previous experiment and $\sim 10°E$ for the stationary mass sink. The westerlies produced in this experiment are even weaker than those obtained with the slower moving mass sink. A perhaps trivial, but interesting result in this experiment is the absence of formation of two well defined cyclones straddling the equator as before and the formation, instead, of two zonally elongated areas of relative maximum in the PV field. These areas are symmetric about the equator and have about 30° longitude in zonal extent. Moreover, the associated circulation patterns associated with these maximum PV areas resemble the monsoon trough circulation. This suggests an explanation for the observation of double ITCZs in the Western Central Pacific (Waliser and Gautier, 1993). The eastward movement of the leading edge of the westerlies with the mass sink is also in agreement with the observation by Nakazawa (1988) of westerlies accompanying SCC.

In the next experiment, the same meridionally elongated mass sink is initially stationary, then accelerates to a maximum speed of 5 m/s, and after several days, decelerates until it stops (see figure 5.9 for time variation of the speed of the mass sink). This experiment was devised to simulate the observed movement of SCCs and investigate the possible implications in the formation of tropical cyclone twins. Super cloud clusters are

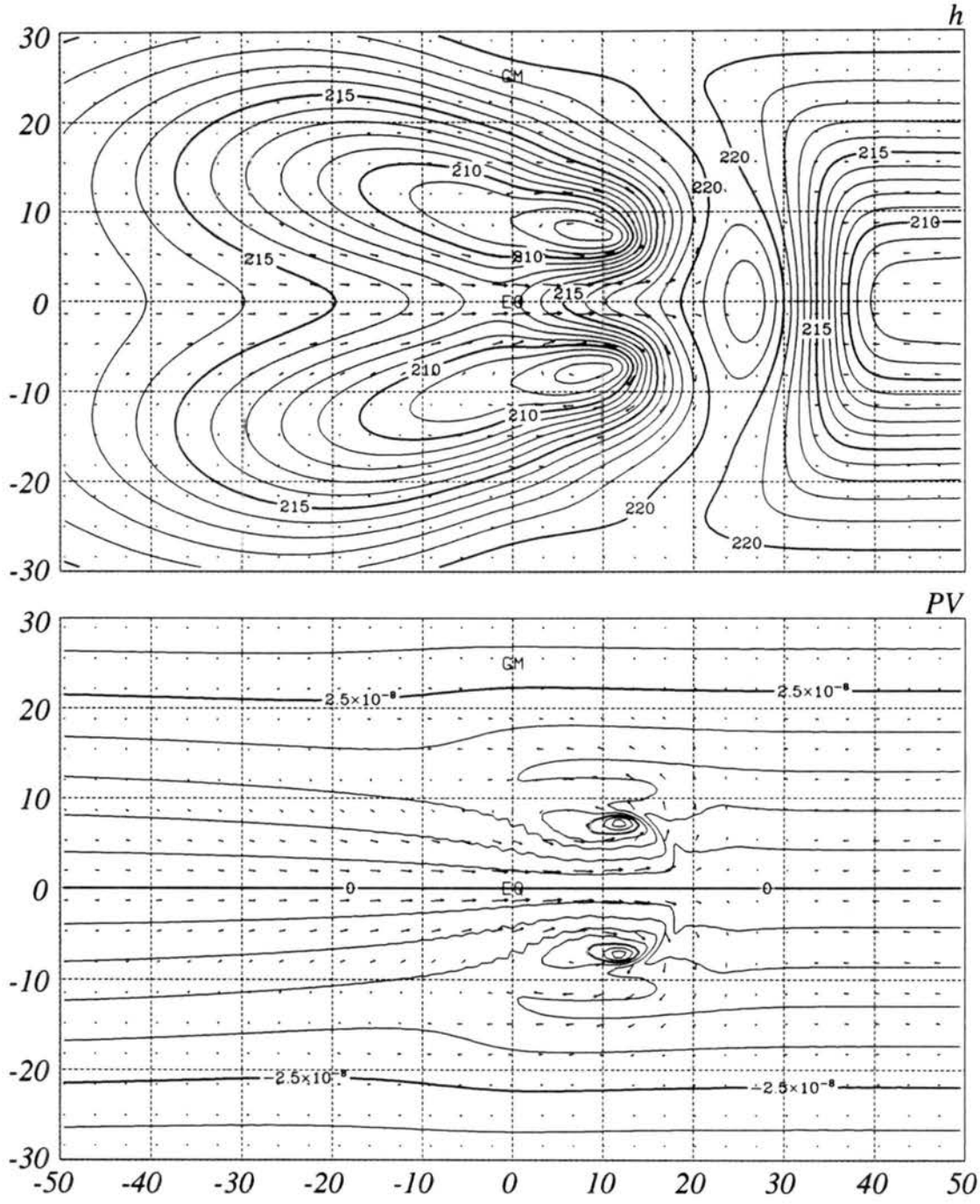

Figure 5.6: Height (m), wind (m/s) and PV ($s\,m^{-2}$) fields for a simulation in which a meridionally elongated mass sink centered at the equator is moving due east at 5 m/s. Results are for day 5 of the simulation.

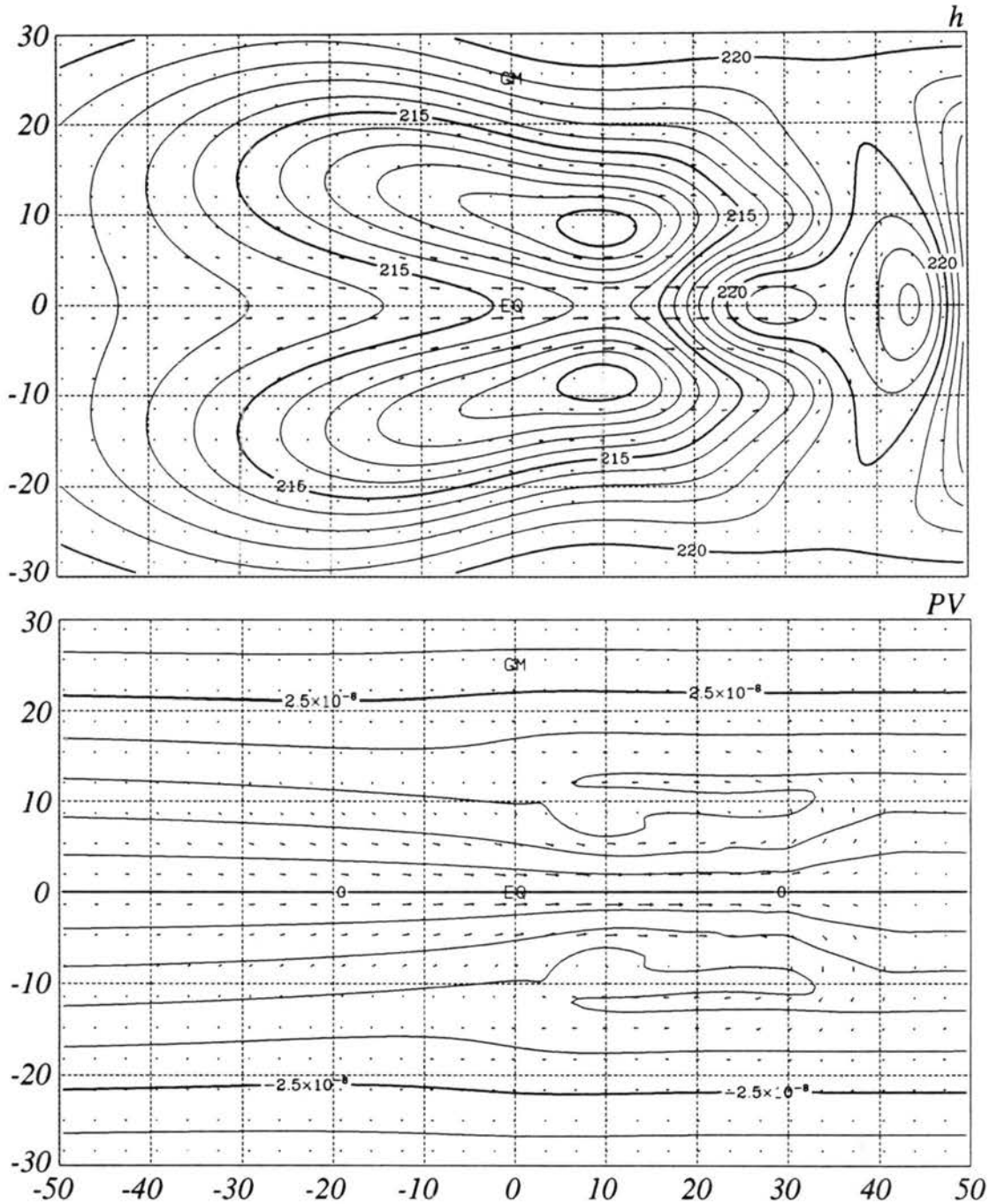

Figure 5.7: Height (m), wind (m/s) and PV ($s\,m^{-2}$) fields for a simulation in which a meridionally elongated mass sink centered at the equator is moving due east at 10 m/s. Results are for day 5 of the simulation.

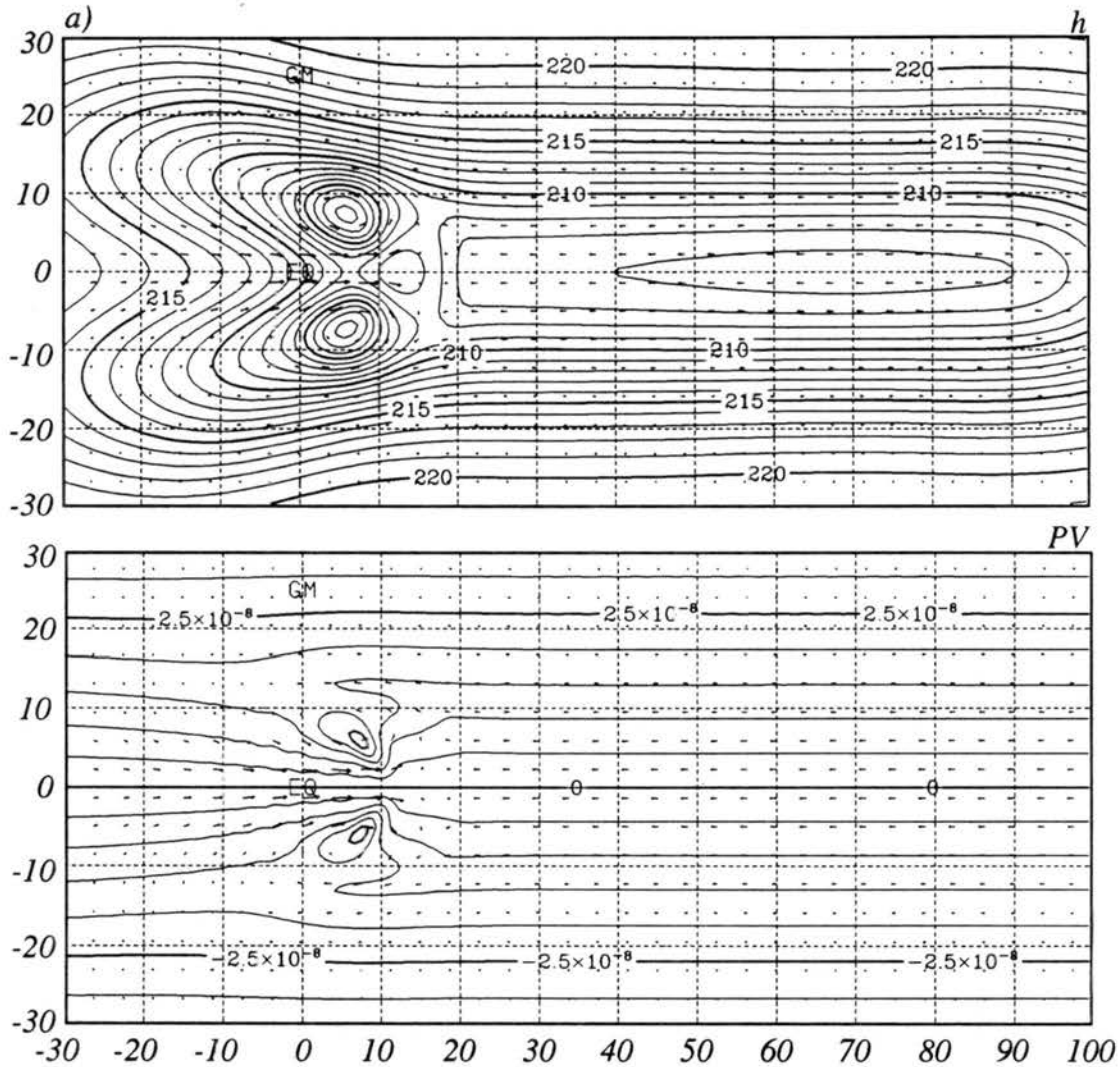

Figure 5.8: Height, wind and PV fields for a simulation in which a meridionally elongated mass sink centered at the equator is moving due east at variable speed. *a)* Height, PV and wind fields at 5 days.

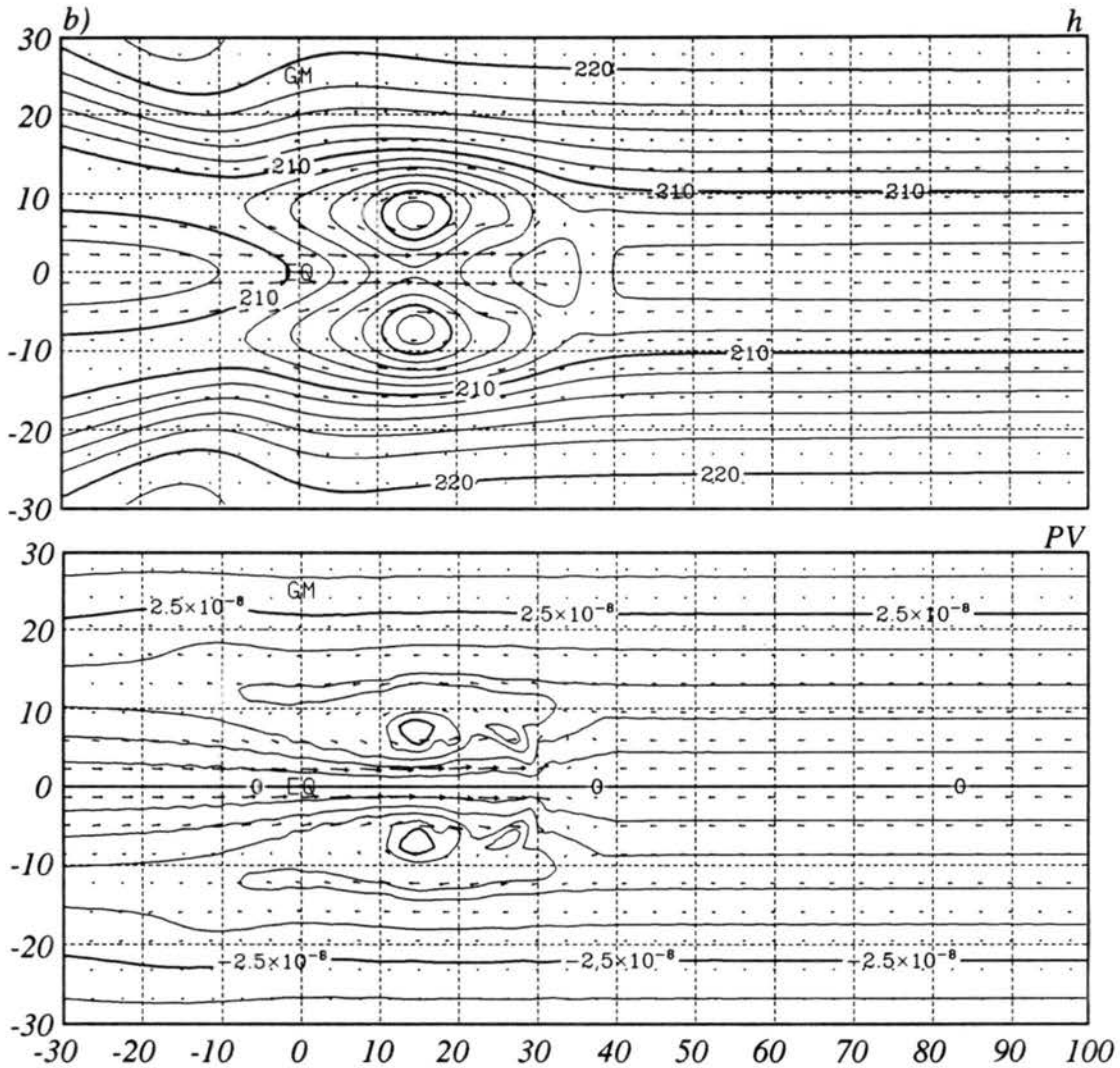

Figure 5.8: *b)* Same at 10 days.

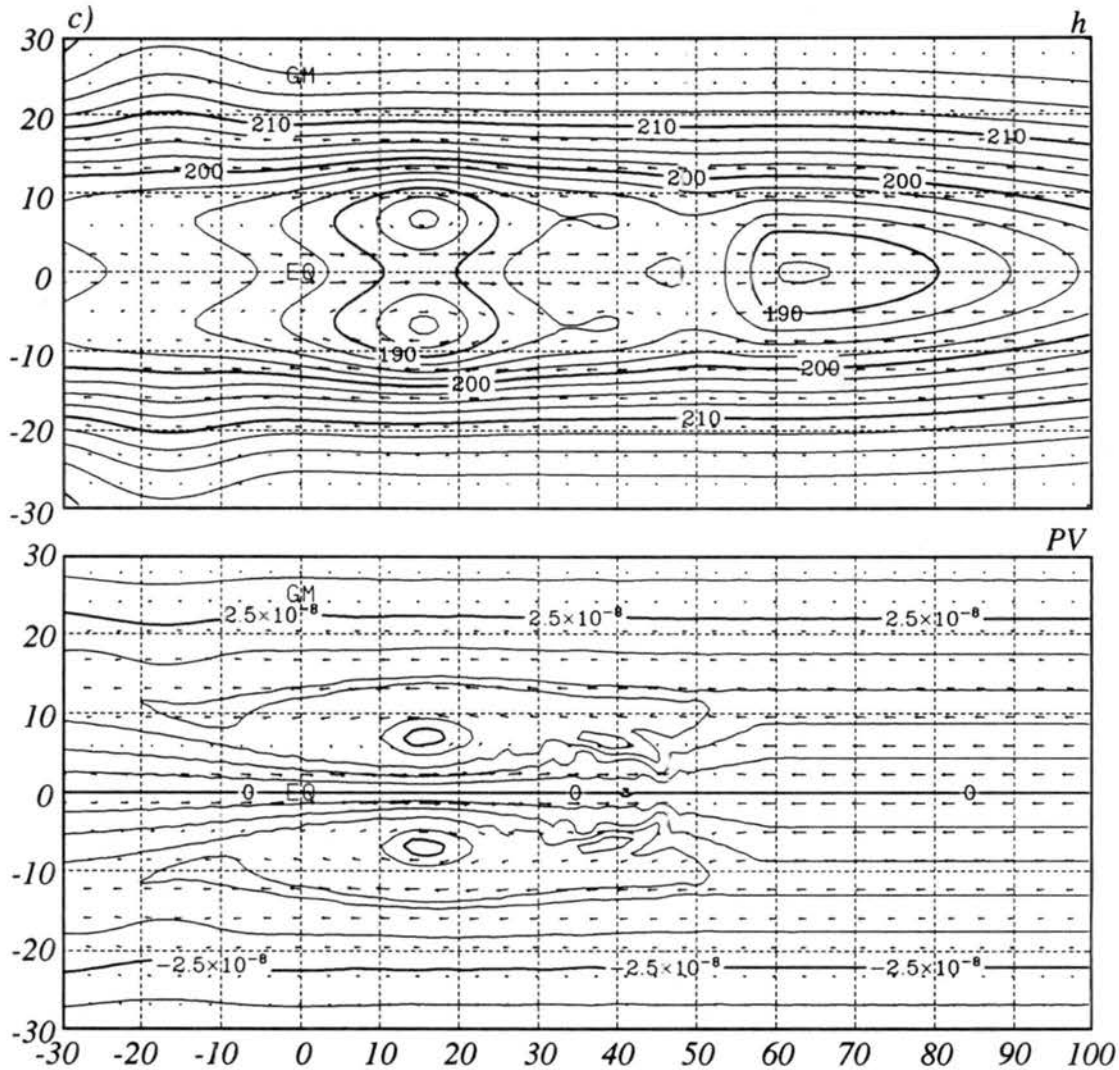

Figure 5.8: *c)* Same at 15 days.

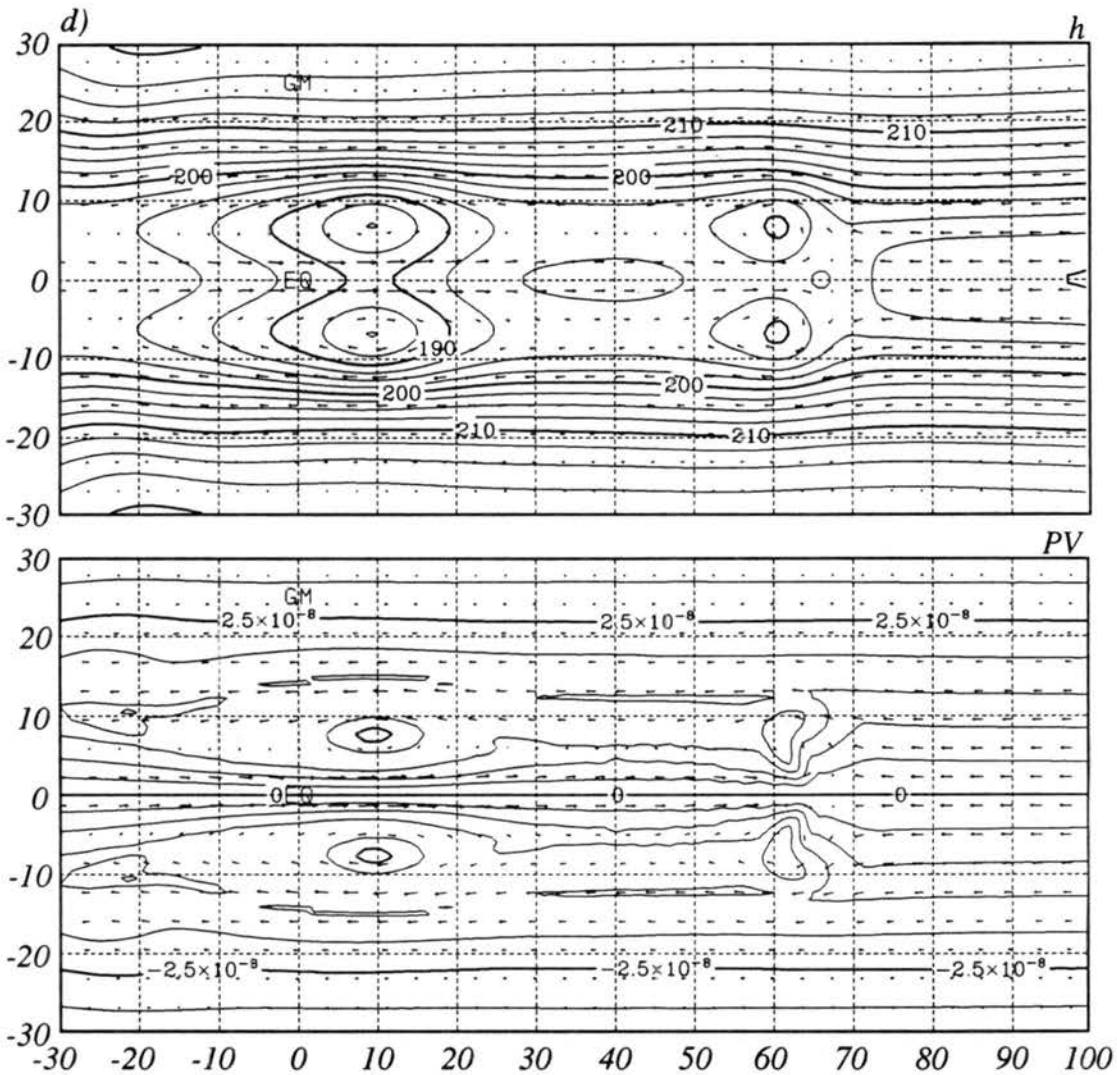

Figure 5.8: *d)* Same at 20 days.

observed to be stationary in their formation region in the Indian Ocean, then cross the Maritime Continent at speeds between 5-10 m/s, and then become stationary again near the dateline (Wang and Rui, 1990).

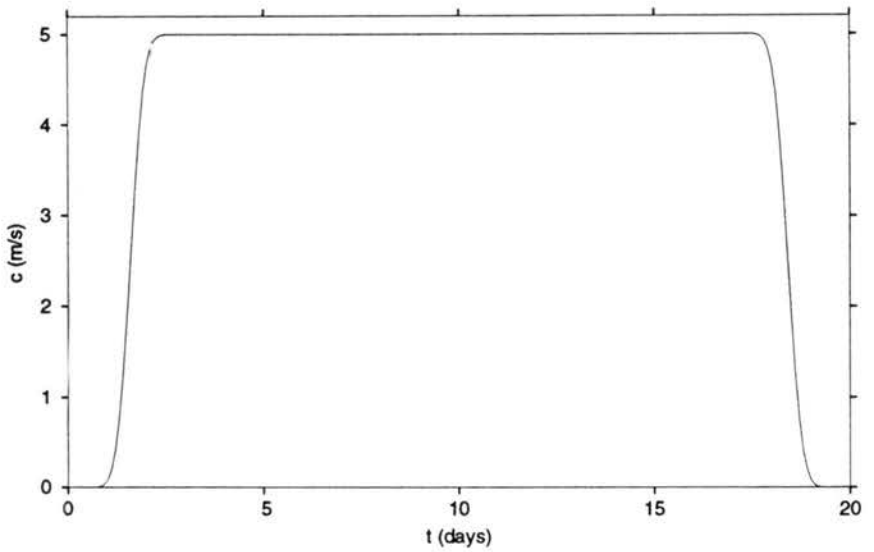

Figure 5.9: Time variation of the speed of the mass sink.

Figure 5.8 shows the resulting height, wind and PV fields for the experiment described above. The spatial truncation used is T126. experiment. After 5 days, two cyclones have formed straddling the equator with their accompanying equatorial westerlies to the west and easterlies to the east. On day 10, these two cyclones have stopped moving east with the mass sink and were left at $\sim 15°E$. The continuing movement of the mass sink is evidenced by two smaller and weaker new cyclonic areas that straddle the equator at $\sim 25°E$. It is also noticeable that the tightening of the PV gradient at the equator (which is effected by the mass sink) continues moving east. Five days later, on day 15, the mass sink continues on its eastward movement, leaving westerlies behind it in a large zonal stretch. These westerlies, however, are stronger in the region between the two initial cyclones that were left behind. The first cyclone pair (westernmost) now moves due west. The mass sink stops moving on day 20, but forcing continues until day 22. On day 22, a new pair of cyclones straddling the equator is present in the region where the mass sink stopped moving. This experiment suggests that the transience of the mass sink is necessary for its periodic shedding of vortices.

This last experiment may suggest a mechanism through which the same eastward moving SCC (which is the convective manifestation of the MJO) could be responsible for the formation of twin tropical cyclones in both the Indian Ocean and the W. Pacific.

5.4 Movement of Twin Tropical Cyclones

In this section, initial value experiments were performed to study the movement of tropical cyclone twins in a resting basic state. In the first experiment (SYM), two vortices of the same intensity ($\zeta_v = 2 \times 10^{-4}\, s^{-1}$) and radius of $2°$, are initially placed at $10°S$ and $10°N$ (see figure 4.4 for radial cross section of tangential wind and vorticity for these vortices). In the next experiment, the intensity of the southern vortex was decreased to half of the intensity of the northern vortex (ASYM). For comparison, another experiment was run with a single vortex centered at $10°N$ with intensity ($\zeta_v = 2 \times 10^{-4}\, s^{-1}$) and radius ($2°$). The trajectories followed by the vortices in three different experiments are shown in figure 5.10.

The trajectory followed by the single vortex in a resting basic state (VOR) is to the N-NW as dictated by the β-drift. The introduction of an identical vortex to the south of the equator causes both vortices to move initially poleward and eastward due to the equatorial westerlies between them. After two days, however, both vortices start moving westward and away form the equator. The interaction between the two vortices causes their trajectories to be longer and more zonal than the trajectory of the single vortex. Note that this effect of making the trajectory of the vortex longer and closer to the equator is also produced by a zonally symmetric PV strip located to the south of the NH vortex (see section 4.3). The tightening of the PV lines in the equatorial region between the vortices produces a PV anomaly near the equator that has the same sign as the PV anomaly that would be produced by the ITCZ, likely having similar effects upon the trajectory of the vortex. If the southern vortex is only half as strong as the northern one (ASYM), the two trajectories will no longer be symmetric about the equator. The southern vortex initially moves to the west and after three days starts moving W-NW. The trajectory of the northern vortex is closer to the trajectory VOR Experiments with increasingly larger

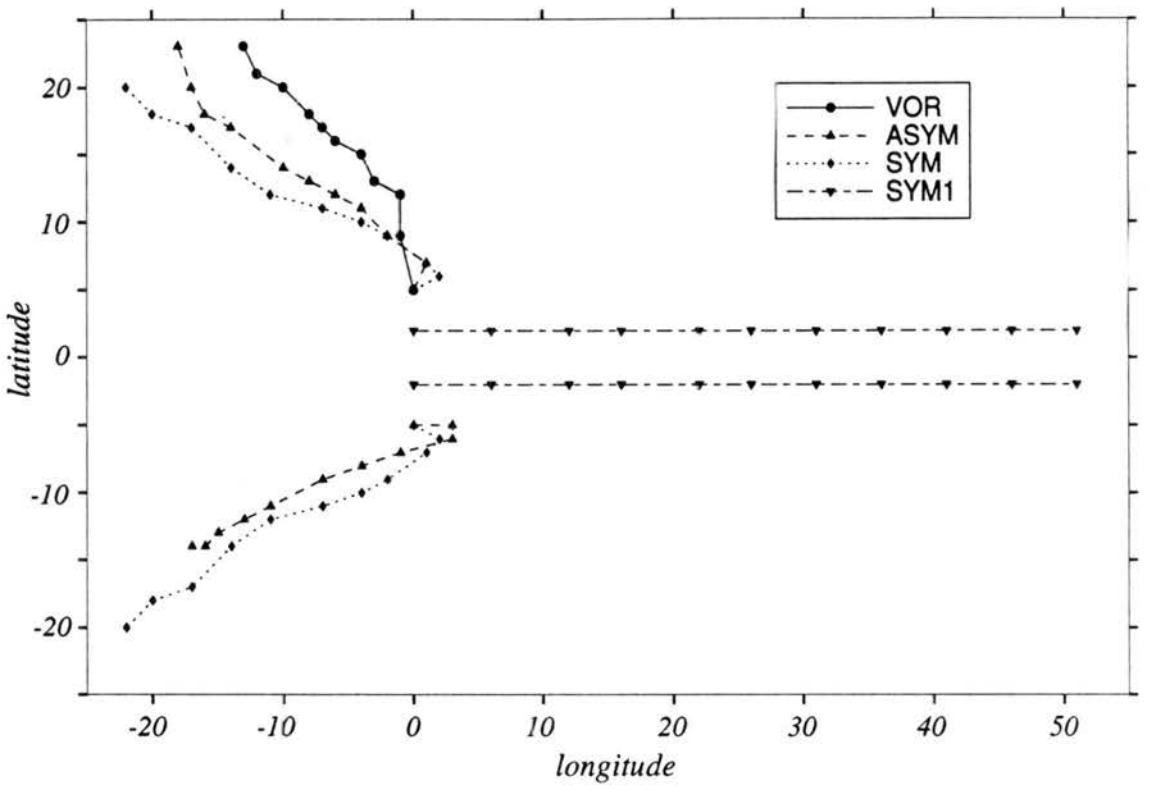

Figure 5.10: Trajectories followed by twin vortices of the same intensity (SYM) and different intensities (ASYM) initially centered at $10°S$ and $10°N$. In the symmetric (SYM) case, the two vortices have $\zeta_v = 2 \times 10^{-4}\, s^{-1}$ and radius $2°$. In the asymmetric case (ASYM) the northern vortex has the same characteristics as the ones in SYM, and is twice as intense as the southern vortex. The trajectory followed by a single vortex in a quiescent environment is also shown (VOR) for comparison. Symbols denote vortex positions every 24 hours.

distances between the two vortices show that their influence on each other's trajectories decreases with distance until they move independently as dictated by pure β-drift. On the other hand, if the two vortices are initially placed close enough together (SYM1), they will move due east instead because of the steering flow influence of the circulation of each vortex on the other.

Chapter 6

SUMMARY AND CONCLUSIONS

A shallow water model on the sphere was used to study some aspects of the dynamics of of the very early stages of tropical cyclone genesis, namely, the formation of the synoptic scale horizontal circulation associated with tropical disturbances. The shallow water model is a very useful simple tool to study tropical atmospheric phenomena that are dominated by horizontal advection of vorticity, divergence and barotropic instability. Two such tropical phenomena addressed here are the ITCZ breakdown and the formation of the tropical disturbances that lead to tropical cyclone twins in the W. Pacific and Indian Oceans.

Easterly waves are an important example of tropical disturbances which have been observed in W. Africa and in the Atlantic Ocean (Carlson, 1969; Burpee, 1972; Reed *et al.*, 1977; Chen and Ogura, 1982), Western and Central Pacific (Reed and Recker, 1971; Yanai, 1961), South China Sea and India (Saha *et al.*, 1981) and Eastern Pacific Ocean (Tai and Ogura, 1987). Approximately half of the Atlantic hurricanes form within African and Atlantic easterly waves (Frank, 1987). A consensus seems to exist that these waves result from combined barotropic and baroclinic instability of the mean zonal flow (Burpee, 1972; Norquist *et al.*, 1977; Rennick, 1976; Simmons, 1977; Mass, 1977; Kuo, 1978; Kwon, 1989). The origin of the unstable mean flow has been explained in two different ways. In the African region the unstable mean flow is believed to exist due to the surface meridional temperature gradient between the warm Saharan air and the colder air over the Guinea Gulf (see, for instance, Burpee, 1972). However the dependence on a surface characteristic that is particular to the African region, makes this theory unsuitable to explain the existence of easterly waves in the Pacific or Indian oceans, unless African easterly waves propagate into these regions (as suggested in Simpson *et al.*, 1969; Frank,

1976; Frank, 1987; Avila and Clark, 1989, among others). The second explanation for the existence of the unstable mean flow involves the convection in the ITCZ itself (as suggested by Hack *et al.*, 1989; Schubert *et al.* 1991, 1992; Guinn, 1992). In the lower levels, ITCZ convection produces a positive (negative) PV anomaly in the NH (SH). This convection generated PV anomaly has a reversal in the meridional PV gradient on its poleward side and may become unstable to small flow perturbations (Rayleigh, 1945). The ITCZ is then hypothesized to undulate under the effect of combined barotropic and baroclinic instability and to break down into a series of tropical disturbances. This mechanism is called ITCZ breakdown and an example of it is shown in figure 1.3. The ITCZ breakdown is then a plausible mechanism to explain the presence of easterly waves independently in each region where they are observed. In the African region, however, where the mean flow shear is stronger (see, for instance, Tai and Ogura, 1987) both of the above mechanisms may be cooperating in the formation of the unstable mean flow.

Given that the ITCZ breakdown is caused by an instability of the mean flow which was studied here with a shallow water model, the theory of stability for barotropic flows was reviewed in chapter 3. A linear normal mode stability analysis for zonally symmetric vorticity strips on the rotating sphere was then performed and the results obtained were found to be in agreement with results previously obtained on the f and β planes, namely that: *1)* the growth rate of the most unstable mode increases as the horizontal shear increases (by either increasing the vorticity of the strip or decreasing its width); *2)* the wavelength of the most unstable mode increases as the vorticity of the strip increases; and *3)* the wavelength of the most unstable mode increases as the width of the strip increases. A couple of exceptions were that on the rotating sphere wavenumber one perturbations did become unstable and the ratio between wavelength and width of the modes decreases with increasing width of the strip. The wave-activity conservation relations for a shallow water flow on the sphere were derived. The usefulness of these relations is limited by the fact that their flux does not provide a measure of the interactions between the mean flow and the perturbations. Application of the derived relationships is left for future work.

Shallow water simulations of the ITCZ breakdown were presented in chapter 4. In the model, initially imposed regions of high PV or mass sinks are used to simulate the

presence of the ITCZ and tropical cyclones. The first simulation presented was an initial value experiment that showed the breakdown of a zonally symmetric PV strip. The results obtained were in agreement with those of the linear normal mode stability analysis performed in chapter 3. Additional initial value experiments in which a circular PV patch was introduced in the vicinity of the above mentioned PV strip were calculated. The PV strip caused the vortex to deviate from its simple β-effect induced motion by both introducing a steering flow and changing the background meridional vorticity gradient (Evans *et al.*, 1991). As expected, the vortex followed a longer and more zonal trajectory towards the WNW. Interestingly, short Rossby wave dispersion to the east of the vortex, produced perturbations on the ITCZ that caused it to break down into several vortices. This was suggested as an alternative mechanism to explain the observation that new tropical cyclones tend to form to the east of existing ones in both the Western (Frank, 1982) and Eastern Pacific. Another possible explanation is simply the formation of a cyclone to the east of the vortex by the short Rossby wave dispersion process (Holland, 1994). The efficiency of this process in producing a vortex, however, was shown to be decreased in the presence of a positive PV strip to the south of the vortex.

In the next set of experiments, localized forcings were introduced as more realistic proxies for a zonally asymmetric ITCZ. In the first case, the forcing was an elliptical mass sink of dimensions and intensity comparable to those of the ITCZ. After a few days, the forcing produced a positive PV anomaly whose associated wind field resembles the tropical monsoon circulation. To the north of the PV anomaly, the meridional PV gradient is reversed, making the flow barotropically unstable to small perturbations. Barotropic instability then occurs and the localized PV strip breaks down into a series of vortices whose dimensions and number depend on the dimensions of the mass sink. The vortices in these experiments did not form simultaneously, but sequentially, from west to east. Moreover, in these model experiments the resulting cyclonic vortices formed on the northern side of the mass sink. This may in part explain the observation by Gray (1968) that approximately 80% of the total global number of tropical cyclones form within or just to the north os the ITCZ.

When the localized mass sink is made wider on its easternmost side, two types of evolution are observed. First, if the distortion from ellipticity is small, the mass sink again produces a PV anomaly that breaks down into a number of vortices. Increasing the ratio between the widths of the eastern and western sides of the mass sink, causes the resulting PV strip to axisymmetrize into only one vortex, rather than breaking down into a series of vortices. An example of the latter type of evolution is the formation of Hurricane Aletta in May of 1978 (see Fig. 4.11).

A brief analyses of tropical cyclone genesis in the E. Pacific during 1980 to 1993 showed a tendency for these storms to cluster in time. This time clustering has previously been observed by Zehnder (1991) and globally by Gray (1979). Liebmann *et al.* (1993) suggests that the Madden-Julian Oscillation might be responsible for the time clustering of storms in the West Pacific and Indian Oceans. Zehnder (1991) proposes that the observed time clustering in the E. Pacific is due to the interaction of a quasi-persistant favorable large scale flow with the Sierra Madre Mountains in Central America. In this study, yet another mechanism is proposed to be responsible for the observed time clustering of tropical cyclones, namely, the ITCZ breakdown. Time clusters were then defined as groups of storms in which each tropical cyclone is separated from the next or previous storm by no more than 4 days. Approximately 40% of the tropical cyclones in the E. Pacific during that 14 year interval formed in these time clusters. Moreover, in most of the observed clusters, the easternmost tropical cyclones were the first to form. These observations of time clustering, spatial distance between storms and their sequential formation from east to west all point to the possibility that ITCZ breakdown may have played an important role in their formation.

The formation of twin tropical cyclones in the W. Pacific and Indian Oceans was addressed in chapter 5. A short climatology of twin tropical cyclones during 1983 to 1993 revealed that W. Pacific twin tropical cyclones are observed about once every year preferrably between 155°E and the dateline. However, since four of the cases observed occurred in 1986, that frequency of formation comes down to about one case every one and a half years.

A series of model experiments were then performed to study the formation and movement of the tropical disturbances that lead to the formation of twin tropical cyclones. In this case, a meridionally elongated mass sink was used to simulate the presence of a super cloud cluster in the tropics. After a few model days, this meridionally elongated mass sink centered at the equator produces two cyclonic circulations straddling the equator. These two cyclonic circulations then move poleward and westward causing the equatorial westerly winds between them to weaken and retreat to the west. The evolution of the circulation produced by the model in this case is in agreement with that shown in ECMWF 850 mb wind analyses during the formation of a set of twin tropical cyclones in the West Pacific in May of 1986 (ECMWF, 1987). When the same mass sink is centered off the equator, the two cyclonic vortices straddling the equator have different intensity.

Super cloud clusters typically form in the Indian Ocean, then move across the Maritime Continent at speeds between 5 and 15 m/s and finally stall and dissipate near the dateline (Wang and Rui, 1990; Weickman and Khalsa, 1990). This inspired some model experiments that investigated the effects of the movement of the mass sink. Experiments run with a mass sink that moved at 5 and 10 m/s showed that the former produced two vortices straddling the equator, while the latter produced two elongated regions of cyclonic vorticity on either side of the equator. The formation of the two elongated regions of cyclonic vorticity straddling the equator when the mass sink is moving at 10 m/s was proposed to be associated with the occasional existence of double ITCZs in the W. Pacific.

One last experiment was shown in which the mass sink simulated the previously described movement of the SCC accross from the Indian ocean to the dateline. In this experiment, the mass sink was initially stationary, then was accelerated to a speed of 5 m/s and then finally stopped several days later. This mass sink produced two sets of twin tropical cyclones, the first one in the region where it was initially turned on and a second one in the region it stopped moving. It was then hypothesized that SCCs associated with the MJO produce twin tropical cyclones in the two regions where they are stationary, namely their region of formation in the Indian Ocean and their decay region near the date line. This is supported by some observations of twin formation in the Indian

Ocean, followed by twin formation near the dateline about 10 days later (such as the two sets of twins in May 1986 listed in table 5.1). The movement of the SCCs then offers an explanation for the existence of preferred regions for the formation of twin tropical cyclones.

The movement of twin tropical cyclones was studied in a series of initial value experiments in which two circular patches of vorticity were introduced on opposite sides of the equator. It was observed that the interaction between the two vortices causes their trajectories to be longer and more zonal towards the WNW than the β-drift trajectory of the single vortex. When the two vortices are close enough together, they move due east instead because of the steering flow influence of the circulation of each vortex on the other.

Both the ITCZ breakdown and the formation of the disturbances that lead to twin tropical cyclones are dominated by balanced dynamics and should be reproduced within the framework of a balanced model. The influences of the Kelvin waves, however, will not be present in most balanced models.

The shallow water model appears to capture some important dynamical aspects of the very early stages of tropical cyclone genesis, namely, the formation of tropical cyclone disturbances in the special cases when the ITCZ breaks down and the formation of twin tropical cyclones in the W. Pacific and Indian Oceans. Baroclinic effects must certainly play an important role in the formation of tropical disturbances, but they were not addressed here. Finally, the reproduction of all the processes that ultimately lead to the formation of a full fledged tropical cyclone clearly requires more physics than is available in this simple shallow water model.

A number of suggestions for future work can be made in both modeling and observational contexts, some of which are mentioned below.

The inclusion of friction effects would be important to more realistically assess the growth rates of the instabilities studied as well as the strength of the circulations produced. However, it should be kept in mind that the time scales and intensity of the circulations produced in the model are directly proportional to the intensity of either the mass sink

(in the forced experiments) or the initial perturbation (in the initial value experiments). This problem needs more attention. The inclusion of vertical structure is important to assess the importance of baroclinic effects in the formation of the tropical disturbances. Long range experiments with a more realistic model could be used to study the periodicity of the ITCZ breakdown. Investigation of the usefulness of the wave-activity concept in barotropic tropical dynamics is also left for future work.

Finally, an improvement of the observational network in the regions where tropical cyclogenesis takes place is crucial to the better understanding of its causes. Observational work is needed to verify the occurrence in nature of the processes studied here.

REFERENCES

Agee, E. M., 1972: Note on ITCZ wave disturbances and formation of Tropical Storm Anna. *Mon. Wea. Rev.*, **100**, 733–737.

Andrews, D. G., 1987: On the interpretation of the Eliassen-Palm flux divergence. *Quart. J. Roy. Meteor. Soc.*, **113**, 323–338.

———, and M. E. McIntyre, 1976: Planetary waves in horizontal and vertical shear: the generalized Eliassen-Palm relation and the mean zonal acceleration. *J. Atmos. Sci.*, **33**, 2031–2048.

———, and ———, 1978: An exact theory of nonlinear waves on a Lagrangian-mean flow. *J. Fluid Mech.*, **89**, 609–646.

Avila, L. A. and G. B. Clark, 1989: Atlantic tropical systems of 1988. *Mon. Wea. Rev.*, **117**, 2260–2265.

Bartels, D. L., and R. A. Maddox, 1991: Midlevel cyclonic vortices generated by mesoscale convective systems. *Mon. Wea. Rev.*, **119**, 104–118.

Bosart, L., and J. Bartlo, 1991: Tropical storm formation in a baroclinic environment. *Mon. Wea. Rev.*, **119**, 1979–2013.

Brandes, E. A., 1990: Evolution and structure of the 6-7 May 1985 mesoscale convective system and associated vortex. *Mon. Wea. Rev.*, **118**, 109–127.

Briegel, L. M., 1993: An observational study of tropical cyclogenesis in the Western Pacific Ocean. *Preprints of the 20th Conference on Hurricanes and Tropical Meteorology*, Amer. Meteor. Soc., 397–400.

Burpee, R. W., 1972: The origin and structure of easterly waves in the lower troposphere of North Africa. *J. Atmos. Sci.*, **29**, 77–90.

Carlson T. N., 1969a: Synoptic histories of three African disturbances that developed into Atlantic hurricanes. *Mon. Wea. Rev.*, **97**, 256–276.

———, 1969b: Some remarks on African disturbances and their progress over the tropical Atlantic. *Mon. Wea. Rev.*, **97**, 716–726.

Case, K. M., 1960: Stability of inviscid plane Couette flow. *Phys. Fluids*, **3**, 143–148.

Challa, M., and R. L. Pfeffer, 1990: Formation of Atlantic hurricanes from cloud clusters and depressions. *J. Atmos. Sci.*, **47**, 909–927.

Chan, J. C. L., and R. T. Williams, 1987: Analytical and numerical studies of the beta-effect in tropical cyclone motion. Part I: zero mean flow. *J. Atmos. Sci.*, **44**, 1257–1265.

Chang, C., 1970: Westward propagating cloud patterns in the tropical Pacific as seen from time-composite satellite photographs. *J. Atmos. Sci.*, **27**, 133–138.

Charney, J. G., 1963: A note on large-scale motions in the tropics. *J. Atmos. Sci.*, **20**, 607–609.

———, and A. Eliassen, 1964: On the growth of the hurricane deppression. *J. Atmos. Sci.*, **21**, 68–75.

Chen, S. S., 1993: Equatorial westerly wind bursts and double cyclones. *Preprints of the 20th Conference on Hurricanes and Tropical Meteorology*, Amer. Meteor. Soc., 615–617.

———, and W. M. Frank, 1993: A numerical study of convective mesovortices. Part I: evolution and dynamics. *J. Atmos. Sci.*, **50**, 2401–2426.

Chen, W. -L., and Y. Ogura, 1982: Modulation of convective activity by large-scale flow patterns observed in GATE. *J. Atmos. Sci.*, **44**, 1260–1279.

Cotton, W. R., M.-S. Lin, R. L. McAnelly, and C. J. Tremback, 1989: A composite model of mesoscale convective complexes. *Mon. Wea. Rev.*, **117**, 765–783.

Drazin, P. G., and W. H. Reid, 1981: *Hydrodynamic instability*, Cambridge University Press, 527 pp. [ISBN 0-521-28980-7].

Dritschel, D. G., 1986: The nonlinear evolution of rotating configurations of uniform vorticity. *J. Fluid Mech.*, **172**, 157–182.

———, 1989: On the stabilization of a two-dimensional vortex strip by adverse shear. *J. Fluid Mech.*, **206**, 193–221.

———, and L. M. Polvani, 1992: The roll-up of vorticity strips on the surface of a sphere. *J. Fluid Mech.*, **234**, 47–69.

Edmon, H. J., Jr, B. J. Hoskins, and M. E. McIntyre, 1980: Eliassen-Palm cross sections for the troposphere. *J. Atmos. Sci.*, **37**, 2600–2616.

Eliassen, A., 1983: The Charney-Stern theorem on barotropic-baroclinic instability. *PA-GEOPH*, bf 121, 563–572.

Elsberry, R. L., 1987: Tropical cyclone motion. *A Global View of Tropical Cyclones*, R. L. Elsberry, W. M. Frank, G. J. Holland, J. D. Jarrel, and R. L. Southern, Eds., ONR Marine Meteorology Program, 185 pp.

Emanuel, K. A., 1986: An air-sea interaction theory for tropical cyclones. Part I: Steady-state maintenance. *J. Atmos. Sci.*, **43**, 585–604.

———, N. Renno, L. R. Schade, M. Bister, M. Morgan, D. J. Raymond, and R. Rotunno, 1993: Tropical cyclogenesis over the Eastern North Pacific: some results of TEXMEX. *Preprints of the 20th Conference on Hurricanes and Tropical Meteorology*, Amer. Meteor. Soc., 110–113.

European Centre for Medium Range Weather Forecasts (ECMWF), 1987: *Daily Global Analyses*, April-June 1986. Reading, Berkshire RG29AX, England.

Evans, J. L., G. J. Holland, and R. L. Elsberry, 1991: Interactions between a barotropic vortex and an idealized subtropical ridge. Part I: Vortex motion. *J. Atmos. Sci.*, **48**, 301–314.

Farrel, B. F., 1982: The initial growth of disturbances in a baroclinic flow. *J. Atmos. Sci.*, **39**, 1663–1686.

Frank, N. L., 1969a: Atlantic tropical systems of 1969. *Mon. Wea. Rev.*, **98**, 306–314.

———, 1969b: The "inverted V" cloud pattern - an easterly wave?. *Mon. Wea. Rev.*, **97**, 130–140.

———, 1976: Atlantic tropical systems of 1975. *Mon. Wea. Rev.*, **104**, 466–474.

Frank, W. M., 1982: Large-scale characteristics of tropical cyclones. *Mon. Wea. Rev.*, **110**, 572–586.

———, 1987: Tropical cyclone formation. *A Global View of Tropical Cyclones*, R. L. Elsberry, W. M. Frank, G. J. Holland, J. D. Jarrel, and R. L. Southern, Eds., ONR Marine Meteorology Program, 185 pp.

Fulton, S. R., and W. H. Schubert, 1985: Vertical normal mode transforms: theory and application. *J. Atmos. Sci.*, **113**, 647–658.

Gerrish, H. P., and M. Mayfield, 1989: Eastern North Pacific tropical cyclones of 1988. *Mon. Wea. Rev.*, **117**, 2266–2277.

Gill, A. E., 1980: Some simple solutions for heat-induced tropical circulation. *Quart. J. Roy. Meteor. Soc.*, **106**, 447–462.

Gray, W. M., 1968: Global view of the origin of tropical disturbances and storms. *Mon. Wea. Rev.*, **96**, 669–700.

———, 1975: Tropical cyclone genesis. Colorado State University, Dept. of Atmospheric Science, Paper No. 234, 121 pp.

———, 1979: Hurricanes: their formation, structure and likely role in the tropical circulation. *Supplement to Meteorology Over the Tropical Oceans*, D. B. Shaw, Ed., Roy. Meteor. Soc., 155-218.

———, 1989: Background information of talk by William M. Gray to the eleventh annual national hurricane conference, Miami, Florida. Colorado State University, 41 pp.

Guinn, T. A., 1992: A dynamic theory for hurricane spiral bands. PhD Dissertation, Colorado State University, 178 pp.

———, and W. H. Schubert, 1993: Hurricane spiral bands. *J. Atmos. Sci.*, **50**, 3380–3403.

Gunther, E. B., 1979: Eastern North Pacific tropical cyclones of 1978. *Mon. Wea. Rev.*, **107**, 911–927.

Hack, J. J., and R. Jakob, 1992: Description of a global shallow water model based on the transform method. *NCAR Tech. Note (NCAR/TN-343+STR)*, Climate and Global Dynamics Division, NCAR, Boulder, Colo., 39 pp.

———, and W. H. Schubert, 1986: Nonlinear response of atmospheric vortices to heating by organized cumulus convection. *J. Atmos. Sci.*, **43**, 1559–1573.

———, ———, D. E. Stevens, and H. Kuo, 1989: Response of the Hadley circulation to convective forcing in the ITCZ. *J. Atmos. Sci.*, **46**, 2957–2973.

Haltiner, G. J., and R. T. Williams, 1980: Numerical prediction and dynamic meteorology. John Wiley & Sons, 477 pp. [ISBN 0-471-05971-4].

Hartten, L. M., 1993: The seasonal and intraseasonal variability of near-surface westerly winds over the Western Equatorial Pacific, 1980-1989. *Preprints of the 20th Conference on Hurricanes and Tropical Meteorology*, Amer. Meteor. Soc., 9–12.

Haynes, P. H., 1988: Forced, dissipative, generalizations of finite amplitude wave-activity conservation relations for zonal and non-zonal basic flows. *J. Atmos. Sci.*, **45**, 2352–2362.

Hertenstein, R. F. A., and W. H. Schubert, 1991: Potential vorticity anomalies associated with squall lines. *J. Atmos. Sci.*, **119**, 1663–1672.

Holland, G. J., 1994: Scale interaction in the Western Pacific monsoon. Submitted to *Meteor. Atmos. Phys.*

Holton, J. R., 1992: *An introduction to dynamic meteorology*. Academic Press, 511pp. [ISBN 0-12-354355-X].

Hoskins, B. J., A. J. Simmons, and D. G. Andrews, 1977: Energy dispersion in a barotropic atmosphere. *Quart. J. Roy. Meteor. Soc.*, **103**, 553–567.

———, M. E. McIntyre, and A. W. Robertson, 1985: On the use and significance of isentropic potential vorticity maps. *Quart. J. Roy. Meteor. Soc.*, **111**, 877–946.

———, H. H. Hsu, I. N. James, M. Matsutani, P. D. Sardeshmukh, and G. H. White, 1989: Diagnostics of the global atmospheric circulation, based on ECMWF analyses 1979-1989. *World Climate Research Programme - 27*, WMO/TD-No. 326.

———, 1991: Towards a PV-θ view of the general circulation. *Tellus*, **43AB**, 27–35.

Houze, R. A., 1989: Observed structure of mesoscale convective systems and implications for large-scale heating. *Quart. J. Roy. Meteor. Soc.*, **115**, 425–461.

Jakob, R. J., J. J. Hack, and D. L. Williamson, 1993: Solutions to the shallow water test set using the spectral transform method. *NCAR Tech. Note (NCAR/TN-388+STR)*, Climate and Global Dynamics Division, NCAR, Boulder, Colo., 82 pp.

Japanese Meteorological Satellite Center (JMSC), 1986: *Monthly Report.* Tokyo, Japan. [ISSN 0387-4028].

Johnson, R. H., and D. L. Bartels, 1992: Circulations associated with a mature-to-decaying mesoscale convective system. Part II: Upper-level features. *Mon. Wea. Rev.*, **120**, 1301–1320.

Joint Typhoon Warning Center (JTWC), 1991: *Annual tropical cyclone report.* US Naval Oceanography Command Center, COMNAVMARIANAS Box 17, FPO, San Francisco, 96630, 238 pp.

Juckes, M. N. and M. E. McIntyre, 1987: A high-resolution one-layer model of breaking planetary waves in the stratosphere. *Nature*, **328**, 590–596.

Keen, R. A., 1982: The role of cross-equatorial tropical cyclone pairs in the Southern Oscillation. *Mon. Wea. Rev.*, **110**, 1405–1416.

Kodama, Y., 1992: Large-scale common features of subtropical precipitation zones (the Baiu frontal zone, the SPCZ and the SACZ). Part I: Characteristics of subtropical frontal zones. *J. Meteor. Soc. Japan*, **70**, 813–835.

Kuo, H. L., 1973: Dynamics of quasi-geostrophic flows and instability theory. *Adv. Appl. Mech.*, **13**, 247–330.

———, 1978: A two-layer model study of the combined barotropic and baroclinic instability in the tropics. *J. Atmos. Sci.*, **35**, 1840–1860.

Kwon, H. J., 1989: A reexamination of the genesis of African waves. *J. Atmos. Sci.*, **46**, 3621–3631.

Lander, M. A., 1990: Evolution of the cloud pattern during the formation of tropical cyclone twins symmetrical with respect to the equator. *Mon. Wea. Rev.*, **118**, 1194–1202.

———, 1993: The Northward-displaced, self-sustaining, Solitary (NSS) monsoon gyre. *Submitted to Weather and Forecasting.*

———, 1994: An exploratory analysis of the relationship between tropical storm formation in the Western North Pacific and ENSO. *Mon. Wea. Rev.*, **122**, 636–651.

Lau, K.-M., L. Peng, C. H. Sui, and T. Nakazawa, 1989: Dynamics of super cloud clusters, westerly wind bursts, 30-60 day oscillations and ENSO: an unified view. *J. Meteor. Soc. Japan*, **67**, 205–219.

Li, X., and B. Wang, 1994: Barotropic dynamics of the beta gyres and beta drift. *J. Atmos. Sci.*, **51**, 746–756.

Liebmann, B., H. H. Hendon, and J. D. Glick, 1993: The relationship between tropical cyclones of the Western Pacific and Indian Oceans and the Madden-Julian Oscillation. Unpublished manuscript.

Lindzen, R. S., 1988: Instability of plane parallel shear flow (toward a mechanistic picture of how it works). *PAGEOPH*, **126**, 103–121.

——— and K. K. Tung, 1978: Wave overreflection and shear instability. *J. Atmos. Sci.*, **35**, 1626–1632.

Love, G., 1985: Cross-equatorial influence of winter hemisphere subtropical cold surges. *Mon. Wea. Rev.*, **113**, 1487–1498.

Luther, D. S., D. E. Harrison, and R. A. Knox, 1983: Zonal winds in the Central Equatorial Pacific and El Niño. *Science*, **222**, 327–330.

Madden, R. A., and P. R. Julian, 1994: Observations of the 40-50 day tropical oscillation – a review. *Mon. Wea. Rev.*, **122**, 814–837.

Mapes, B., and R. A. Houze, 1992: An integrated view of the 1987 Australian monsoon and its mesoscale convective systems. I: Horizontal structure. *Quart. J. Roy. Meteor. Soc.*, **118**, 927–963.

———, and ———, 1993: Cloud clusters and superclusters over the oceanic warm pool. *Mon. Wea. Rev.*, **121**, 1398–1415.

Mass, C., 1979: A linear primitive equation model of African wave disturbances. *J. Atmos. Sci.*, **36**, 2075–2092.

McBride, J., 1981a: Observational analysis of tropical cyclone formation. Part I: basic description of data sets. *J. Atmos. Sci.*, **38**, 1117–1131.

———, 1981b: Observational analysis of tropical cyclone formation. Part III: budget analysis. *J. Atmos. Sci.*, **38**, 1152–1166.

———, and R. Zehr, 1981: Observational analysis of tropical cyclone formation. Part II: Comparison of non-developing versus developing systems. *J. Atmos. Sci.*, **38**, 1132–1151.

McIntyre, M. E., and T. N. Palmer, 1983: Breaking planetary waves in the stratosphere. *Nature*, **305**, 593–600.

———, and ———, 1984: The 'surf zone' in the stratosphere. *J. Atmos. Terr. Phys.*, **46**, 825–849.

Melander, M. V., J. C. Williams, and N. J. Zabusky, 1985: Axisymmetrization and vorticity-gradient intensification of an isolated two-dimensional vortex through filamentation. *J. Fluid Mech.*, **178**, 137–159.

Merrill, R. T., 1984: A comparison of large and small tropical cyclones. *Mon. Wea. Rev.*, **112**, 1408–1418.

Miller, L., R. E. Cheney, and B. C. Douglas, 1988: GEOSAT altimeter observations of Kelvin waves and the 1986-1987 El Niño. *Science*, **239**, 52–54.

Montgomery, M. T., and B. F. Farrel, 1993: Tropical cyclone formation. *J. Atmos. Sci.*, **50**, 285–310.

Mozer, J. B., and J. A. Zehnder, 1994: Cluster analysis of eastern North Pacific tropical cyclogenesis precursors. *J. Geophys. Res.*, **99**, 8085–8093.

Nakazawa, T., 1988: Tropical super clusters within intraseasonal variations over the Western Pacific. *J. Meteor. Soc. Japan*, **66**, 823–839.

Nitta, T., and M. Yanai, 1969: A note on the barotropic instability of the tropical easterly current. *J. Meteor. Soc. Japan*, **47**, 127–130.

Norquist, D. C., E. E. Recker and R. J. Reed, 1977: The energetics of African wave disturbances as observed during phase III of GATE. *Mon. Wea. Rev.*, **105**, 334–342.

Ooyama, K. V., 1964: A dynamical model for the study of tropical cyclone development. *Geofis. Int.*, **4**, 187–198.

———, 1982: Conceptual evolution of the theory and modeling of the tropical cyclone. *J. Meteor. Soc. Japan*, **60**, 369–380.

Philander, S. G., 1990: *El Niño, La Niña, and the Southern Oscillation.* Academic Press, 293pp. [ISBN 0-12-553235-0].

Phoebus, P. A., 1993: Westerly wind anomalies associated with developing tropical cyclones in the Western Pacific. *Preprints of the 20th Conference on Hurricanes and Tropical Meteorology*, Amer. Meteor. Soc., 127–130.

Polvani, L. M., and R. A. Plumb, 1992: Rossby wave breaking, microbreaking, filamentation and secondary vortex formation: the dynamics of a perturbed vortex. *J. Atmos. Sci.*, **49**, 462–476.

Rayleigh, J. W. S., 1945: *The Theory of Sound*, **vol. 2**, Dover Publications, Inc., New York, 504 pp. [ISBN 0-486-60293].

Raymond, D. J., 1993: Westerly wind bursts in the Western Equatorial Pacific: an air-sea interaction instability? *Preprints of the 20th Conference on Hurricanes and Tropical Meteorology*, Amer. Meteor. Soc., 16–19.

Reed, R. J., D. C. Norquist, and E. E. Recker, 1977: The structure and properties of African wave disturbances as observed during phase III of GATE. *J. Atmos. Sci.*, **105**, 317–333.

———, and E. E. Recker, 1971: Structure and properties of synoptic-scale wave disturbances in the Equatorial Western Pacific. *J. Atmos. Sci.*, **28**, 1117–1133.

Reilly, D. H., 1992: On the role of upper-tropospheric potential vorticity advection in tropical cyclone formation: case studies from 1991. Ms. Thesis, Massachusets Institute of Technology, Cambridge, MA, 124 pp.

Renard, R. J., and W. N. Bowman, 1976: The climatology and forecasting of eastern North Pacific Ocean tropical cyclones. *NEPRF Tech, Paper No. 7-76*, 79 pp.

Rennick, M. A., 1976: The generation of African waves. *J. Atmos. Sci.*, **33**, 1955–1969.

Riehl, H., 1945: Waves in the easterlies and the polar front in the tropics. University of Chicago Department of Meteorology, Victor P. Starr, Ed., Misc. Rep. No. 17, 79 pp.

———, 1948: On the formation of west Atlantic hurricanes. Studies of upper-air conditions in low latitudes. University of Chicago Department of Meteorology, Victor P. Starr, Ed., Misc. Rep. No. 24, 67 pp.

Ripa, P., 1983: General stability conditions for zonal flows in a one-layer model on the β-plane or the sphere. *J. Fluid Mech.*, **126**, 463–489.

Rotunno, R., and K. A. Emanuel, 1987: An air-sea interaction theory for tropical cyclones. Part II: Evolutionary study using a nonhydrostatic axisymmetric numerical model. *J. Atmos. Sci.*, **44**, 542–561.

Sadler, J. C., 1976: A role of the tropical upper tropospheric trough in early season typhoon development. *Mon. Wea. Rev.*, **104**, 1266–1278.

———, 1978: Mid-season typhoon development and intensity changes and the Tropical Upper Tropospheric Trough. *Mon. Wea. Rev.*, **106**, 1137–1152.

Saha, K., F. Sanders, and J. Schukla, 1981: Westward propagating predecessors of monsoon depressions. *Mon. Wea. Rev.*, **109**, 330–343.

Schubert, W. H., P. E. Ciesielski, and K. W. Harding, 1992: Dynamics of the Australian summer monsoon. Colorado State University, Dept. of Atmospheric Science, Paper No. 492, 48 pp.

———, ———, D. E. Stevens, and H. Kuo, 1991: Potential vorticity modeling of the ITCZ and the Hadley circulation. *J. Atmos. Sci.*, **48**, 1493–1509.

———, and J. J. Hack, 1982: Inertial stability and tropical cyclone development. *J. Atmos. Sci.*, **39**, 1687–1697.

———, J. J. Hack, P. L. Silva Dias and S. R. Fulton, 1980: Geostrophic adjustment in an axissymmetric vortex. *J. Atmos. Sci.*, **37**, 1464–1484.

Shepherd, T. G., 1990: Arnol'd stability applied to fluid flow: successes and failures. *Proceedings of IMA Workshop on Nonlinear phenomena in Atmospheric and Oceanic Sciences*. Springer-Verlag.

Silva Dias, P. L., W. H. Schubert, and M. DeMaria, 1983: Large-scale response of the tropical atmosphere to transient convection. *J. Atmos. Sci.*, **40**, 2689–2707.

Simmons, A. J., 1977: A Note on the instability of the African easterly jet. *J. Atmos. Sci.*, **34**, 1670–1674.

Simpson, R. H., N. Frank, D. Shideler, and H. M. Johnson, 1969: Atlantic tropical disturbances of 1968. *Mon. Wea. Rev.*, **97**, 240–255.

Sui, C. H., and K. M. Lau, 1992: Multiscale phenomena in the tropical atmosphere over the Western Pacific. *J. Atmos. Sci.*, **120**, 407–430.

Tai, K. S., and Y. Ogura, 1987: An observational study of easterly waves over the Eastern Pacific in the northern summer using FGGE data. *J. Atmos. Sci.*, **44**, 339–361.

Torrence, C., 1993: Westerly wind bursts as precursors to El Niño. *Preprints of the 20th Conference on Hurricanes and Tropical Meteorology*, Amer. Meteor. Soc., 5–8.

Velasco, I., and J. M. Fritsch, 1987: Mesoscale convective complexes in the Americas. *J. Geophys. Res.*, **92**, 9591–9613.

Verlinde, J., and W. R. Cotton, 1990: A mesoscale vortex couplet observed in the trailing anvil of a multicelular convective complex. *Mon. Wea. Rev.*, **118**, 993–1010.

Waliser, D. E., and C. Gautier, 1993: A satellite-derived climatology of the ITCZ. *J. Climate*, **6**, 2162–2174.

Wang, B., and H. Rui, 1990: Synoptic climatology of transient tropical intraseasonal convective anomalies. *Meteor. Atmos. Phys.*, **44**, 43–61.

Weickmann, K. M., and S. J. S. Khalsa, 1990: The shift of convection from the Indian Ocean to the Western Pacific Ocean during a 30-60 day oscillation. *Mon. Wea. Rev.*, **118**, 964–978.

Weisman, M. L., W. C. Skamarock, J. B. Klemp, and C. Davis, 1993: The generation of mesoscale convective vortices within long-lived convective systems. *Preprints of the 20th Conference on Hurricanes and Tropical Meteorology*, Amer. Meteor. Soc., 120–123.

Yanai, M., 1961: A detailed analysis of typhoon formation. *J. Meteor. Soc. Japan*, **39**, 187–213.

———, S. Esbensen and J. Chu, 1973: Determination of bulk properties of tropical cloud clusters from large-scale heat and moisture budgets. *J. Atmos. Sci.*, **30**, 611–627.

Zehnder, J. A., 1991: The interaction of planetary-scale tropical easterly waves with topography: a mechanism for the initiation of tropical cyclones. *J. Atmos. Sci.*, **48**, 1217–1230.

———, and R. T. Gall, 1991a: Alternative mechanisms of tropical cyclone formation in the Eastern North Pacific. *Atmósfera*, **4**, 37–51.

———, and ———, 1991b: On a mechanism for orographic triggering of tropical cyclones in the Eastern North Pacific. *Tellus*, **43A**, 25–36.

Zehr, R. M., 1992: Tropical cyclogenesis in the Western North Pacific. NOAA Technical Report NESDIS 61, 181 pp.

———, 1993: Recognition of mesoscale vortex initiation as stage one of tropical cyclogenesis. *Preprints of the 20th Conference on Hurricanes and Tropical Meteorology*, Amer. Meteor. Soc., 405–408.

Zhong, W., R. L. Gall, and J. A. Zehnder, 1993: Interannual variability of tropospheric waves in the tropics: a possible link with tropical cyclogenesis. *J. Atmos. Sci.*, **50**, 333–341.

Appendix A

NUMERICAL ASPECTS OF THE GLOBAL SHALLOW WATER MODEL

The global shallow water model from Section 2.1 is solved using the spectral transform method in space and semi-implicit differencing in time. A brief review of these methods is presented below. A detailed discussion of the numerical aspects of this model is presented in Hack and Jakob (1992).

A.1 The spectral transform method

The spectral transform method consists of locally calculating all non-linear terms and diabatic processes on an associated transform grid in physical space and evaluating linear terms, derivatives and time tendencies in spectral space.

On the surface of a sphere, the spectral space is spanned by the eigenfunctions of Laplace's tidal equation. These form a complete and orthogonal set of functions called spherical harmonics. The completeness property of the spherical harmonics, implies that any function $g(\lambda, \mu)$ (with sufficient continuity properties) on the surface of a sphere can be represented to a certain degree of precision by a linear combination of the spherical harmonics, that is

$$g(\lambda, \mu) = \sum_{m=-\infty}^{\infty} \sum_{n=-\infty}^{\infty} g_n^m P_n^m(\mu) e^{im\lambda} \tag{A.1}$$

where $P_n^m(\mu)$ are the associated Legendre Polynomials.

Using the orthogonality property of the spherical harmonics the coefficients g_n^m may be calculated using

$$g_n^m = \int_{-1}^{+1} \frac{1}{2\pi} \int_0^{2\pi} g(\lambda, \mu) e^{-im\lambda} d\lambda P_n^m(\mu) d\mu \tag{A.2}$$

Equations (A.1) and (A.2) above are called a transform pair since they are used to transform variables back and forth between physical and spectral spaces.

Nevertheless, for quantitative purposes, evaluation of (A.1) requires truncation of the series. Using triangular truncation, (A.1) becomes

$$g(\lambda,\mu) = \sum_{m=-M}^{M} \sum_{n=|m|}^{M} g_n^m P_n^m(\mu) e^{im\lambda} \tag{A.3}$$

where M is both the shortest wave included in the east-west direction and the highest degree of the associated Legendre polynomials in the meridional direction. Therefore M is associated to the resolution of the model in both the zonal and meridional directions.

Numerical evaluation of (A.2) requires approximating the double integral by two summations. The inner integral in (A.2) is approximated by

$$g^m(\mu) = \frac{1}{2\pi}\int_0^{2\pi} g(\lambda,\mu)e^{-im\lambda}d\lambda = \frac{1}{I}\sum_{\mathtt{i}=1}^{I} g(\lambda_{\mathtt{i}},\mu)e^{-im\lambda_{\mathtt{i}}} \tag{A.4}$$

where each individual longitude is given by $\lambda_{\mathtt{i}} = 2\pi\mathtt{i}/\mathtt{I}$ and I is the total number of gridpoints in the east-west direction of the transform grid. In order to allow an exact, unaliased Fourier transform of quadratic terms, $I \geq 3M+1$ is used. This Fourier transform is evaluated using a Fast Fourier Transform algorithm. The outer integral is approximated via Gaussian quadrature,

$$g_n^m = \int_{-1}^{+1} g^m(\mu)P_n^m(\mu)d\mu = \sum_{\mathtt{j}=1}^{J} g^m(\mu_{\mathtt{j}})P_n^m(\mu_{\mathtt{j}})w_{\mathtt{j}} \tag{A.5}$$

where the Gaussian latitudes ($\mu_{\mathtt{j}}$) are the roots of the Legendre Polynomial $P_J(\mu)$, J is the total number of Gaussian latitudes in the north-south direction and the Gaussian weight is $w_{\mathtt{j}} = 2(1-\mu_{\mathtt{j}}^2)/[JP_{J-1}(\mu_{\mathtt{j}})]^2$. Once again, in order to permit exact, unaliased computations of quadratic terms, $J \geq (3M+1)/2$ is used for triangular truncation. Finally, plugging (A.5) into (A.4) produces the discrete form of (A.2), which is used to obtain the spectral space version of the governing equations given in chapter 2.

The spectral space representations of (2.5), (2.6) and (2.8) may then be written as:

$$\begin{aligned}\frac{\partial\delta_n^m}{\partial t} &= -\sum_{\mathtt{j}=1}^{J}[imB^m(\mu_{\mathtt{j}})P_n^m(\mu_{\mathtt{j}}) - A^m(\mu_{\mathtt{j}})H_n^m(\mu_{\mathtt{j}})]\frac{w_{\mathtt{j}}}{a(1-\mu_{\mathtt{j}}^2)} + \\ &\quad + \frac{n(n+1)}{a^2}\sum_{\mathtt{j}=1}^{J}[E^m(\mu_{\mathtt{j}}) + \Phi^m(\mu_{\mathtt{j}})]P_n^m(\mu_{\mathtt{j}})w_{\mathtt{j}}\end{aligned} \tag{A.6}$$

$$\frac{\partial \eta_n^m}{\partial t} = -\sum_{j=1}^{J}[imA^m(\mu_j)P_n^m(\mu_j) - B^m(\mu_j)H_n^m(\mu_j)]\frac{w_j}{a(1-\mu_j^2)} \tag{A.7}$$

$$\frac{\partial \Phi_n^m}{\partial t} = -\sum_{j=1}^{J}[imC^m(\mu_j)P_n^m(\mu_j) - D^m(\mu_j)H_n^m(\mu_j)]\frac{w_j}{a(1-\mu_j^2)} - \overline{\Phi}\delta_n^m + Q_n^m \tag{A.8}$$

where $A = U\eta$, $B = V\eta$, $C = U\Phi$, $D = V\Phi$, $E = U^2 + V^2/2(1-\mu^2)$ and A_n^m, B_n^m, C_n^m, D_n^m and E_n^m are their spectral space representations. Also,

$$H_n^m = (1-\mu^2)\frac{dP_n^m}{d\mu} \tag{A.9a}$$

and:

$$\nabla^2 P_n^m(\mu)e^{im\lambda} = -\frac{n(n+1)}{a^2}P_n^m(\mu)e^{im\lambda} \tag{A.9b}$$

In order to close the system composed of equations (A.6)-(A.8), it is necessary to obtain diagnostic equations for U and V as functions of δ and η. These diagnostic equations are obtained by using the spectral space representations of (2.10)-(2.13) and are given by

$$\eta_n^m = \sum_{j}^{J} = [imV^m(\mu_j)P_n^m(\mu_j) + U^m(\mu_j)H_n^m(\mu_j)]\frac{w_j}{c(1-\mu_j^2)} + f_n^m \tag{A.10}$$

$$\delta_n^m = \sum_{j}^{J} = [imU^m(\mu_j)P_n^m(\mu_j) + V^m(\mu_j)H_n^m(\mu_j)]\frac{w_j}{a(1-\mu_j^2)} \tag{A.11}$$

Equations (A.6)-(A.8) and (A.10)-(A.11) form the closed system that is integrated by the model using the semi-implicit time scheme that will be briefly described in the next section.

Finally, in spectral space, the nonlinear balance equation (2.22) used in the initialization of some model runs becomes

$$\begin{aligned}\Phi_n^m &= -\frac{a^2}{n(n+1)}\sum_{j=1}^{J}[imB^m(\mu_j)P_n^m(\mu_j) - A^m(\mu_j)H_n^m(\mu_j)]\frac{w_j}{a(1-\mu_j^2)} \\ &\quad -E_n^m\end{aligned} \tag{A.12}$$

This concludes the review of the spatial representations used in the model, the time integration scheme is presented next.

A.2 The semi-implicit time differencing scheme

The shallow water equations represent Rossby, Kelvin, mixed Rossby-gravity and gravity modes. The presence of the very fast gravity modes implies that when using an explicit time differencing procedure, the time step must be very small due to stability constraints. In this model, this problem is avoided with the use of a semi-implicit time differencing scheme. In a semi-implicit scheme, terms that govern the propagation of the gravity modes (the divergence term in the continuity equation and the Laplacian of the geopotential in the divergence prognostic equation) are treated implicitly and all other terms are treated explicitly (see Haltiner and Williams, 1980, for details). Both explicit and implicit differentiations use a second order accurate centered time scheme.

After semi-implicit time discretization, equations (A.6) through (A.8) become:

$$\begin{aligned}(\eta_n^m)^{\tau+1} &= \sum_{\mathrm{j}=1}^{J}\Big\{\Big\{[\eta^m(\mu_\mathrm{j})]^{\tau-1} - 2\triangle t\varepsilon_f\left[\eta^m(\mu_\mathrm{j})\right]^{\tau}\Big\}P_n^m(\mu_\mathrm{j}) \\ &\quad -\frac{2\triangle t}{a(1-\mu_\mathrm{j}^2)}[imA^m(\mu_\mathrm{j})P_n^m(\mu_\mathrm{j}) - B^m(\mu_\mathrm{j})H_n^m(\mu_\mathrm{j})]\Big\}w_\mathrm{j} \\ &\quad +2\triangle t\varepsilon_f f_1^0 \qquad\qquad (A.13)\end{aligned}$$

$$\begin{aligned}(\delta_n^m)^{\tau+1} &= \sum_{\mathrm{j}=1}^{J}\{[\delta^m(\mu_\mathrm{j})]^{\tau-1} - 2\triangle t\varepsilon_f\left[\delta^m(\mu_\mathrm{j})\right]^{\tau}\}P_n^m(\mu_\mathrm{j})w_\mathrm{j} \\ &\quad +\left[1+\overline{\Phi}\triangle t^2\frac{n(n+1)}{a^2}\right]^{-1}\sum_{\mathrm{j}=1}^{J}\Big\{2\triangle t\frac{n(n+1)}{a^2}\left[[\Phi^m(\mu_\mathrm{j})]^{\tau-1} + E^m(\mu_\mathrm{j})\right]P_n^m(\mu_\mathrm{j}) \\ &\quad +\frac{2\triangle t}{a(1-\mu_\mathrm{j}^2)}\left[imB^m(\mu_\mathrm{j})P_n^m(\mu_\mathrm{j}) + A^m(\mu_\mathrm{j})H_n^m(\mu_\mathrm{j})\right] \\ &\quad +\frac{(2\triangle t)^2}{2a(1-\mu_\mathrm{j}^2)}\frac{n(n+1)}{a^2}\left[-imC^m(\mu_\mathrm{j})P_n^m(\mu_\mathrm{j}) + D^m(\mu_\mathrm{j})H_n^m(\mu_\mathrm{j})\right]\Big\}w_\mathrm{j} \qquad (A.14)\end{aligned}$$

$$\begin{aligned}(\Phi_n^m)^{\tau+1} &= \sum_{\mathrm{j}=1}^{J}\{[\Phi^m(\mu_\mathrm{j})]^{\tau-1} - 2\triangle t\varepsilon_f[\Phi^m(\mu_\mathrm{j})]^{\tau}\}P_n^m(\mu_\mathrm{j})w_\mathrm{j} \\ &\quad +\left[1+\overline{\Phi}\triangle t^2\frac{n(n+1)}{a^2}\right]^{-1}\sum_{\mathrm{j}=1}^{J}\Big\{-\frac{\overline{\Phi}}{2}\frac{n(n+1)}{a^2}(2\triangle t)^2E^m(\mu_\mathrm{j})P_n^m(\mu_\mathrm{j}) \\ &\quad -2\triangle t\overline{\Phi}[\delta^m(\mu_\mathrm{j})]^{\tau-1}P_n^m(\mu_\mathrm{j}) \\ &\quad +\frac{2\triangle t}{a(1-\mu_\mathrm{j}^2)}\left[-imC^m(\mu_\mathrm{j})P_n^m(\mu_\mathrm{j}) + D^m(\mu_\mathrm{j})H_n^m(\mu_\mathrm{j})\right] \\ &\quad -\frac{\overline{\Phi}}{2}\frac{(2\triangle t)^2}{a(1-\mu_\mathrm{j}^2)}\left[imB^m(\mu_\mathrm{j})P_n^m(\mu_\mathrm{j}) + A^m(\mu_\mathrm{j})H_n^m(\mu_\mathrm{j})\right]\Big\}w_\mathrm{j} \qquad (A.15)\end{aligned}$$

where τ indicates the time step.

Equations (A.16)-(A.18) and (A.10)-(A.11) are the closed systems used by the model to prognose the mass and wind fields.

Appendix B

LINEAR STABILITY ANALYSIS

In this appendix, the method used in chapter 2 to calculate the linear normal mode stability of zonal vorticity strips on the sphere is delineated

Consider the basic state zonally symmetric absolute vorticity distribution shown in Fig. B.1. At the co-latitudes, $\mu = \mu_j \, (j = 1, 2, \ldots, J)$, the vorticity jumps by an amount ξ_j. The ξ_j can be either positive or negative and the distances between successive $\mu = \mu_j$ are not necessarily constant. The basic state absolute angular velocity, $\bar{\omega} + \Omega$ (where $\bar{\omega} = \bar{u} a \cos\phi$), corresponding to this vorticity distribution is

$$\bar{\omega}(\mu) + \Omega = \sum_{j'=1}^{j} \tfrac{1}{2}\xi_{j'} \left(\frac{1+\mu_{j'}}{1+\mu} \right) + \sum_{j'=j+1}^{J} \tfrac{1}{2}\xi_{j'} \left(\frac{1-\mu_{j'}}{1-\mu} \right) \quad \text{for} \quad \mu_j \le \mu \le \mu_{j+1}. \tag{B.1}$$

Multiplication of (B.1) by $(1-\mu^2)$, followed by differentiation with respect to μ, yields the basic state absolute vorticity profile

$$\begin{aligned} \bar{\zeta}(\mu) &= 2\Omega \sin\phi - \frac{\partial(\bar{u}\cos\phi)}{a\cos\phi\partial\phi} = -\frac{d[(\bar{\omega}+\Omega)(1-\mu^2)]}{d\mu} \\ &= \sum_{j'=1}^{j} \tfrac{1}{2}\xi_{j'}(1+\mu_{j'}) - \sum_{j'=j+1}^{J} \tfrac{1}{2}\xi_{j'}(1-\mu_{j'}) \qquad \text{for} \qquad \mu_j \le \mu \le \mu_{j+1}. \end{aligned} \tag{B.2}$$

Equation (B.2) corresponds to the stairstep vorticity pattern shown in Fig.(B.1).

If equation (B.1) is evaluated at $\mu = \mu_j$, the resulting expression can be written

$$\sum_{j'=1}^{J} A_{jj'}\xi_{j'} = \bar{\omega}_j + \Omega, \tag{B.3}$$

where $\bar{\omega}_j = \bar{\omega}(\mu_j)$ and

$$A_{jj'} = \tfrac{1}{2} \begin{cases} \frac{1+\mu_{j'}}{1+\mu_j} & j' \le j \\ \frac{1-\mu_{j'}}{1-\mu_j} & j' > j. \end{cases} \tag{B.4}$$

The procedure used to find ξ_j $(j = 1, 2, \ldots, J)$ from a continuous $\bar{u}(\mu)$ profile is now delineated. First note that the continuous $\bar{u}(\mu)$ profile also defines a continuous $\bar{\omega}(\mu)$

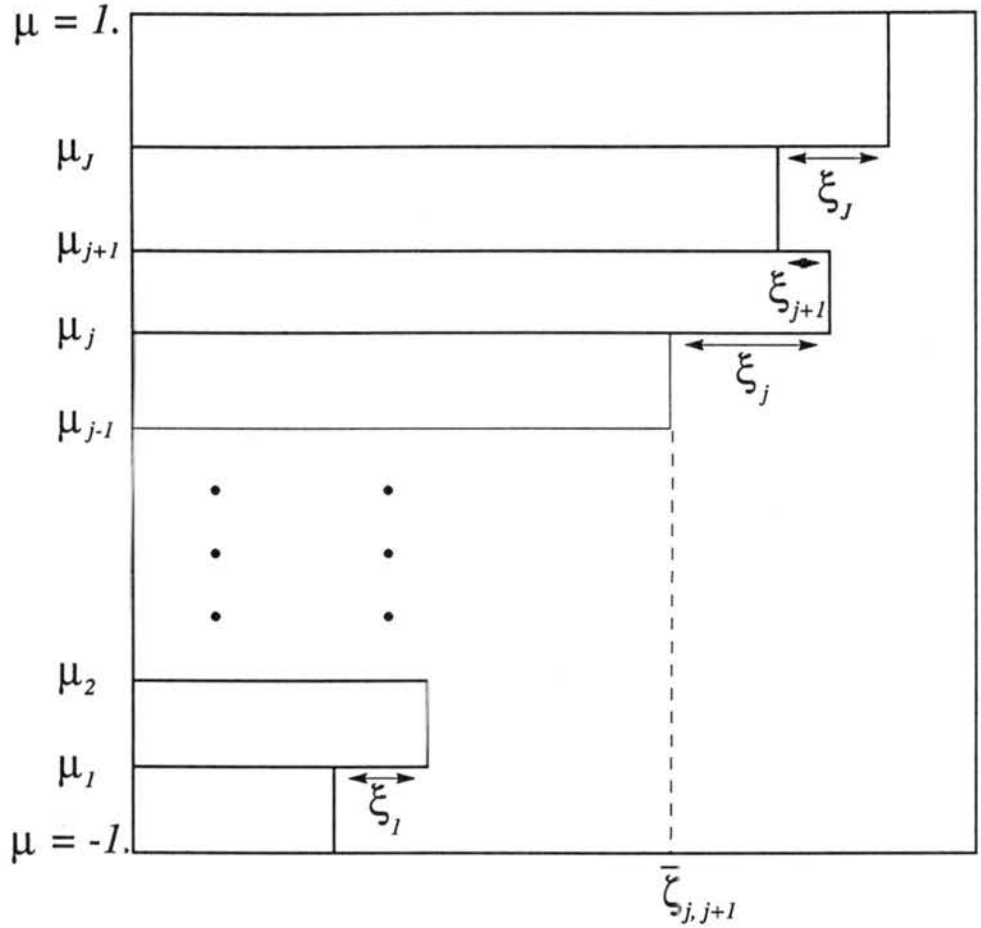

Figure B.1: Stairstep distribution of vorticity.

profile since $\bar{u} = \bar{\omega}a(1-\mu^2)^{1/2}$. Then define μ_j $(j = 1, 2, \ldots, J)$, which determines $A_{jj'}$ and $\bar{\omega}_j$. And finally solve the linear algebraic system (B.3) for ξ_j $(j = 1, 2, \ldots, J)$. The discretized (or interpolated) versions of $\bar{\omega}$ and $\bar{\zeta}$ can now be plotted from equations (B.1) and (B.2).

Now suppose that each interface is slightly displaced sinusoidally. The value of μ for the j^{th} interface is $\mu_j + \eta_j(\lambda, t)$, where $\eta_j(\lambda, t) = \hat{\eta}_j e^{i(m\lambda - \nu t)}$. For this situation the perturbation vorticity will be zero except near the interfaces, *i.e.*, $\zeta' = \nabla^2\psi' = 0$ for $\mu \neq \mu_j$ $(j = 1, 2, \ldots, J)$. Substituting $\psi(\lambda, \mu, t) = \Psi(\mu)e^{i(m\lambda - \nu t)}$ into this last equation we obtain:

$$(1-\mu^2)\frac{d}{d\mu}\left[(1-\mu^2)\frac{d\Psi}{d\mu}\right] - m^2\Psi = 0 \quad \text{for} \quad \mu \neq \mu_j \quad (j = 1, 2, \ldots, J). \tag{B.5}$$

As discussed by Dritschel and Polvani (1992), the solutions of (B.5) are $\left(\frac{1-\mu}{1+\mu}\right)^{m/2}$ and $\left(\frac{1+\mu}{1-\mu}\right)^{m/2}$, the first of which is singular at the south pole but decays to zero at the north pole, and the second of which is singular at the north pole but decays to zero at the south pole. Thus, a wavenumber m perturbation in the vorticity field at $\mu = \mu_{j'}$ has an associated streamfunction with the normalized structure $\left[\frac{(1-\mu)(1+\mu_{j'})}{(1+\mu)(1-\mu_{j'})}\right]^{m/2}$ north of $\mu = \mu_{j'}$ and the structure $\left[\frac{(1+\mu)(1-\mu_{j'})}{(1-\mu)(1+\mu_{j'})}\right]^{m/2}$ south of $\mu = \mu_{j'}$. By the superposition principle, the streamfunction associated with wavenumber m vorticity perturbations at all interfaces is:

$$\psi'(\lambda,\mu,t) = \left\{ \sum_{j'=1}^{j} B_{j'} \left[\frac{(1-\mu)(1+\mu_{j'})}{(1+\mu)(1-\mu_{j'})}\right]^{m/2} + \sum_{j'=j+1}^{J} B_{j'} \left[\frac{(1+\mu)(1-\mu_{j'})}{(1-\mu)(1+\mu_{j'})}\right]^{m/2} \right\} e^{i(m\lambda-\nu t)}, \tag{B.6}$$

for $\mu_j \le \mu \le \mu_{j+1}$. Note that this perturbation streamfunction is continuous at the interfaces. Here the $B_{j'}$ are constants which will be determined below in (B.6). It can easily be confirmed by inspection that ψ' is continuous. Note that the meridional component of velocity, $v' = \partial\psi'/a\cos\phi\partial\lambda$, is also continuous.

Now it is necessary to impose continuity of $\omega = \bar{\omega} + \omega' = \bar{\omega} - \partial\psi'/a^2\partial\mu$. Continuity of ω at $\mu_j + \eta_j$ requires that

$$\begin{aligned} &\tfrac{1}{2}\xi_j a^2(1-\mu)(1+\mu_j) + mB_j \left[\tfrac{(1-\mu)(1+\mu_j)}{(1+\mu)(1-\mu_j)}\right]^{m/2} e^{i(m\lambda-\nu t)} \\ &= \tfrac{1}{2}\xi_j a^2(1+\mu)(1-\mu_j) - mB_j \left[\tfrac{(1+\mu)(1-\mu_j)}{(1-\mu)(1+\mu_j)}\right]^{m/2} e^{i(m\lambda-\nu t)} \end{aligned} \tag{B.7}$$

at $\mu = \mu_j + \eta_j$. Linearization of (B.7) yields:

$$mB_j = +\tfrac{1}{2}\xi_j a^2 \hat{\eta}_j. \tag{B.8}$$

Imposing that the normal velocity of a particle on an interface be equal to that of the interface itself, *i.e.*,

$$\frac{\partial\eta_j}{\partial t} + \bar{\omega}_j \frac{\partial\eta_j}{\partial\lambda} = \frac{v'_j\cos\phi}{a} = \frac{im}{a^2}\psi'(\mu_j). \tag{B.9}$$

Finally, the desired standard eigenvalue problem is obtained by substituting (B.8) into (B.6) and using the resulting expression in (B.9) to obtain:

$$(\nu - m\bar{\omega}_j)\hat{\eta}_j + \sum_{j'=1}^{J} \tfrac{1}{2}\xi_{j'} I^{(m)}_{jj'} \hat{\eta}_{j'} = 0, \tag{B.10}$$

where

$$I_{jj'}^{(m)} = \begin{cases} \left[\frac{(1-\mu_j)(1+\mu_{j'})}{(1+\mu_j)(1-\mu_{j'})}\right]^{m/2} & j' \leq j \\ \left[\frac{(1+\mu_j)(1-\mu_{j'})}{(1-\mu_j)(1+\mu_{j'})}\right]^{m/2} & j' \geq j. \end{cases} \tag{B.11}$$

Once the μ_j and ξ_j $(j = 1, 2, \ldots, J)$ are specified, the $\bar{\omega}_j$ and $I_{jj'}^{(m)}$ are determined from (B.3), (B.4), (B.10) and (B.11). Then, (B.10) is (for a given m) a standard matrix eigenvalue problem with eigenvalue ν and eigenvector $\hat{\eta}_j$. This form of the eigenvalue/eigenvector problem has also been discussed by Dritschel (1989).